Università degli Studi di Firenze
Scuola di Ingegneria
DIEF - Department of Industrial Engineering of Florence

PhD School: *Energetica e Tecnologie Industriali ed Ambientali Innovative*
Scientific Area: ING-IND/09 - *Sistemi per l'Energia e l'Ambiente*

Experimental Characterization of the Rim Sealing Effectiveness in a Stator-Rotor Cavity

PhD Candidate: Ing. Lorenzo Orsini

Tutor: Prof. Ing. Bruno Facchini

Co-Tutor: Ing. Alessio Picchi

Co-Tutor: Ing. Alessio Bonini

PhD School Coordinator: Prof. Ing. Giovanni Ferrara

XXXVI PhD School Cycle - 2020-2023

Via di Santa Marta, 3, 50139 Firenze, Italy.

To my family

To Stella

May the Force be with you.
Star Wars, 1977

Acknowledgements

In the end, even this journey has come to an end. When I decided to embark on this adventure, I had no idea about the countless challenges that I would have to face in the following years. However, looking back now, I cannot help but feel a bit nostalgic for what turned out to be one of the most intense and gratifying experiences of my life. The people who know me are aware that I am not used to express my emotions but, on this occasion, I want to deeply thank all those who have been by my side during these years. Their words of comfort, encouragement and sometimes even well deserved reproach provided the strength I needed to endure and overcome the toughest moments.

The first thanks goes to Prof. Bruno Facchini, who believed in me since the very beginning, often more than I believed in myself. He has always been willing to listen and offer advice, both professionally and personally. Thank you for giving me the opportunity to take part in this unique experience that I will deeply cherish in my memories.

The next heartfelt thanks goes to Alessio, the person who welcomed me into the THT Lab from day one and put me to work, encouraging me to do what I never thought I would be capable of. I am proud to have you as my technical supervisor because your assistance has been fundamental throughout these years. In addition, special thanks go to Tommaso F., who offered me help and guidance during the initial months when I felt completely lost and did not even know where to start. Your technical and human support has been crucial, making me feel immediately welcomed within the group. Then, I want to thank all the guys in the THT Lab,

Riccardo, Tommaso B., Sofia B., Umberto, Sofia G. and Riess, with whom I shared weeks, months and years during which we faced countless challenges and difficulties but, in the end, we always ended up sharing a laugh and a beer together.

I also want to thank Antonio and all the other people who are part of the HTC group and who are in Santa Marta. You have always been available to lend me a hand when I needed it, and for this, I am grateful to all of you. I know that the opportunities to see each other are always fewer than we would like, but it is nice to feel like we are all part of a single group facing the same challenges every day.

I extend my genuine appreciation to Alessio and Luca, the two people within Baker Hughes who have followed my entire journey, always willing to offer advice or suggestions to strive for improvement. Our collaborative efforts have led to significant achievements and I am deeply thankful to both of you for this.

A heartfelt thank you is reserved to my lifelong friends, some of whom have accompanied me in my reckless choices since elementary school. We have grown up together and faced countless adventures, from the small challenges of teenage life to the adult problems we never thought would come. You have always supported me in my decisions and for that, I want to thank you deeply because I could not have wished for better friends.

Thank you Antonio and Maria for always making me feel at home and for consistently caring about me. You have always done so much for me without expecting anything in return, and for that, I extend my heartfelt gratitude to both of you.

This part is inevitably dedicated to my family, whose unwavering support has been essential to achieve all of this. I am grateful to my father and my mother for instilling in me the value of perseverance and the belief that even the most intimidating challenges can be overcome by taking one step at a time. I am grateful that you are always there to listen to me and ask about my day, even when you are tired from dealing with a thousand problems. I am also grateful to my sister, Eleonora, for being the person who has always believed in me more than anyone else

and for always sharing her thoughts with sheer honesty, often showing me that things can be looked at from a different perspective. Even though I am the older brother, I have learned more things from you than you can imagine. Thanks also to my aunts and uncle who always listen to me with open mouths as if I am saying the most fascinating thing in the world. Lastly, I want to thank my grandparents who are no longer with us, but whose memory lives on within me. Their memory has given me the strength to carry on even when I thought I could not make it.

Lastly, an immense thank you goes to Stella for always being by my side, even when I am grumpy or anxious. You have seen qualities in me that I did not know I had, taught me that reading a good book can be enjoyable and not just something boring and encouraged me to be the best version of myself. It feels like I have known you for a lifetime because together we have faced everything: we have laughed, cried, spent sleepless nights, gone on extraordinary journeys and planned our future together. The best part of these years has been knowing that I only needed to turn my head towards you to inevitably find your smile waiting for me.

Abstract

The aim of this PhD thesis has been to design, commission and test a new Rotating Cavity Rig to experimentally investigate the problem of hot gas ingestion inside a stator-rotor cavity of a gas turbine. Such facility, designed to be operated under non-reactive conditions, is a single-stage test rig where the test section is constituted by a stator disk which features 44 integrated vanes and a rotor disk which features 66 integrated blades. Both the disks can accommodate replaceable cover plates that, despite some inevitable simplifications, have been specifically designed to replicate different engine rim seals as close as possible. The interchangeability and modularity of the covers allow replacing them with different geometries in order to evaluate the impact of multiple geometrical parameters on the sealing performance. In particular, seven different configurations of radial rim seals were experimentally investigated by performing CO_2 gas sampling measurements on the stator surface. This approach showed that increasing the axial overlap or the distance between the vanes TE and the blades LE provides a modest reduction in the sealing flow rate necessary to fully seal the cavity. On the contrary, it was found that increasing the radial gap leads to an increase in the dimensional sealing flow rate which does not appear to be linear with the increase in the radial gap.

Although gas sampling measurements represent a standard and robust approach to determine the effectiveness inside a stator-rotor cavity, the use of this technique inevitably results in single point measurements where any 2D effect is neglected. Therefore, an alternative approach based on the exploitation of Pressure Sensitive Paint is presented. Prior to this research, there were no documented cases in literature where PSP had been applied to investigate the phenomenon of hot gas ingestion. First, the PSP setup was validated through a comparison of the results obtained on the stator side with those obtained by performing standard gas sampling measurements. Subsequently, the validated PSP setup was used to obtain 2D effectiveness maps also on the rotor side. This allowed the investigation of the presence of a buffer layer formed by the purge flow pumped towards the outer radius by the rotation of the rotor disk which provides further protection to the rotor side with respect to the stator side. Finally, the results obtained on both sides of the cavity were correlated with each other by performing sealing effectiveness measurements across the cavity width through the use of a concentration probe.

Furthermore, the PSP allowed performing the analysis of the effect of different values of Density Ratio on the sealing performance of the rim seal, an aspect usually neglected in the majority of the experimental facilities present in literature. Hence, two distinct values of Density Ratio were achieved by using either pure N_2 ($DR = 1$) or CO_2 ($DR = 1.52$) as purge flow. The resulting 2D effectiveness maps obtained on both sides of the cavity showed a similar qualitative behaviour for the two gases when the same dimensional quantity of purge flow was injected into the wheel-space. However, it was observed that the use of CO_2 (higher purge flow density) consistently led to reduced levels of protection. Finally, the experimental data points gathered from both the stator and the rotor sides of the cavity were respectively fitted by using either a modified version of the Orifice Model that explicitly includes the effect of the Density Ratio or the Buffer Ratio model. In the end, this allowed the evaluation of the influence of the Density Ratio on the sealing performance of the rim seal and on the low-order models employed to perform the data analysis.

Contents

Nomenclature

Acronyms

BR	Buffer Ratio model
BW	Backward (bending mode)
CFD	Computational Fluid Dynamics
CI	Combined-Ingress
DR	Density Ratio
EI	Externally-Induced
FEM	Finite Element Method
FW	Forward (bending mode)
HPT	High Pressure Turbine
LDA	Laser Doppler Anemometry
LE	Leading Edge
OM	Orifice Model
OPR	Overall Pressure Ratio
PIV	Particle Image Velocimetry
PSP	Pressure Sensitive Paint
RANS	Reynolds Averaged Navier-Stokes
RI	Rotationally-Induced
SAS	Secondary Air Systems
URANS	Unsteady Reynolds Averaged Navier-Stokes
TE	Trailing Edge

$THTLab$	Laboratory of Technology for High Temperature	
TIT	Turbine Inlet Temperature	
TLC	Thermochromic Liquid Crystal	

Greeks

α	Vane exit angle	$[deg]$
β	Blade inlet angle, Swirl ratio	$[deg]$,$[-]$
Γ_c	Ratio of discharge coefficients	$[-]$
δ	Displacement	$[m]$
δA	Elemental area of the Orifice Model	$[m^2]$
ΔC_p	Non-dimensional pressure difference	$[-]$
Δp	External pressure difference	$[Pa]$
$\Delta\varepsilon$	Buffer effect	$[-]$
ε_{ad}	Adiabatic effectiveness	$[-]$
ε_c	Concentration effectiveness	$[-]$
ε_{PSP}	PSP effectiveness	$[-]$
θ	Non-dimensional vane pitch	$[-]$
λ_{turb}	Turbulent flow parameter	$[-]$
μ	Dynamic viscosity	$[Pa \cdot s]$
ρ	Density	$[kg/m^3]$
Φ	Non-dimensional sealing parameter	$[-]$
Φ_{min}	Minimum value of Φ_0 to prevent ingress	$[-]$
Ω	Angular velocity of rotation	$[rad/s]$

Letters

A	Empirical fitting constant of BR model	$[-]$
BR	Buffer Ratio	$[-]$
c	Concentration of gas	$[-]$
C	Velocity relative to vanes	$[m/s]$
C_d	Discharge coefficient	$[-]$
C_f	Flow coefficient	$[-]$
C_p	Pressure coefficient	$[-]$

$C_{p,max}$	Non-dimensional maximum pressure difference	$[-]$
C_w	Non-dimensional flow rate	$[-]$
$C_{w,min}$	Minimum value of $C_{w,0}$ to prevent ingress	$[-]$
F	Force	$[N]$
g	Normalized wheel-space pressure	$[-]$
g^*	Value of g when $\Phi_0 = 0$	$[-]$
G	Axial gap ratio	$[-]$
G_c	Seal clearance ratio	$[-]$
h	Annulus height	$[m]$
K	Empirical constant	$[-]$
K_{xx}, K_{yy}	Stiffness in radial directions	$[N/m]$
K_{zz}	Stiffness in axial direction	$[N/m]$
$\dot{m}$	Mass flow rate	$[kg/s]$
M	Mixing parameter	$[-]$
Ma	Mach number	$[-]$
MW	Molecular weight	$[g/mol]$
n	Empirical fitting exponent of BR model	$[-]$
p	Pressure	$[Pa]$
p_{O_2}	Partial pressure of oxygen	$[Pa]$
P_{max}	Non-dimensional pressure parameter	$[-]$
r	Radius	$[m]$
r_{disk}	Characteristic radius of the seal	$[m]$
R	Generic resulting quantity	$[-]$
Re_w	Axial Reynolds number in annulus	$[-]$
Re_Φ	Rotational Reynolds number	$[-]$
$s_{c,ax}$	Axial seal clearance	$[m]$
$s_{c,rad}$	Radial seal clearance	$[m]$
$s_{overlap}$	Seal overlap	$[m]$
S	Axial width between stator and rotor	$[m]$
U	Bulk-mean velocity through the rim-seal clearance	$[m/s]$

v	Generic variable	$[-]$
vib	Amplitude of vibration	$[m]$
V	Velocity relative to blades	$[m/s]$
V_r	Radial velocity component	$[m/s]$
V_z	Axial velocity component	$[m/s]$
V_ϕ	Tangential velocity component	$[m/s]$
w	Generic measurement uncertainty	$[-]$
W	Axial velocity in the annulus	$[m/s]$

Subscripts

air	PSP case with air as purge
an	Annulus
avg	Average value
$buffer$	Buffer volume
$design$	Design condition
e	Egress flow
EI	Refer to the EI regime
fg	PSP case with foreign gas as purge
i	Ingress flow
$local$	Local conditions
max	Maximum
min	Minimum
off	PSP case with no purge flow
r	Radial direction
ref	Reference value
R	Rotor side
RI	Refer to the RI regime
s	Static Quantity
S	Stator side
tot	Total quantity
x	Refer to the x-direction
y	Refer to the y-direction
z	Refer to the z-direction

0	Location at sealant flow inlet
1	Location in the annulus at vane exit
2	Location in the wheel-space

Chapter 1

Introduction

Contents

1.1 Development of the modern gas turbine

The development of gas turbines has had a fundamental impact on the technological evolution of the 20th century, particularly on the advancement of aerial propulsion. The jet engine, a revolutionary propulsion technology that completely transformed aviation, was introduced in 1930s thanks to the work of Frank Whittle and Hans von Ohain, two prominent figures that independently contributed to the early development of this technology.

Frank Whittle, a British Royal Air Force officer, conceived the idea of a gas turbine engine able to generate thrust and thus propulsion through the expulsion of high-speed gases between the late 1920s and the early 1930s. Although initially facing challenges in securing support and funding from the British Air Ministry, he then succeeded to develop his concept into a detailed patent in 1930. The first operational jet engine, the Power Jets W.1, was then developed and tested in 1937 with the support of the Air Ministry, marking a significant milestone in aviation history (Figure 1.1). Then, the Gloster E.28/39 aircraft, powered by the Whittle W.1, made its debut flight in 1941 and became the first British jet-powered aircraft to fly.

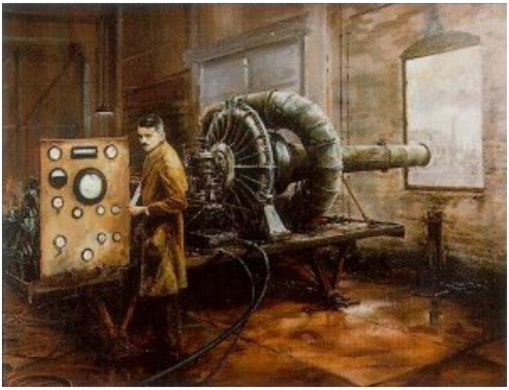

Figure 1.1: Frank Whittle with the first operational jet engine (painting by Rod Lovesey - Midland Air Museum).

Hans von Ohain, a German engineer, independently started to work on jet propulsion in the early 1930s while he was studying at the University of Göttingen. He successfully filed a patent for his jet engine design in 1936 and, unlike Whittle who had to face initial scepticism, he immediately received support from Ernst Heinkel, an aircraft designer. Thus, the aircraft Heinkel He 178, powered by the engine HeS 3B, was designed and in 1939, only a few months before Whittle's Gloster E.28/39 flight, it became the first aircraft to fly using a turbojet engine.

Since then, gas turbines have become the norm for aircraft propulsion, allowing the achievement of progressively higher flight speeds and improved efficiency. Although the fundamental operating principles have remained basically the same as those found in the initial designs by Whittle and von Ohain, gas turbines have undergone rapid advancements in the recent years and nowadays their application spans across multiple fields. In fact, owing to their remarkable power-to-weight ratio and high mechanical reliability due to the presence of a limited number of moving components, gas turbines are employed not only for aircraft propulsion, as widely discussed by Cumpsty [1], but also for helicopters and naval ships. Moreover, the availability of a wide range of power sizes, ranging from micro-turbines of a few tens of kW to heavy-duty industrial ones capable to produce hundreds of MW, allows gas turbines to be employed for power distribution and electricity generation as well. An additional yet very important advantage of gas turbines is the possibility to employ different types of fuels including fossil fuels, fuel oils, natural gas and even hydrogen. In particular, the use of hydrogen has gained considerable success in the recent years in both academic and industrial contexts, as it reduces the overall amount of NO_x, CO and CO_2 emitted from the combustion process [2]. Alternatively, Chang et al. [3] have recently demonstrated that it is possible to directly fuel a commercial micro-turbine with the biogas obtained from a sewage treatment plant, still achieving good operational flexibility and acceptable thermal efficiencies (≈23%). The main advantage is the possibility to directly use the biogas without requiring a chemical treatment. On the contrary, if one wanted to inject the biogas into a pipeline, the treatment would be necessary to reduce the content of CO_2 and water, leading to further energy inefficiencies and complications.

Finally, the remarkable versatility of gas turbines has also made them suitable to be used in combined cycles and co-generation systems. Recently, advanced combined cycles (see Figure 1.2), where solar concentration systems have been incorporated to further enhance the overall efficiency, have been described in literature [4, 5]. Speaking of renewable energies, it is also worth to remember that gas turbines are required to play a fundamental role in supporting the integration and optimization of renewable sources towards a more sustainable future. In fact, as renewable energies continue to expand, their inherently intermittent nature represents a challenge that needs to be addressed in order to ensure a stable and reliable power supply. In this context, gas turbines represents a versatile solution by acting as a flexible backup power source capable of rapidly adjusting to the fluctuations of the renewable energy production.

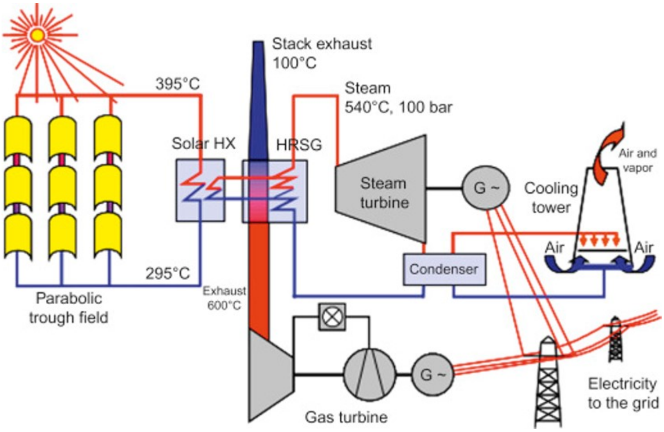

Figure 1.2: Example of an integrated solar combined cycle plant [4].

1.2 Advancements in cooling technology

Nowadays, enhancing the performance of gas turbines has become an increasingly demanding and complex task for engine designers who are required to face a continuous challenge in order to achieve ever-improving levels of efficiency. Alongside efforts to reduce weight, advancements in new materials, development of novel manufacturing techniques and aerodynamics enhancements, over the years there has been a remarkable increase in the Overall Pressure Ratio (OPR) and, consequently, in the Turbine Inlet Temperature (TIT), as shown in Figure 1.3. In particular, the latter has been progressively increased to the extent that it is now common for modern engines to reach temperatures of 2000 K and beyond [1, 6]. However, despite employing the most advanced monocrystalline nickel-based alloys to manufacture the turbine blades of the first stages, these would reach the melting point at around 1500 K. Consequently, even the most advanced materials exhibit maximum acceptable temperatures that are several hundred degrees lower than the gas temperatures encoun-

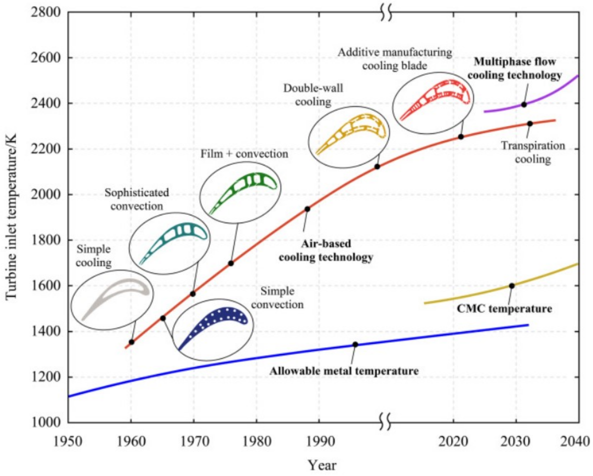

Figure 1.3: Progression in cooling technology for turbine blades [6].

tered at the turbine inlet of contemporary engines. This temperature difference must be then compensated through technological progress in terms of further advancement of heat-resistant materials, application of ceramic coatings and improved cooling strategies. Consequently, cooling air at approximately 900 K is bled off from the compressor, distributed to several locations through a complex internal network known as the Secondary Air System (SAS), used to cool the hot components and then fed back to the main gas path. Although a lot of attention has been usually reserved to cooling techniques that protect the blades and vanes (film cooling, pin fins, turbulators…), sealing the cavity between the rotating and the stationary components is equally important in order to protect the discs and blade roots from the detrimental effect of the hot gas ingested from the main annulus. The complexity of a modern SAS is shown in Figure 1.4 where the different cooling and sealing flows present in a High-Pressure Turbine (HPT) have been highlighted. Nonetheless, since these airflows are not involved in the combustion process, they do not directly contribute to the generation of power. Consequently, the extraction of air for cooling and sealing purposes leads to a reduction in engine efficiency and overall work output. Therefore, since nowadays the SAS is required to manage considerable quantities of cooling air, ranging from 15% to 25% of the main flow, being able to accurately estimate the necessary quantity of cooling required by the turbine has become a fundamental task. In fact, while the use of an insufficient amount of cooling would lead to overheating of critical components, thus causing catastrophic damages, an excessive quantity of cooling could lead to additional undesired losses due to the mixing with the main flow that in conjunction with the reduced work output could result in a suppression of the advantages of having an higher TIT. Hence, effectively controlling the sealing of stator-rotor cavities can be achieved by pressuring the cavity through the injection of sealing air that counteracts the ingestion of hot gases from the annulus and by fitting a non-contacting rim seal, such as the one depicted in Figure 1.5, at the periphery between the stator and rotor disks to further minimize the ingested flow.

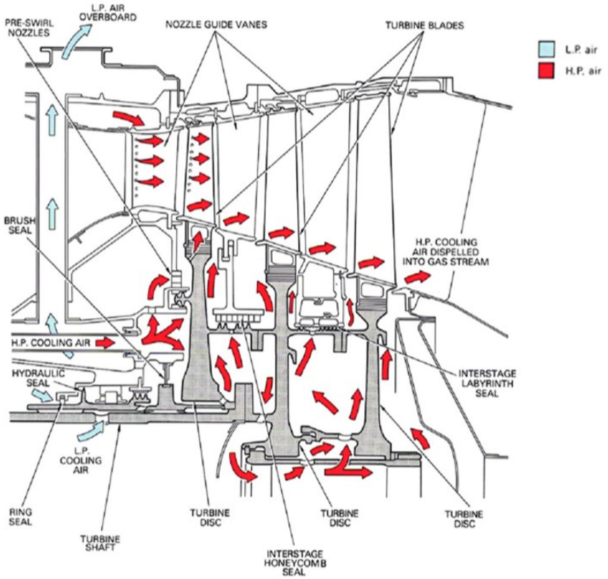

Figure 1.4: Internal air system of a gas turbine [7].

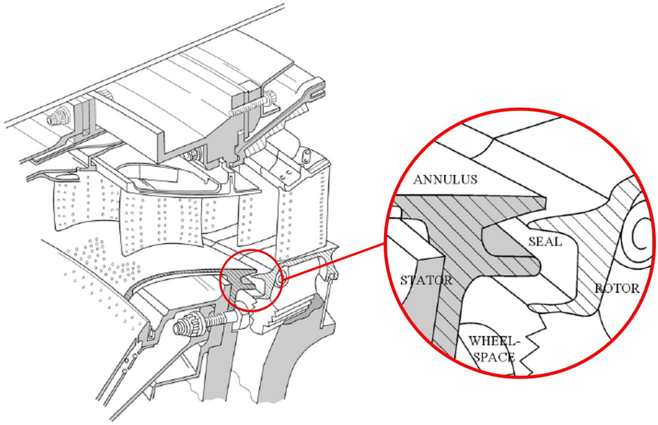

Figure 1.5: Generic rim seal configuration in a HPT stage [8].

1.3 Introduction to hot gas ingestion mechanisms

Given the need to enhance the performance of secondary air systems to optimize the efficiency of gas turbines, it becomes of paramount importance to understand the physical phenomena underlying hot gas ingestion. Although a comprehensive literature review will be provided in Chapter 2, the purpose of this section is to introduce the primary mechanisms commonly associated to the ingestion of hot gases inside stator-rotor cavities:

- Externally-Induced ingress (Section 1.3.1);
- Rotationally-Induced ingress (Section 1.3.2);
- Combined Ingress (Section 1.3.3);

1.3.1 Externally-Induced ingress

The dominant mechanism behind the ingestion of hot gases in gas turbines has been attributed to the presence of non-axisymmetric, unsteady and 3D pressure fluctuations in the main annulus flow. This circumferential variation of static pressure arises from the passage of the flow over the stationary vanes and rotating blades and it leads to the formation of different regions within the turbine annulus where the external pressure is either higher (indicated as + in Figure 1.6) or lower (indicated as – in Figure 1.6) in comparison to the pressure within the wheel-space. Consequently, this results in corresponding flows of hot gas from the annulus into the wheel-space (ingress) and of sealing air from the wheel-space to the annulus (egress) [8]. The illustration reported in Figure 1.6 uses red arrows to depict the ingress of hot gases and blue arrows to represent the exit of cooler sealing air. This type of ingestion is commonly referred to as Externally-Induced (EI) ingress [9, 10]. In general, the impact of the peak-to-through pressure difference on the degree of ingress has been found to weaken as the separation distance between the trailing edge (TE) of the vane and the leading edge (LE) of the blade increases. Among the many possible parameters that may influence the ingestion of hot gas into

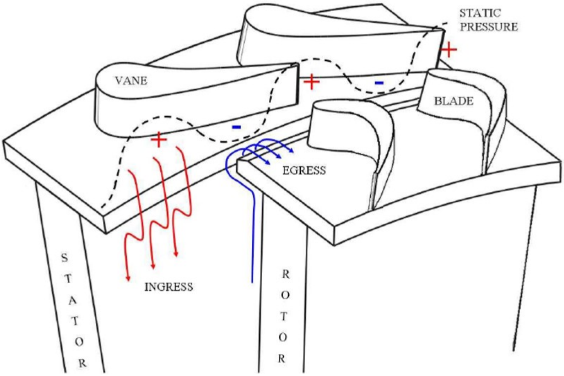

Figure 1.6: Circumferential variation of static pressure in a gas turbine annulus associated with the mechanism of EI ingress [8].

the wheel-space, Sangan [11] indicates the following factors as the most influential ones: the axial distance between vanes and blades and their geometry/shape, the Mach and Reynolds numbers of the main annulus flow, the configuration and the position of the rim seal with respect to the vanes and blades and the quantity of sealing flow injected inside the wheel-space.

Moreover, the development of the flow field under EI conditions within a stator-rotor cavity is schematically shown in Figure 1.7 for an axial rim seal. Here, the ingested hot gas is again indicated in red and the sealing air in blue. Specifically, Figure 1.7a depicts the general scenario in which the sealing flow is not sufficient to fully prevent the ingestion of hot gas while Figure 1.7b depicts the specific case in which the quantity of sealing flow ensures the complete sealing of the wheel-space. The purge flow supplied by the internal air system of the engine is injected inside the cavity to pressurize it and this results in the formation of a source region at low radius from which fluid is drawn into the rotor boundary layer. As the disk rotates, the fluid moves radially outwards becoming progressively thicker until a part of it is expelled into the turbine annulus. Close to the outer edge of the cavity, the hot gas from the main flow enters in the wheel-space (only in Figure 1.7a) where it mixes with the flow that recirculates inside the wheel-space, resulting in the formation of a mixing region. This mixture of hot and cold gas is then entrained into the boundary layer on the stator surface where it moves radially inwards. At the same time, it partially migrates in the axial direction from the stator towards the rotor side of the cavity. As a result, the thickness of the boundary layer on the stator side decreases in the negative radial direction and a core of recirculating flow is generated within the cavity [8, 10]. According to these observations, it may be concluded that, in the case of complete mixing within the outer mixing region, the temperature along the stator surface should remain approximately constant with radius. On the contrary, given

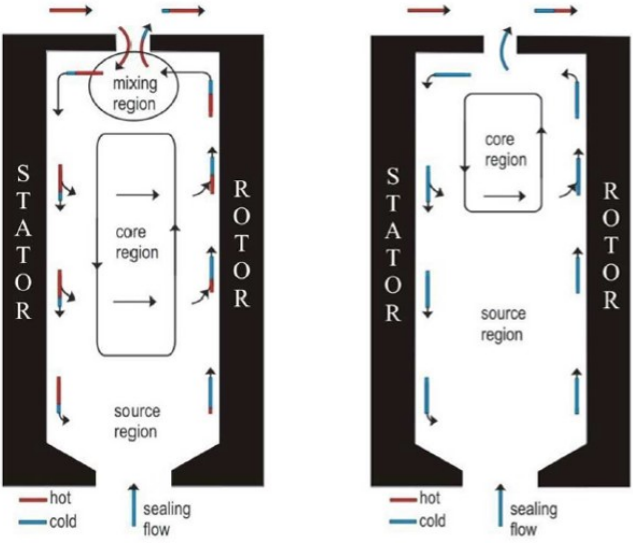

(a) Cavity with ingestion (EI) (b) Cavity fully sealed (EI)

Figure 1.7: Flow field within a stator-rotor cavity under EI conditions for the cases of (a) Cavity with ingestion and (b) Cavity fully sealed [8].

the progressive entrainment of the partially mixed flow that migrates in the axial direction, the average temperature of the rotor surface should rise as the radius increases. Despite this, as will be later shown in greater details, the sealing flow entrained inside the rotor boundary layer generates a buffer layer that further protects the rotor surface from the ingested hot gases [12, 13]. Thus, the resulting temperature on the rotor side is lower with respect to the stator side, although not radially constant. Then, the gradual injection of an increasing quantity of sealing flow rate causes the core region to reduce in size and move progressively upward until the fully sealed condition shown in Figure 1.7b is reached. Under such circumstances, the ingestion of hot gases is entirely prevented.

1.3.2 Rotationally-Induced ingress

Although EI ingress is usually considered to be the dominant ingestion mechanism in gas turbines, the ingress of hot gases can still occur even in the case of axisymmetric external flow in the turbine annulus, where no circumferential variations of static pressure are present. This type of ingestion is commonly referred to as Rotationally-Induced (RI) ingress [14] and it has been attributed to rotational effects of the fluid inside the wheel-space. In fact, the rotational motion of the fluid within the cavity creates a centripetal acceleration, giving rise to a radial pressure gradient which can lead to certain scenarios where the pressure within the wheel-space might fall below that in the flow path. Thus, this pressure difference induces the ingestion of fluid through the rim seal in correspondence of the stator disk while the disk-pumping effect simultaneously causes the egress of fluid in correspondence of the rotor disk [15].

The flow field that develops within the stator-rotor cavity under RI conditions is schematically shown in Figure 1.8 for an axial rim seal. Here, both the case with ingestion of hot gases (Figure 1.8a) and the case of fully sealed cavity (Figure 1.8b) have been reported. However, they will not be further discussed as they closely resemble those already described for the EI regime.

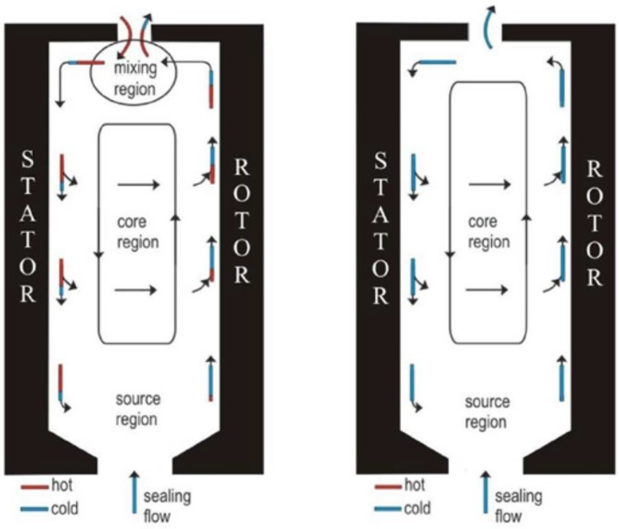

(a) Cavity with ingestion (RI) *(b) Cavity fully sealed (RI)*

Figure 1.8: Flow field within a stator-rotor cavity under RI conditions for the cases of (a) Cavity with ingestion and (b) Cavity fully sealed [15].

1.3.3 Combined Ingress

In many practical cases, engine designers only take into account the entity of the Externally-Induced ingress, as the impact of the RI ingress is often negligible if compared to that of EI ingress. However, there are some situations in which both the EI and RI ingress may play a significant role, as for example when the gas turbine is operated at off-design conditions [16, 17]. This type of ingestion is commonly referred to as Combined-Ingress (CI) [9, 18].

Another situation in which it is necessary to take into account the impact of RI ingress is the case of double rim seals. The flow field that develops within the stator-rotor cavity in a double radial rim seal is schematically shown in Figure 1.9. In particular, the outer seal is exposed to the variations in circumferential pressure created by the passage of the main flow over the vanes and blades resulting in EI ingress taking place through the outer seal. However, these pressure fluctuations are attenuated within the space between the two seals thus resulting in Combined-Ingress occurring through the inner seal. In the extreme case where such pressure asymmetry is entirely eliminated in the outer wheel-space, RI ingress occurs in the inner one [19].

As can be seen, the rim seal shown in Figure 1.9 is of the radial type. According to literature [11, 20], the radial configuration exhibits better sealing performance than the axial configuration shown in Figure 1.7 and 1.8. As will be better shown later in Chapter 2, the greater performance of the radial rim seal has been observed for both single and double configurations.

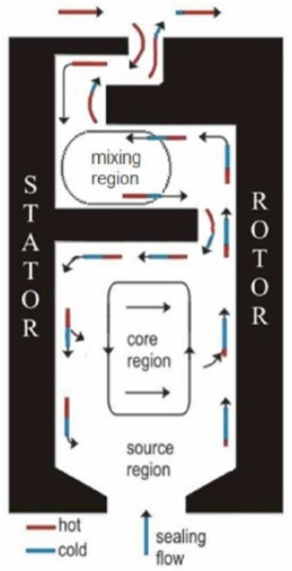

Figure 1.9: Flow field within a stator-rotor cavity for a double radial rim seal [11].

1.4 Thesis aims

The aim of this PhD thesis has been to design, commission and test a new Rotating Cavity Rig to experimentally investigate the problem of hot gas ingestion inside a stator-rotor cavity of a gas turbine. Such facility, which is the result of a collaboration between the University of Florence and Baker Hughes, is a single-stage test rig where both the stator and the rotor disks can accommodate replaceable cover plates that, despite some inevitable simplifications, have been specifically designed to replicate different engine rim seals as close as possible. The interchangeability and modularity of the covers allow replacing them with different geometries in order to investigate multiple arrangements. This will enable evaluating the impact of different geometrical parameters such as the axial overlap, the TE-LE distance and the radial gap on the sealing performance.

The test rig has been designed with the intent to operate at cold flow conditions. In addition to performing standard pressure and CO_2 concentration measurements within the cavity, specific optical accesses have been incorporated in the design in order to allow the exploitation of optical measurement techniques such as Pressure Sensitive Paint (PSP). Prior to this research, there were no documented cases in literature where PSP had been applied to investigate the phenomenon of hot gas ingestion. Hence, significant results were expected to be found on both the stator and the rotor sides of the cavity. In particular, achieving reliable results on the rotor surface represented one of the main objectives of this work, as traditional techniques like gas sampling measurements cannot be applied here due to the high rotational speed of the rotor.

Furthermore, the PSP allowed performing the analysis of the effect of different values of Density Ratio on the sealing performance of the rim seal. These results can be employed to extrapolate experimental data, typically collected at values of Density Ratio close to one, towards more representative engine conditions. In addition, they can also be used to calibrate simplified correlations and models that still represent a valid alternative to more expensive and time-consuming numerical simulations.

1.5 Thesis outline

The present work is organized into the following chapters:

- **Chapter** 1 → Introduction to the problem of hot gas ingestion which focuses on the primary mechanisms associated to the ingress of hot gases inside the stator-rotor cavities of gas turbines. In the end, the thesis objectives are outlined along with a list of publications that have arisen from the research conducted in this work.

- **Chapter** 2 → Detailed literature review on the problem of hot gas ingestion which provides a comprehensive description of the theoretical models and the experimental facilities that have been developed throughout the years to investigate the ingestion phenomenon. Additionally, the chapter introduces several useful adimensional parameters that will be later employed to discuss the obtained results.

- **Chapter** 3 → Presentation of the Rotating Cavity Rig and definition of the operating conditions with respect to the other test rigs available in literature. The different components that make up the facility are initially described in order to understand the overall layout of the test rig and then a detailed explanation of the design procedure is provided. First, the CFD analyses conducted to perform the fluid dynamic design of both the flow path and the feeding system are presented. Subsequently, a significant number of static-structural, dynamic-modal and dynamic-harmonic FEM analyses are discussed to verify the suitability of the chosen layout in terms of stress, deformation and vibration values.

- **Chapter** 4 → Description of the installation of the test rig inside the laboratory test cell and verification of the correct assembly of the facility. Then, the different rim seal configurations that have been tested in this study are shown and described. Subsequently, the instrumentation of the test rig is described in detail, illustrating all the measurement points present in the facility. Special attention is reserved to the description of the innovative setup that has been developed to carry out PSP measurements on both the stator and the rotor sides of the cavity. The last part of the chapter is dedicated to the description of a series of commissioning tests that were conducted to ensure the correct and safe operation of the test rig.

- **Chapter** 5 → Description of the experimental results obtained through the use of gas sampling measurements starting from the complete characterization of the baseline configuration at both design and off-design conditions. Subsequently, the experimental campaign was extended to the study of other six rim seal configurations to determine the impact of different geometric parameters on the sealing performance of the cavity. In particular, the study will focus on assessing the influence of different values of axial overlap, different distances between the vanes TE and the blades LE and different values of radial gap.

- **Chapter** 6 → Description of the experimental results obtained through the use of PSP by using pure N_2 as purge flow. First, the contours obtained on the stator side of the cavity are compared with the effectiveness values previously obtained through standard CO_2 concentration measurements in order to validate the application of the PSP technique for the study of hot gas ingestion. Subsequently, the validated PSP setup was used to obtain 2D effectiveness maps also on the rotor side. Finally, the results obtained on both sides of the cavity are correlated with each other by performing sealing effectiveness measurements across the cavity width through the use of a concentration probe.

- **Chapter** 7 → Description of the impact of the DR on the sealing performance of the rim seal through the analysis of the experimental results obtained by using the PSP technique with either pure N_2 ($DR = 1$) or pure CO_2 ($DR = 1.52$) as purge flow. Therefore, the experimental data points gathered from both the stator and the rotor sides of the cavity are respectively fitted by using either a modified version of the Orifice Model that explicitly includes the effect of the Density Ratio or the Buffer Ratio model. In the end, this will enable evaluating the influence of the Density Ratio on the sealing performance of the rim seal and on the low-order models employed to perform the data analysis.

1.6 Publications

The content of Chapter 5 is expected to lay the groundwork for an upcoming publication while the rest of this work has led to the publication of the following conference/journal papers:

- Orsini, L., Picchi, A., Bonini, A., Innocenti, L., Di Benedetto, D., Da Soghe, R., and Mazzei, L. “Design procedure of a rotating cavity rig for hot gas ingestion investigation.” ASME Paper No. GT2022-82676, 2022.

- Orsini, L., Brocchi, S., Picchi, A., Facchini, B., Bonini, A., and Innocenti, L. “Commissioning of a newly designed experimental facility for hot gas ingestion investigation.” ETC Paper No. ETC2023-263, 2023.

- Orsini, L., Picchi, A., Facchini, B., Bonini, A., and Innocenti, L. “On the use of pressure-sensitive paint to determine the rim sealing effectiveness.” J. Turbomach, 146(2), October 2023.

- Orsini, L., Picchi, A., Facchini, B., Bonini, A., and Innocenti, L. “Impact of the purge flow density ratio on the rim sealing effectiveness in hot gas ingestion measurements.” J. Turbomach, 146(2), October 2023.

Chapter 2

Literature review

Contents

2.1 Background overview

The ingestion of hot gases into the enclosed space located between the rotating and stationary components of a gas turbine generally involves 3D and possibly unsteady fluid dynamics mechanisms. Therefore, the rotating flow that occurs inside stator-rotor cavities usually appears to be highly complex and a thorough investigation is often required to understand its behaviour. For this reason, this chapter starts with a brief explanation of the fluid dynamics within rotating systems in order to provide a groundwork useful to understand the subsequent sections. Afterwards, a much more detailed literature review regarding both past and current research will be presented, distinguishing between the main regimes connected to the problem of hot gas ingestion: Rotationally-Induced (RI) and Externally-Induced (EI).

For the aim of this work, this review will be specifically focused on the description of the different test rigs that have been developed throughout the years to experimentally characterize the sealing performance of rim seals. As a matter of fact, experimental results are greatly relevant up to the present day since fundamental test cases, which replicate actual engine geometries, still represent a widely used approach to calibrate correlations and simplified models. In fact, although theoretical models allow for a quick yet highly effective analysis of the data, they usually require an experimental calibration to provide accurate and reliable results. Although different models have been formulated over the course of time, the Orifice Model (OM) developed by the University of Bath is among the most renowned and, for this reason, it will be later explained in detail. Nowadays, a highly detailed description of the fluid dynamic behaviour of stator-rotor cavities can also be provided by very complex and time-consuming CFD simulations. However, despite representing an essential instrument for the development of increasingly efficient engines, numerical simulations can still be affected by significant uncertainties. Therefore, they usually require an experimental validation to ensure that the obtained results are reliable.

2.2 Simple disk rotating in free air

One of the most basic cases of rotational flow motion is known as the "free disk" case and it involves a simple disk freely spinning within an undisturbed environment. Such scenario is illustrated in Figure 2.1 where a free disk of radius r_{disk} is spinning with uniform angular velocity Ω. Due to friction, the undisturbed flow is accelerated from zero velocity in the free-stream up to the tangential velocity $V_\phi = \Omega \cdot r$ at the surface of the disk, thus satisfying the no-slip condition in the rotor boundary layer that forms as a result of the shearing motion of the fluid. Since the fluid within the boundary layer moves radially outward with a velocity V_r due to the centrifugal force generated as a consequence of the rotation of the disk, the surrounding fluid is continuously drawn in the axial direction, assuming a velocity V_z, in order to satisfy the conservation of mass. This process, in which the fluid of the free-stream is constantly entrained in the boundary layer and then pumped up towards the periphery of the rotating disk, is known as the "free disk pumping effect". It should be noted that, although Figure 2.1 shows only one side of the disk, it is

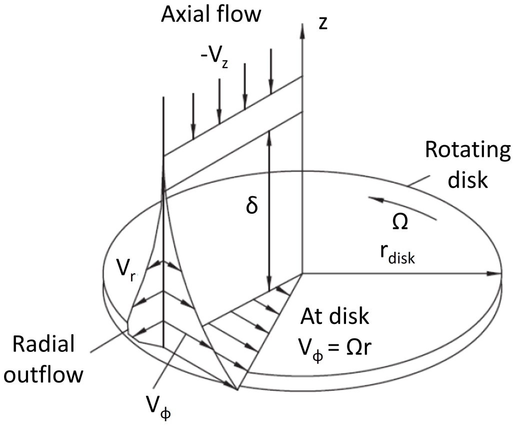

Figure 2.1: Simple disk rotating in free air. Adapted from Childs [21].

evident that the same behaviour occurs on both sides due to symmetry reasons. Furthermore, as noted by Childs [21], the flow near the axis of rotation is typically in a laminar regime regardless of the value of Ω. As the radius increases, the appearance or not of a transitional region leading to turbulent flow is generally a function of the value of the local rotational Reynolds number, defined as follows:

$$Re_{\phi,local} = \frac{\rho \cdot \Omega \cdot r^2}{\mu} \tag{2.1}$$

where ρ is the density of the fluid, r represents the local radius on the surface of the rotating disk and μ is the dynamic viscosity of the fluid. Despite a characteristic value of $Re_{\phi,local} = 2 \times 10^5$ typically indicates the onset of transitional flow, this phenomenon is also influenced by other parameters such as the smoothness of the disk surface.

2.3 Stationary disk in a rotating fluid

Before moving on to the analysis of more complex stator-rotor systems, it is also useful to examine the scenario where a stationary disk is immersed in a rotating flow. Such scenario is illustrated in Figure 2.2 where a stationary disk of radius r_{disk} is immersed in a flow spinning outside of the boundary layer with uniform angular velocity Ω. The rotating flow remains in steady-state conditions under the effect of the centrifugal force which thus gives rise to the appearance of a pressure gradient. Approaching the stationary disk, the flow is decelerated from the free-stream velocity $V_\phi = \Omega \cdot r$ to zero at the surface of the disk, in accordance with the no-slip condition, thus causing a corresponding decrease in the local centrifugal force. The flow within the boundary layer moves radially inward with a velocity V_r due to the effect of the pressure gradient. Moreover, an axial flow with velocity V_z moves away from the surface of the disk towards the core of the rotating fluid. Hence, in order to satisfy the conservation of mass, air from the surrounding free-stream is drawn into the boundary layer from the outer edge of the disk. As before, Figure 2.2 shows only one side of the disk due to the symmetry of the problem.

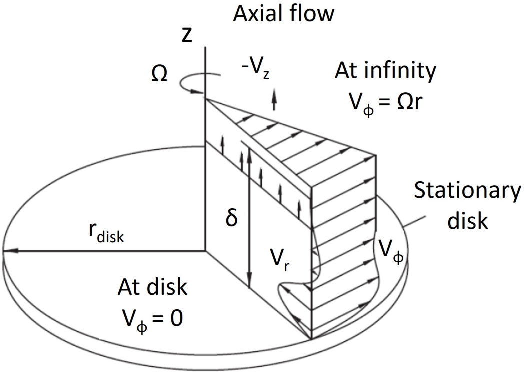

Figure 2.2: Stationary disk in a rotating fluid. Adapted from Childs [21].

2.4 Rotor-Stator system

The combination of both the cases described above leads to the definition of a more complex system, where a rotating disk is positioned near a stationary casing. This system, which represents the typical configuration of a gas turbine stage, is known as rotor-stator system. As illustrated in Figure 2.3, such configuration includes a rotor disk and a stator disk, both with a radius equal to r_{disk}, separated by an axial width S that creates a cavity commonly known as wheel-space. Additionally, it is worth noting the presence of additional features, including the possible presence of a stator or rotor shroud positioned at the periphery of the disks and the potential supply of sealing flow near the axis of rotation.

The first theoretical models attempting to explain the behaviour of the flow within the wheel-space date back to the 1950s, when detailed experimental data or complex numerical simulations were not yet available. In particular, the first model was proposed in 1951 by Batchelor [22] who suggested that a rotating inviscid fluid core would develop inside the cavity, rotating at an angular velocity ranging from zero to Ω. Consequently, two boundary layers would form within the wheel-space: one on the rotor

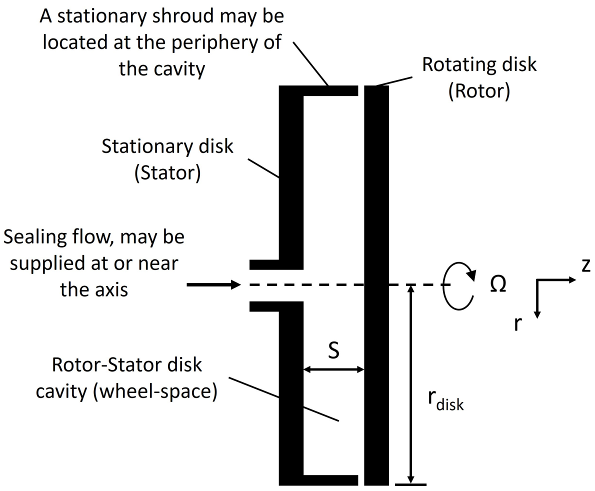

Figure 2.3: Rotor-stator system. Adapted from Childs [21].

surface similar to that described for the case of free disk (Section 2.2), and one on the stator surface resembling that described for the case of stationary disk immersed in a rotating fluid (Section 2.3). This results in the stator boundary layer being fed from the fluid at the periphery of the cavity which then moves radially inward. This flow would thus move axially away from the stator surface to support the rotating core. In contrast, the rotor boundary layer would be axially fed by the flow originating from the rotating core while being pumped radially outward by the rotating disk. This type of flow structure is commonly known as the Batchelor flow model.

A different flow model was proposed in 1953 by Stewartson [23], who presented an alternative description of the flow field developing within the rotor-stator system. In the Stewartson flow model, the flow field resembled that of a free disk, where the tangential velocity component of the fluid matched the rotational velocity of the disk, $V_\phi = \Omega \cdot r$, within the rotor boundary layer. Then, the velocity would gradually decrease in the axial direction until it would become zero on the stator surface.

Stewartson derived these observations from theoretical calculations and experiments and concluded that a flow behaviour of such kind would not require the development of a boundary layer on the stator surface. Hence, a rotating fluid core would not exist within the wheel-space.

The characteristic velocity profiles that would develop in a rotor-stator wheel-space according to both the Batchelor and the Stewartson flow models have been summarised by Childs [21] and they are reported in Figure 2.4. In particular, according to the model developed by Batchelor, the tangential velocity (Figure 2.4a) undergoes a rapid change within both boundary layers while maintaining a constant trend in the rotating core as the axial distance z/S from the surface of the rotor disk varies. The behaviour of the radial velocity component (Figure 2.4b) highlights a radial outflow on the rotor and a radial inflow on the stator, while it

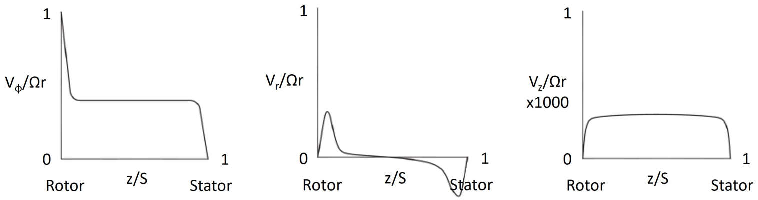

(a) Batchelor - Tangential velocity *(b) Batchelor - Radial velocity* *(c) Batchelor - Axial velocity*

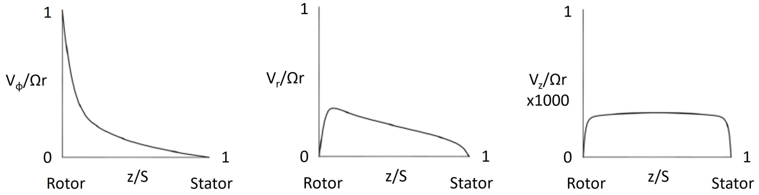

(d) Stewartson - Tangential velocity *(e) Stewartson - Radial velocity* *(f) Stewartson - Axial velocity*

Figure 2.4: Characteristic velocity profiles in a rotor-stator wheel-space. Batchelor flow model: (a) Tangential velocity, (b) Radial velocity and (c) Axial velocity. Stewartson flow model: (d) Tangential velocity, (e) Radial velocity and (f) Axial velocity. Adapted from Childs [21].

approaches a value close to zero in the core. The axial velocity (Figure 2.4c) remains almost constant within the cavity. Regarding the model developed by Stewartson, the tangential velocity component (Figure 2.4d) gradually decreases from its maximum value $V_\phi = \Omega \cdot r$ on the rotor surface to zero on the stator surface. The behaviour of the radial velocity (Figure 2.4e) highlights that the entire wheel-space experiences radial outflow, which decreases in intensity approaching the stator. Lastly, similar to the Batchelor flow model, the axial velocity (Figure 2.4f) maintains a constant trend within the wheel-space.

The existence of these two conflicting models gave rise to what is known as the Batchelor-Stewartson controversy and the determination of the validity of one model over the other was found to be depending on the flow conditions only through subsequent experimental observations. Picha and Eckert ([24]) indeed demonstrated that for a rotor-stator system equipped with shrouds positioned at the periphery of the disks, as typically found in a gas turbine stage, the rotating core did indeed exist, highlighting that the Batchelor flow model was the most accurate to describe the flow structure developing in this type of configuration. The same authors conducted further experiments, showing that the rotating core does not seem to be present when the disks are instead open to the atmosphere (without shrouds) or when the sealing flow injected inside the cavity is high enough to suppress the presence of the rotating core. In the latter cases, the Stewartson flow model was thus identified as the one that best describes the flow behaviour within the wheel-space. A few years later, in 1996, the presence of the rotating core and the trends of tangential and radial velocities predicted by the Batchelor flow model were confirmed by Chen et al. [25] who employed a rotor-stator configuration equipped with a shroud on the stator side to conduct experimental measurements by using Laser Doppler Anemometry (LDA). The measurements were taken in the absence of sealing flow and extensive data was collected at various axial positions within the cavity. As illustrated in Figure 2.5, both the tangential (Figure 2.5a) and the radial (Figure 2.5b) velocity trends are in agreement with the flow structure predicted by Batchelor. The presence

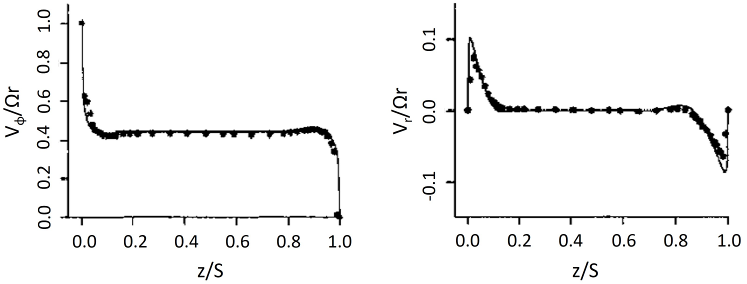

(a) Tangential velocity *(b) Radial velocity*

Figure 2.5: Characteristic velocity profiles in a rotor-stator wheel-space obtained by using the LDA technique: (a) Tangential velocity and (b) Radial velocity. Adapted from Chen et al. [25].

of a non-viscous rotating core within the wheel-space is thus confirmed by the nearly constant behaviour of both the velocity components as the axial distance z/S from the surface of the rotor disk varies.

Furthermore, it is important to note that for a Batchelor-type flow, where a non-viscous core rotates within a cavity with separated boundary layers, the development of the flow field is primarily governed by two non-dimensional parameters: the swirl ratio β (Eq. 2.2) and the turbulent flow parameter λ_{turb} (Eq. 2.3). As extensively described by Owen and Rogers [26], the ratio between the tangential velocity of the flow, V_ϕ, and the angular velocity of the rotor, Ω, defines the swirl ratio:

$$\beta = \frac{V_\phi}{\Omega \cdot r} \tag{2.2}$$

Meanwhile, the turbulent flow parameter is defined as:

$$\lambda_{turb} = C_w \cdot Re_\phi^{-0.8} \tag{2.3}$$

where Re_ϕ is the rotational Reynolds number:

$$Re_\phi = \frac{\rho \cdot \Omega \cdot r_{disk}^2}{\mu} \tag{2.4}$$

which is derived from Eq. 2.1 by imposing $r = r_{disk}$ and C_w is referred to as the non-dimensional sealing flow rate which is defined as:

$$C_w = \frac{\dot{m}}{\mu \cdot r_{disk}} \tag{2.5}$$

where $\dot{m}$ represents the mass flow rate of the sealing flow injected inside the cavity. Therefore, the results obtained by Owen and Rogers [26] demonstrated that using the parameter λ_{turb} allows obtaining a good prediction of the flow structure that develops within the wheel-space. In particular, they demonstrated the existence of a critical level of sealing flow, identified by the value $\lambda_{turb} = 0.22$, beyond which the rotating core is supposedly suppressed and the transition from a Batchelor-type flow to a Stewartson-type flow may occur.

In conclusion, Daily and Nece [27] performed a detailed study of the flow structures that develop inside an enclosed rotor-stator system in the absence of superposed flow. By combining theoretical and experimental investigations, the flow structures that develop within the wheel-space were classified into four categories depending on the value assumed by Re_ϕ and by the axial gap ratio G, which is defined as:

$$G = \frac{S}{r_{disk}} \tag{2.6}$$

where S represents the axial width between the stator and the rotor surfaces. The four possible flow regimes that can establish in a rotor-stator system without superimposed sealing flow rate are shown in Figure 2.6 and they can be described as follows:

- **Regime I** → The flow is laminar (low Re_ϕ) and the axial spacing is small (low G). The flow is of the Couette type and the boundary layers on the rotor and stator surfaces are merged together. Furthermore, if Re_ϕ is kept constant, an increase in G results in a reduction in the frictional heating on the rotor;

- **Regime II** → The flow is laminar (low Re_ϕ) and the axial spacing is large (high G). In this case, the boundary layers on the stator and rotor are separated from each other, leading to the creation of a rotating core. The effect of the stator is to reduce the rotation of the core. Consequently, the resulting frictional heating is lower than that observed for a free disk;

- **Regime III** → The flow is turbulent (high Re_ϕ) and the axial spacing is small (low G). Flow structure similar to Regime I;
- **Regime IV** → The flow is turbulent (high Re_ϕ) and the axial spacing is large (high G). Flow structure similar to Regime II;

Although these regimes were identified in the absence of sealing flow, they would be similar in presence of a superposed flow. However, the amount of injected flow will have an additional effect on the flow structures that develop within the wheel-space. For example, Owen and Rogers [26] suggested that in presence of a superposed flow, the transition from laminar to turbulent flow would occur at lower values of Re_ϕ.

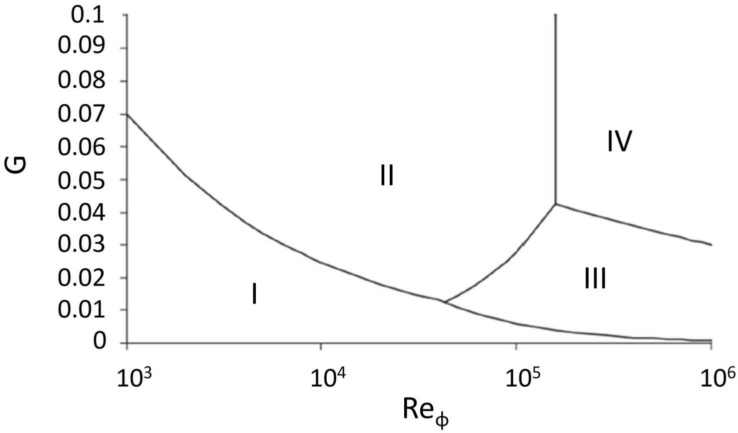

Figure 2.6: Flow regimes developing inside an enclosed rotor-stator system with no superposed flow. Adapted from Daily and Nece [27].

2.5 Literature review on RI ingress

The early studies regarding the phenomenon of hot gas ingestion primarily focused on the case of Rotationally-Induced ingress and only years later the attention shifted towards the case of Externally-Induced ingress. At the University of Sussex, Bayley and Owen [28] were among the first, in 1970, to conduct an experimental study by using a rotor-stator system. The test rig, shown in Figure 2.7, featured a 30-inch diameter rotor disk which could be spun up to 4500 RPM. The rotor was axially separated from the shrouded stator disk by a variable gap $s_{c,ax}$. The sealing flow, $C_{w,0}$, was injected into the cavity through the center of the stator disk and flowed radially outward until it was discharged through the axial rim seal into quiescent atmosphere, given the absence of mainstream annulus flow. The resulting flow rotation within the wheel-space led to the formation of a radial pressure gradient, causing the system to operate under sub-atmospheric conditions within the cavity. Consequently, this allowed the system to ingest external air into the cavity, leading to the

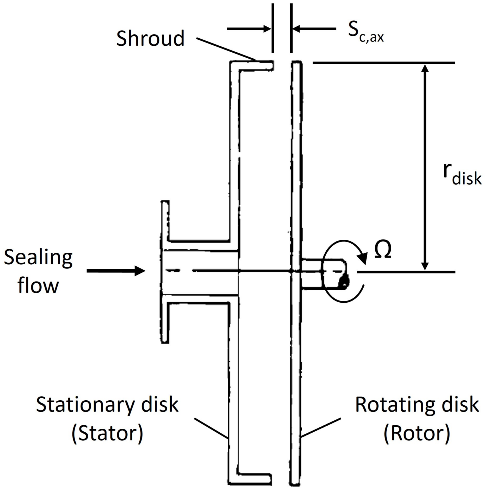

Figure 2.7: Rotor-stator system. Adapted from Bayley and Owen [28].

establishment of the RI regime. The experiments conducted by Bayley and Owen aimed to determine the minimum value of sealing flow rate, $C_{w,min}$, required to fully seal the cavity. Hence, they performed static pressure measurements on the surface of the stator disk while gradually increasing the amount of sealing flow injected into the cavity. The gradual increase in pressure within the wheel-space resulted in a progressive reduction in the amount of ingested air until, at relatively high sealing flow rates, the ingress of air was completely prevented. The results obtained from this experimental investigation allowed the authors to derive an empirical correlation, known as the "Bayley-Owen criterion for RI ingress", that could be used to estimate the minimum non-dimensional sealing flow rate needed to prevent ingestion in the RI case:

$$C_{w,min,RI} = 0.61 \cdot G_c \cdot Re_\phi \tag{2.7}$$

This expression is valid for $Re_\phi \leq 4 \times 10^6$ and $G_c \ll G$ and it highlights that $C_{w,min}$ is proportional to the rotational Reynolds number, Re_ϕ, and to the seal clearance ratio, G_c, which is defined as follows:

$$G_c = \frac{s_{c,ax}}{r_{disk}} \tag{2.8}$$

The experimental results used to derive the correlation reported in Eq. 2.7 are summarised in Figure 2.8 where the measured values of $C_{w,min}$ are plotted as a function of Re_ϕ for different values of axial gap ratio (G) and seal clearance ratio (G_c). By observing the reported trends it is clear that $C_{w,min}$ tends to increase with Re_ϕ. Moreover, it is also evident that greater values of G_c require higher values of $C_{w,min}$ to reach the fully sealed condition while the axial gap ratio G appears to have only a minor influence on the results. Actually, the test rig employed in this study represents an upgrade of the model used by the same authors in 1969 [29] to describe the flow behaviour within the wheel-space. However, since the test rig used in 1969 had an unshrouded stator, the results described in the 1970 work proved to be of greater relevance for the application to gas turbines.

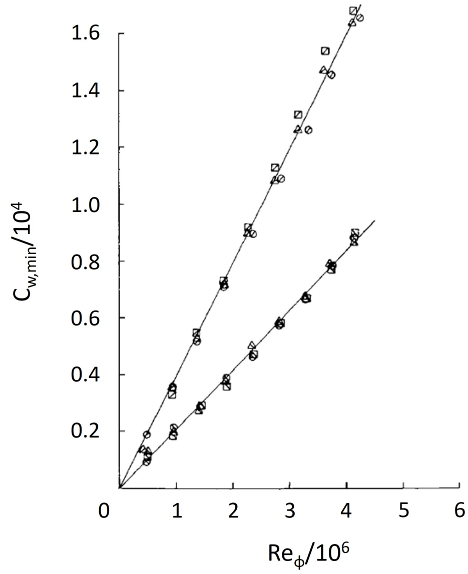

Experiment	G	G_c
⦸	0.06	0.0033
⊘	0.06	0.0067
⧅	0.12	0.0033
⧄	0.12	0.0067
△	0.18	0.0033
△	0.18	0.0067

Figure 2.8: Measured values of $C_{w,min}$ plotted as a function of Re_ϕ for different values of axial gap ratio (G) and seal clearance ratio (G_c). Adapted from Bayley and Owen [28].

In 1983, Phadke and Owen [30] extended the research on RI ingress in rotor-stator systems. The test rig used for their study allowed them to employ the different rim seal geometries reported in Figure 2.9 to investigate different axial and radial clearances. In particular, they tested one axial configuration (configuration A) and four radial configurations (configurations B, C, D and E). Once again, the experiments were conducted in the absence of mainstream annulus flow and static pressure measurements were used as the criterion to assess the ingress of air inside the wheel-space. Additionally, they also employed the flow visualization technique by injecting oil particles into the sealing flow to investigate the variation of the minimum non-dimensional sealing flow rate required to prevent ingestion for different values of G_c and Re_ϕ.

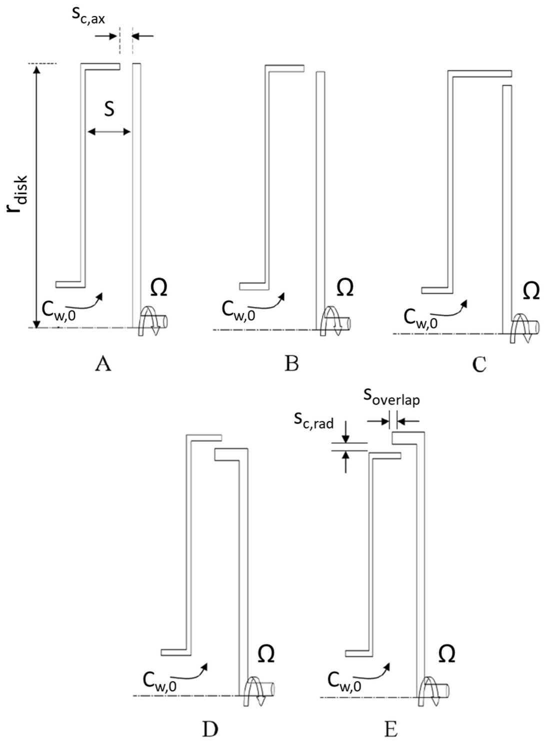

Figure 2.9: Different rim seal geometries: one axial configuration (A) and four radial configurations (B, C, D and E). Adapted from Phadke and Owen [30]

For the radial rim seal configurations labelled as C and D, where the stationary shroud overlaps the rotor, it was observed that the pressure within the cavity increased instead of decreasing as Re_ϕ increased. This phenomenon, referred to as the "pressure-inversion effect", was not observed in the case of axial-clearance configurations and it was also noticed that this effect became more pronounced as the degree of overlap between the stationary shroud and the rotor increased. Although the authors proposed different theories to explain this phenomenon, they did not provide a definitive explanation. As shown in Figure 2.10, when comparing the results of the axial rim seal with those obtained for radial ones under equivalent conditions, it becomes evident that a seal with a radial clearance requires a smaller quantity of sealing flow to prevent ingress compared to one with an axial clearance, making the pressure inversion effect beneficial in reducing $C_{w,min}$.

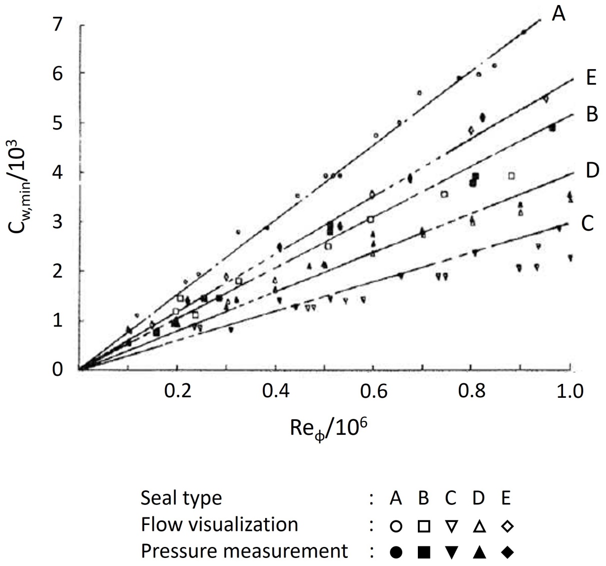

Figure 2.10: Variation of $C_{w,min}$ with Re_ϕ for five different rim seal geometries. Adapted from Phadke and Owen [30].

The use of gas concentration measurements to determine the effectiveness in different rim seal geometries was first proposed in 1987 by Graber et al. [31] and then in 1992 by Daniels et al. [32]. The rotating test rig used to perform the experiments consisted of a rotor-stator system in which only the rotor disk included a shroud. In this case, the experiments were conducted with mainstream flow present in the annulus and two different values of swirl ratio β were investigated. However, given the very low flow rate (< 0.03 m/s) and the absence of any indication regarding the presence of circumferential pressure fluctuations in the annulus, it is plausible to assume that the flow exhibited a high degree of axisymmetry, as suggested by Owen [14]. Consequently, any ingestion that occurred could be likely attributed to rotational effects, implying that only RI ingress occurred. The sealant flow, injected into the wheel-space from the stator side, was seeded with CO_2 and concentration measurements were performed at various radial positions on the stator surface. In the event of a completely sealed cavity, the concentration value measured on the stator wall would be equal to the value measured at the sealant flow inlet. Hence, the concentration effectiveness was defined as follows:

$$\varepsilon_c = \frac{c_S - c_{an}}{c_0 - c_{an}} \tag{2.9}$$

where c_S, c_{an} and c_0 respectively represent the concentration of CO_2 at a given radial position on the stator surface, in the annulus and at the sealant flow inlet. Hence, the cavity can be considered fully sealed when $\varepsilon_c = 1$. The experiments were conducted on a range of different rim seal geometries with axial or radial gaps and the obtained results appeared to be in good agreement with those of Phadke and Owen [30], providing further confirmation that the effect of the main annulus flow was negligible. In Figure 2.11, the results in terms of effectiveness are compared for two rim seals with different radial clearances: the dots represent the baseline configuration used as a reference while the triangles represent a configuration with half the radial clearance (dimensions are in inches). As can be observed, reducing the radial clearance leads to an increase in effectiveness for the same amount of sealing flow injected into the cavity. Alternatively, it can be stated that the sealing flow required to achieve a certain level of effectiveness decreases as the radial clearance decreases. Furthermore, in Figure 2.12, the baseline configuration is compared with a rim seal without axial overlap (stator and rotor are on-line). Once again, the dots represent the baseline case while the triangles indicate the different geometry used for the comparison. By observing this figure, it can be concluded that increasing the overlap results in a

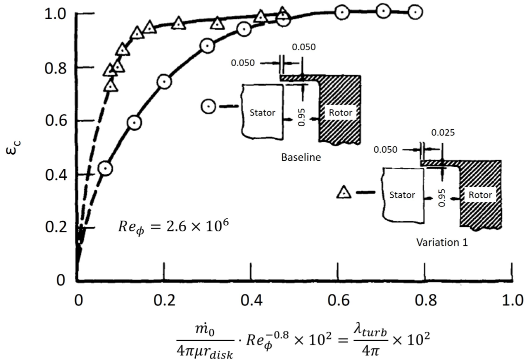

Figure 2.11: Variation of ε_c with coolant flow rate for two rim seals with different values of radial clearance. Adapted from Graber et al. [31].

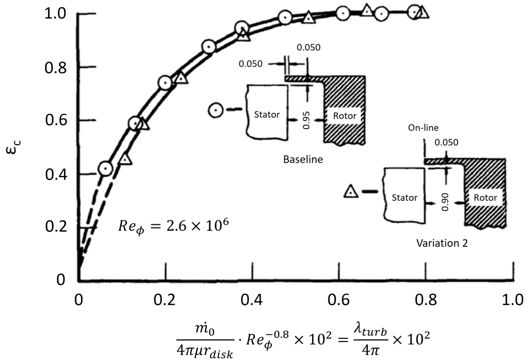

Figure 2.12: Variation of ε_c with coolant flow rate for two rim seals with different values of axial clearance. Adapted from Graber et al. [31].

slight increase in the effectiveness values, although such improvement is much smaller than the one achieved by reducing the radial clearance. In general, by examining the effectiveness curves presented in Figures 2.11 and 2.12, it can be observed that there is usually an initial rapid increase in performance until an effectiveness value of $\varepsilon_c = 0.80$ is reached and then the trend becomes asymptotic, thus requiring double the amount of sealing flow rate already injected to achieve $\varepsilon_c = 1$. Therefore, this explains why gas turbine rim seals are often designed to not completely prevent ingestion but rather to allow acceptable disk temperatures, resulting in a significant reduction in the required sealant flow rate. Finally, it was shown that not all the studied rim seal configurations were subject to the same proportionality constant indicated by Bayley and Owen [28] in Eq. 2.7. Instead, their behaviour depended on different factors such as the specific geometric characteristics of the rim seal, the rotational Reynolds number and the presence or absence of external flow.

In 1988, Phadke and Owen [33] included N_2O gas concentration measurements to the series of techniques previously implemented in their test rig in order to further advance the research on RI ingress. Therefore, this led to the utilization of three distinct approaches to determine the level of ingress: pressure measurements, flow visualization through smoke injection and gas concentration measurements. The experiments were carried out on a rotor-stator test rig which was placed in a still environment, thus in the absence of external flow. In addition, a more extensive array of geometries than those employed by the same authors [30] in 1983 was investigated, including axial, radial and double clearance rim seals. In all the studied configurations, which are shown in Figure 2.13 along with the flow patterns identified by using the flow visualization technique, the sealing flow was injected from the center of the stator disk. This flow then impinged on the rotor surface, moved radially outward and left the cavity through the clearance. From the performed measurements it was observed that, as both the rotational speed and the seal clearance increased, a greater amount of sealing air was required to prevent the ingestion of external flow. Furthermore, the ”pressure inversion effect” previously described by the same authors was once again identified in configurations 4 and 5. In these cases, above a certain sealing flow rate, the pressure inside the cavity was observed to be increasing rather than decreasing as the rotational speed increased. Through the use of flow visualization, it was possible to attribute this previously unexplained phenomenon to the presence of a recirculation zone near the clearance which was gen-

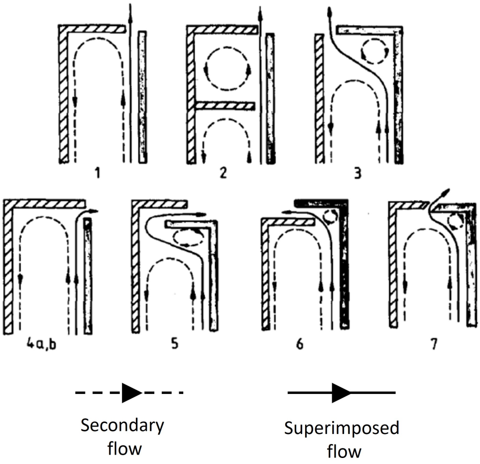

Figure 2.13: Simplified representation of the flow patterns identified through flow visualization for seven investigated rim seal configurations. Adapted from Phadke and Owen [33].

erated by the impingement of the radially pumped flow on the stator disk. Therefore, this recirculation zone caused an increase in pressure inside the cavity which helped to prevent the ingestion of external flow. The pressure measurements performed within the wheel-space allowed the authors to determine that, given a certain value of C_w, there is a critical value of Re_ϕ beyond which the pressure inside the cavity changes from higher to lower values than those in the annulus and after this change the ingestion of external flow occurs. Moreover, it was observed that the quantity of ingested flow increases as C_w decreases and it is also proportional to the values of Re_ϕ and G_c. The effect of the latter on the variation of $C_{w,min}$ with Re_ϕ was therefore investigated by using flow visualization and the results obtained for an axial rim seal (configuration 1) are presented in Figure 2.14. As can be seen, the amount of sealing flow required to prevent the ingestion increases linearly with Re_ϕ for all the investigated values of G_c, although larger clearance gaps lead to a more rapid increase. This linearly increasing trend, consistent with the results previously found by Bayley and Owen [28], was also found for all the other tested configurations. However, a comparison of the performance of the different geometries allowed them to confirm that radial rim seals are more effective than axial ones in preventing the ingestion of air.

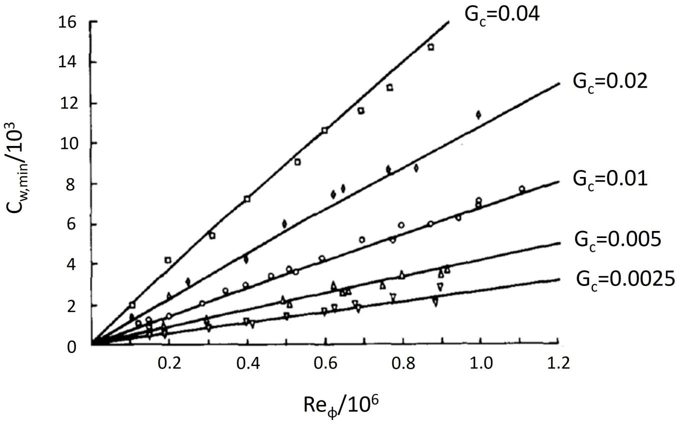

Figure 2.14: Variation of $C_{w,min}$ with Re_ϕ for different values of G_c (configuration 1). Adapted from Phadke and Owen [33].

In 1991, Chew [34] attempted to develop a theoretical model that could be used to describe the ingestion of air in the RI case. In particular, he proposed a mathematical model in which the behaviour of the boundary layer within the cavity, which could be described through an integral momentum approach, was linked to the behaviour of the rim seal, which was instead considered as a simple orifice. The model was then used to estimate the minimum flow necessary to prevent the ingestion of air inside the cavity and the predicted values were found to agree reasonably well with the experimental findings of Bayley and Owen [28], Phadke and Owen [30, 33] and Graber et al. [31]. Moreover, the model showed that the quantity of ingested air is generally roughly equal to 20% of the minimum flow rate required to fully seal the system, $C_{w,min}$.

Then, in 1992 Chew et al. [35] reviewed the model again, taking into consideration recently acquired data from Dadkhah et al. [36] who performed measurements of static and total pressure along with gas concentration in a 1.5-stage test rig developed at the University of Sussex. The facility, capable to operate with axisymmetric annulus flow but not equipped with vanes and blades, included two radial rim seals: Figure 2.15a denotes the upstream wheel-space equipped with rim seal A while Figure 2.15b denotes the downstream wheel-space equipped with rim seal B. Although pressure measurements indicated that $C_{w,min}$ was lower for rim seal A compared to rim seal B, according to concentration measurements the amount of ingestion for rim seal A was greater than that for rim seal B. This discrepancy was attributed to the different relative position between the stator and rotor disks and the two rim seals, as the direction of the main flow was from the stator to the rotor for configuration A and vice versa for configuration B. Therefore, the authors were led to conclude that the value of $C_{w,min}$ and thus the ingestion phenomenon are influenced by the mainstream flow. Hence, this study was among the first, along with that of Abe et al. [37] and Phadke and Owen [33], to suggest the possible existence of an Externally-Induced regime in addition to the Rotationally-Induced one.

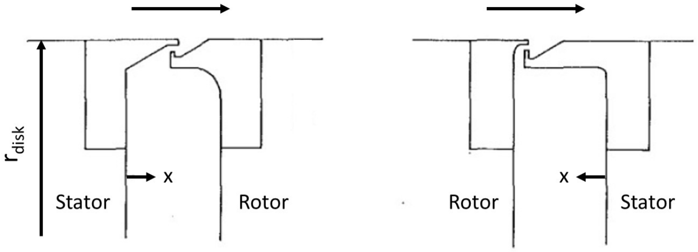

(a) Upstream wheel-space (b) Downstream wheel-space

Figure 2.15: Representation of the (a) Upstream wheel-space equipped with rim seal A and (b) Downstream wheel-space equipped with rim seal B. Adapted from Dadkhah et al. [36].

In recent years, further research into the ingestion of hot gases has been carried out at the University of Bath. In order to investigate the phenomenon of RI ingress, Sangan [11, 15] performed an extensive experimental campaign on a single-stage test rig equipped with 32 stator vanes and 41 rotor blades. Several gas concentration measurements were performed where the annulus exit was left open to the atmosphere while the inlet was closed to prevent the potential generation of swirl in the main flow due to the rotation of the rotor. The resulting values of sealing effectiveness ε_c were then derived from the concentration measurements by applying Eq. 2.9. Hence, the obtained variation of ε_c with the nondimensional sealing flow rate $C_{w,0}$ is reported in Figure 2.16, where the performance of a radial rim seal (open symbols) is compared with that of an axial rim seal (solid symbols). Moreover, symbols with different shapes highlight the effect of Re_ϕ on the two different rim seals. As can be seen, as the quantity of injected sealing flow increases, the cavity pressurizes thus reducing the amount of ingested flow (ε_c increases).

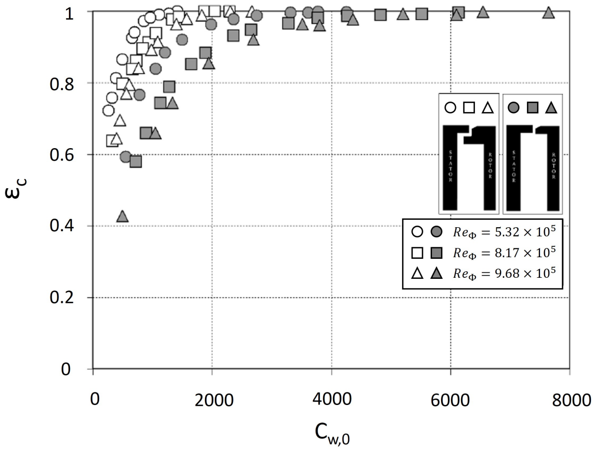

Figure 2.16: Variation of ε_c with $C_{w,0}$ for a radial rim seal (open symbols) and an axial rim seal (solid symbols). Adapted from Sangan et al. [15].

Furthermore, despite both rim seals experience a decrease in ε_c as Re_ϕ increases, the radial rim seal has a better performance than the axial one. According to these trends, it becomes evident that different correlations are needed to assess both the effects of G_c and Re_ϕ on ε_c. To ease the comparison between different geometries and operating conditions, the obtained results have been also plotted in Figure 2.17 as a function of a new parameter called the non-dimensional sealing parameter Φ:

$$\Phi_0 = \frac{C_{w,0}}{2\pi \cdot G_c \cdot Re_\phi} \tag{2.10}$$

which combines together the effects of C_w, G_c and Re_ϕ. As can be seen, all the obtained data collapse onto a single curve for each of the two rim seals. According to this observation, it can be stated that different values of rotational speed do not have an impact on the results expressed in terms of Φ. Furthermore, the obtained results show that the radial rim seal requires approximately 38% of the sealing flow required by the axial rim seal to fully seal the cavity and thus prevent RI ingress.

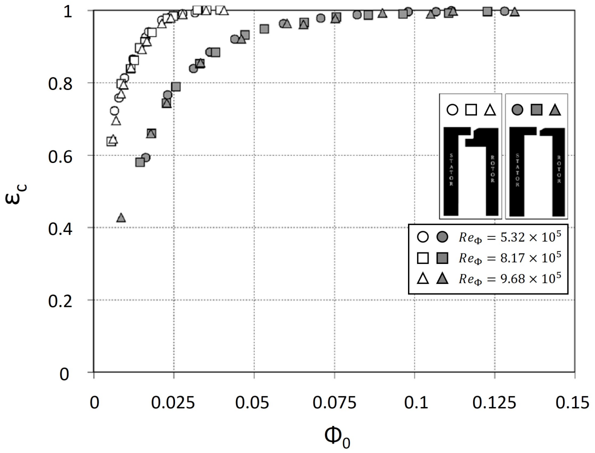

Figure 2.17: Variation of ε_c with Φ_0 for a radial rim seal (open symbols) and an axial rim seal (solid symbols). Adapted from Sangan et al. [15].

2.6 Literature review on EI ingress

The already mentioned study conducted by Abe et al. [37] in 1979 demonstrated for the first time that the ingestion of air into a rotor-stator system could be governed by the main annulus flow rather than by the disk pumping effect caused by the rotation of the rotor. In contrast to the majority of the studies described earlier, the facility designed for this study involved the use of a main flow in the annulus. Despite the absence of rotor blades, the flow was turned by approximately 50 deg through the use of 27 stationary nozzle guide vanes positioned upstream of the clearance to create the circumferential pressure asymmetries necessary to establish the EI regime. The test rig allowed the authors to perform a wide range of different measurements including pressure, velocity, propane concentration and oil paint flow visualization on different rim seal geometries designed to closely resemble those found in actual gas turbines. By conducting tests with different amounts of sealing flow injected into the cavity, the authors demonstrated that the ingestion was primarily controlled by the ratio of sealing flow to annulus flow, as well as by the shape and clearance of the rim seal. Furthermore, it was shown that the presence of non-axisymmetric flow in the annulus due to the passage of the flow over the nozzles influenced the pressure distribution within the cavity. This raised questions about the Bayley and Owen [28] correlation reported in Eq. 2.7, as the obtained results indicated that this correlation would underestimate the amount of ingested flow in all those cases where non-axisymmetric conditions existed in the main flow.

The research on EI ingress was extended in 1988 by Phadke and Owen [38, 39]. As shown in Figure 2.18, the employed test rig involved the use of an external flow in the annulus. However, due to the absence of stator vanes and rotor blades, circumferential pressure asymmetries were created by blocking portions of the annulus with honeycomb pieces attached to a wire mesh. In Phadke and Owen [38], numerous tests were carried out under quasi-axisymmetric external flow conditions on the rim seals 1, 3 and 5 described in Phadke and Owen [33] and shown in Figure 2.13.

Therefore, in order to characterize the flow in the annulus, the definition of the axial Reynolds number was introduced:

$$Re_w = \frac{\rho \cdot W \cdot r_{disk}}{\mu} \tag{2.11}$$

where W represents the axial velocity in the annulus. Moreover, the flow coefficient C_f was defined as the ratio between the axial and the rotational Reynolds numbers:

$$C_f = \frac{Re_w}{Re_\phi} \tag{2.12}$$

Different values of Re_w and Re_ϕ were tested up to a maximum of 1.2×10^6 and, as already done for the RI study, three different measurement techniques were used to determine the value of $C_{w,min}$: by introducing smoke particles into the external flow and monitoring the amount of smoke ingested into the wheel space (qualitative measurement), by measuring gas concentration on the stator surface through the injection of a small

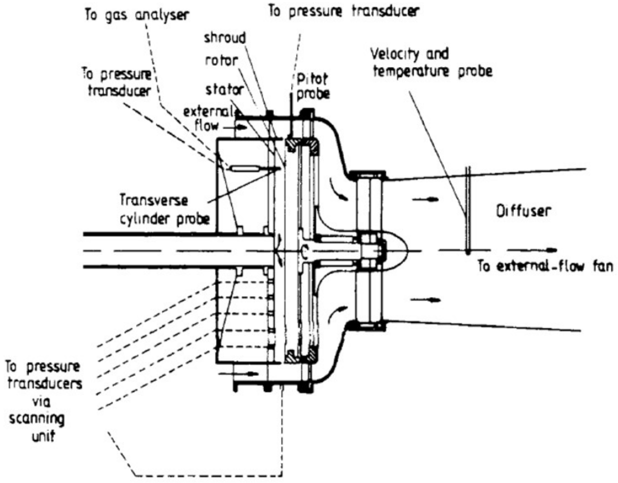

Figure 2.18: Schematic representation of the external-flow test rig employed by Phadke and Owen [38].

quantity of N_2O into the sealing flow and finally by comparing the measured pressure values between the annulus and the cavity. Despite the three methods providing qualitatively similar results, the pressure measurements tended to overestimate the resulting values of $C_{w,min}$. Figure 2.19 reports a first interesting result concerning the evaluation of the impact of the seal clearance G_c on the variation of $C_{w,min}$ with Re_w. The results were obtained for rim seal 1 in the absence of rotation ($Re_\phi = 0$) and show that $C_{w,min}$ increases linearly with Re_w. Furthermore, the results also confirm that a larger gap in the wheel-space leads to an increase in the quantity of ingested flow and consequently in $C_{w,min}$. Subsequently, additional tests were conducted by varying both the rotational speed and the external flow rate. The results shown in Figure 2.20 were obtained for rim seal 1 with $G_c = 0.01$ and illustrate the impact of Re_ϕ on the variation of $C_{w,min}$ with Re_w. The dashed line represents, for comparison, the values obtained in the case of $G_c = 0.01$ and $Re_\phi = 0$, as seen in Figure 2.19. The obtained results clearly demonstrated the existence of two flow regimes depending on the value assumed by the flow coefficient: a RI regime appears to be dominating at low values of C_f while an EI regime appears to be dominating at large values of C_f. In accordance

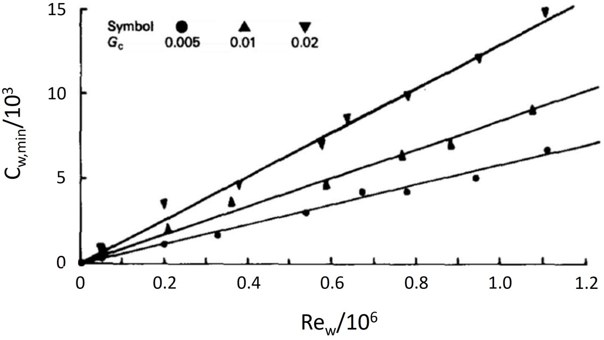

Figure 2.19: Impact of G_c on the variation of $C_{w,min}$ with Re_w for rim seal 1 with $Re_\phi = 0$. Adapted from Phadke and Owen [38].

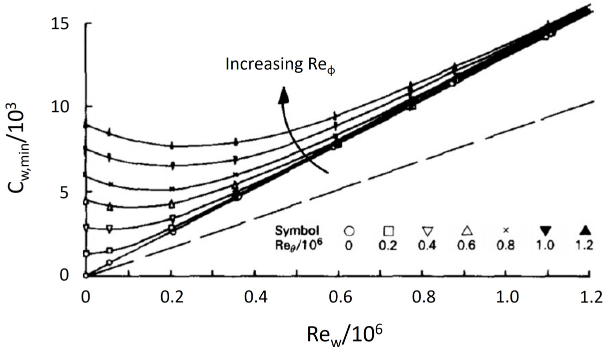

Figure 2.20: Impact of Re_ϕ on the variation of $C_{w,min}$ with Re_w for rim seal 1 with $G_c = 0.01$. Adapted from Phadke and Owen [38].

with the previously obtained results [33], Phadke and Owen observed that, in the RI regime, $C_{w,min}$ increased for increasing values of Re_ϕ. However, for larger values of C_f, the value of $C_{w,min}$ appeared to be independent from Re_ϕ but increased for increasing values of Re_w. In addition, the reported values of $C_{w,min}$ appeared to be significantly greater than those obtained for the case of $Re_\phi = 0$ (dashed line).

Then, Phadke and Owen [39] carried out additional experiments involving non-axisymmetric external flow where they incorporated the aforementioned honeycomb sections into the external annulus to create different pressure distributions in the circumferential direction without altering the flow rate. This approach allowed them to separate the effect of the pressure asymmetries from that of Re_w to determine which one of the two was dominant in the EI regime. The results shown in Figure 2.21 were obtained for rim seal 1 with $G_c = 0.01$ and $Re_\phi = 0$ and illustrate the impact of six different levels of pressure asymmetries on the variation of $C_{w,min}$ with Re_w. The circles (asymmetry number 0) represent, for comparison, the values obtained in the case of quasi-axisymmetric external flow conditions, as seen in Figure 2.19. The level of asymmetry in the external pressure distribution was quantified by using the parameter

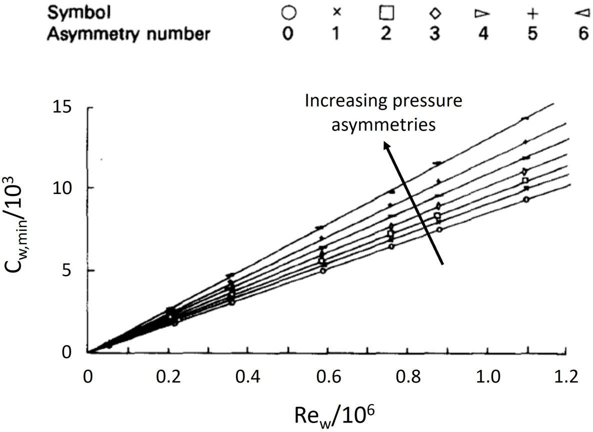

Figure 2.21: Impact of six different levels of pressure asymmetries on the variation of $C_{w,min}$ with Re_w for rim seal 1 with $G_c = 0.01$ and $Re_\phi = 0$. Adapted from Phadke and Owen [39].

$C_{p,max}$, which represents the non-dimensional maximum circumferential pressure difference in the annulus:

$$C_{p,max} = \frac{\Delta p}{\frac{1}{2} \cdot \rho \cdot W^2} \tag{2.13}$$

where Δp represents the external pressure difference and W the axial velocity of the main annulus flow. The obtained results confirmed that $C_{w,min}$ increased linearly with Re_w. Moreover, it progressively increased as the pressure distribution in the external flow became more asymmetric, hence for increasing values of $C_{p,max}$. In particular, this increase was observed to be linear with $C_{p,max}^{1/2}$. Consequently, several tests were performed on a series of axial and radial clearance rim seals and the obtained results are reported in Figure 2.22. As can be noticed, all the experimental measurements collapsed onto a single line, thus allowing Phadke and Owen to derive a correlation for EI ingress:

$$C_{w,min} = 2\pi \cdot K \cdot G_c \cdot P_{max}^{1/2} \tag{2.14}$$

where K is an empirical constant and P_{max} is a non-dimensional pressure parameter defined as:

$$P_{max} = \frac{1}{2} \cdot C_{p,max} \cdot Re_w^2 \tag{2.15}$$

For the present study, the data correlated quite well with a value of $K = 0.6$. Hence, the authors suggested that the EI ingress was predominantly influenced by the pressure asymmetry and not by the external flow rate itself and that $C_{w,min}$ could be estimated from the knowledge of P_{max}. In conclusion, it was suggested that the Bayley and Owen [28] correlation reported in Eq. 2.7 should be employed for RI ingress while the Phadke and Owen [39] correlation reported in Eq. 2.14 should be used for EI ingress. Consequently, assuming a value of $C_{w,min}$ higher than those predicted for both regimes was considered to be a conservative design approach.

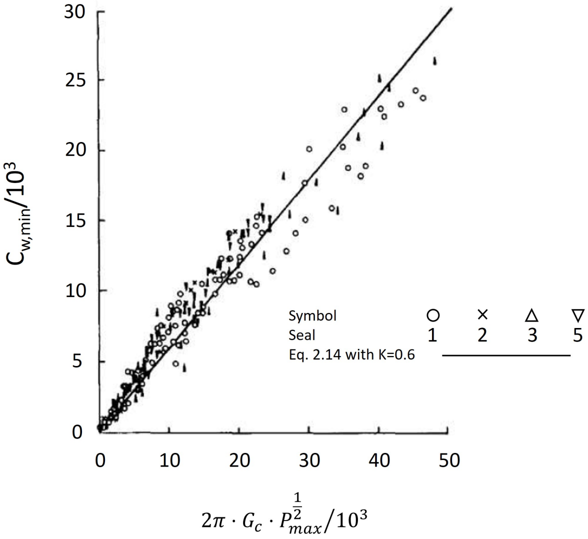

Figure 2.22: Variation of $C_{w,min}$ with $2\pi \cdot G_c \cdot P_{max}^{1/2}$. Adapted from Phadke and Owen [39].

In 1992, Hamabe and Ishida [40] continued to investigate the impact of non-axisymmetric external flow on EI ingress by performing experiments on a single-stage test rig equipped with upstream stator nozzles but without downstream rotor blades. The degree of non-axisymmetry in the external flow was measured by using 24 static pressure taps while sealing effectiveness was determined through gas concentration measurements. The authors tried to relate the effectiveness distribution obtained for different values of sealing flow rate to the external circumferential pressure distribution by employing a model they had developed in 1991 [41]. This model allowed them to approximate the external pressure profile with different functions (A: step function, B: sine-wave and C: saw-tooth) which were then integrated and the obtained results are compared to the measured data in Figure 2.23. As can be noticed, although none of the

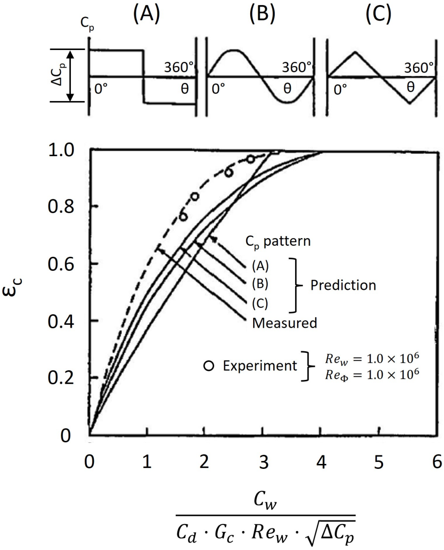

Figure 2.23: Distributions of ε_c obtained by modelling the external pressure profile with different functions (A: step function, B: sine-wave and C: saw-tooth). The dashed line corresponds to the experimentally measured distribution. Adapted from Hamabe and Ishida [40].

employed functions provided a perfect correlation with the experimental data, the best match was achieved by using the saw-tooth distribution (C). A perfect match was instead obtained by employing the experimentally measured pressure distribution (dashed line). Thus, the authors concluded that an accurate knowledge of the external circumferential pressure distribution in the flow path was essential to accurately predict the sealing effectiveness within the wheel-space, as even small differences in the employed profile led to the prediction of significantly different effectiveness values.

The already described experimental facility developed in 1992 at the University of Sussex by Dadkhah et al. [36] was capable to operate with an axisymmetric external flow but it was not equipped with vanes and blades. Thus, it was upgraded in 1994 by Chew et al. [42] who added stator guide vanes that could be used to generate pressure asymmetries in the annulus. By performing N_2O gas concentration measurements on a simple axial clearance rim seal, the authors confirmed the dependence between the static pressure distribution downstream of the vanes and the resulting values of sealing effectiveness. The obtained results were subsequently used to derive a simple orifice model similar to the one developed by Hamabe and Ishida [40]. When compared to the experimental data, the orifice model predicted a higher degree of ingestion, potentially because it did not take into account inertial effects. Furthermore, steady 3D CFD simulations were performed and a generally promising agreement with the experimental results was found. Nevertheless, an underestimation of the ingestion level was observed at high sealing flow rates which was attributed to a number of different factors such as an insufficient spatial resolution, the absence of detailed modelling of the main annulus flow and the inability to capture unsteady effects. However, it is also important to point out that CFD simulations allowed the authors to investigate the impact of ingestion on the rotor side of the cavity, an investigation which is generally very challenging to conduct experimentally due to the difficulty of performing gas concentration measurements on a surface rotating at high speed.

The test rig of the University of Sussex was then further upgraded in 1994 by Green and Turner [43] who added 32 blades to the setup previously used by Chew et al. [42]. This led to the publication of the first experimental investigation performed on a test rig for hot gas ingestion which included both vanes and blades. Their study involved the investigation of four different annulus configurations by performing N_2O gas concentration measurements on a simple axial clearance rim seal. The obtained results are reported in Figure 2.24 where the configuration with the complete stage (cross symbols) is compared with the one containing only the vanes (triangle symbols), the one with axisymmetric flow in the absence of both vanes and blades (circle symbols) and the one in complete absence of external flow (square symbols). As can be noticed, the case without external flow, corresponding to the RI regime, showed the lowest value of ingestion and thus the best effectiveness values while the configuration with only the vanes resulted in the worst performance. Unexpectedly, the addition of the blades in the complete stage configuration led to a decrease in the ingestion level rather than to an increase.

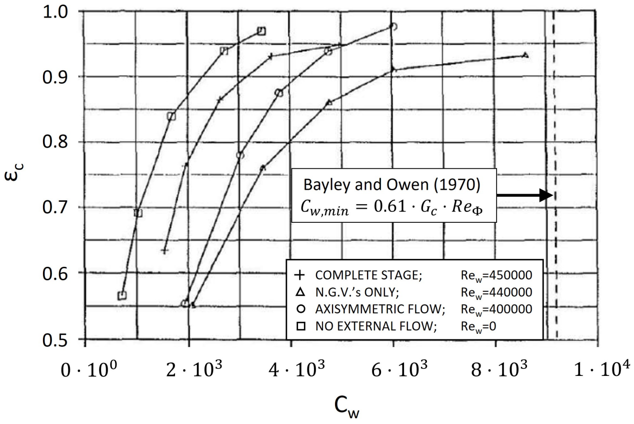

Figure 2.24: Variation of ε_c with C_w for four different annulus configurations. Adapted from Green and Turner [43].

Therefore, it was hypothesized that the rotor blades might have mitigated the pressure asymmetries generated by the vanes, leading to reduced pressure magnitudes and, consequently, to a reduced ingestion level.

In 1995, Bohn et al. [44] conducted experiments on EI ingress at the University of Aachen in a single-stage test rig equipped with 30 vanes but without blades. The test rig could reach a vane exit Mach number up to 0.70 and a rotation speed of 15000 RPM, allowing it to be operated under conditions close to those of an actual engine. By performing gas concentration measurements within the wheel-space and static pressure measurements in the annulus over two vane pitches and at three different axial positions downstream of the trailing edge of the vanes, the authors demonstrated that the level of ingestion increased as the vanes were moved closer to the entrance of the stator-rotor cavity. This phenomenon was attributed to the fact that the peak-to-trough difference of the pressure distribution downstream of the vanes decays in the axial direction. Therefore, when the vanes were moved closer to the rim seal, this resulted in higher pressure values near the cavity entrance thus leading to higher ingestion levels. Additionally, by conducting velocity measurements using the LDA technique, it was observed that, under certain conditions, the ingestion of air could occur not only on the stator side but also on the rotor side of the cavity. In parallel with the experiments, multiple numerical simulations were performed to investigate the flow structure developing inside the wheel-space and a qualitatively good agreement with the experiments was found.

In 1997, Hills et al. [45] attempted to further investigate the interaction between the mainstream flow and the sealing flow by conducting pressure measurements on a slightly modified configuration of the test rig described by Chew et al. [42] which was equipped with an axial clearance rim seal. In particular, 29 stator guide vanes were positioned 3 mm upstream of the rim seal gap to create a pressure asymmetry in the external flow and 16 aluminium pegs were placed 18.5 mm downstream of the rim seal gap in place of the rotor blades. This choice was made to minimize the impact of the rotor blades on the upstream pressure asymmetry. The experimental results were then compared with those obtained through steady 3D CFD simulations and a good agreement was found at low values of sealing flow. On the contrary, the significant discrepancy recorded at high values of sealing flow was attributed to the interaction between the mainstream flow and the sealing flow itself. The authors concluded that a comprehensive CFD calculation incorporating both annulus and cavity flows might be necessary to fully capture this phenomenon.

The test rig of the University of Aachen was then upgraded in 1999 by Bohn et al. [46] who equipped it with 62 rotor blades and a dynamometer to dissipate the generated power. The authors performed pressure measurements and CO_2 gas concentration measurements on the two different rim seal geometries shown in Figure 2.25 to assess the effects of both Re_w and Re_ϕ on the sealing effectiveness. The results indicated that an increase in Re_w corresponded to an increase in the pressure asymmetry within the annulus and thus to a decrease in the sealing performance for both the investigated geometries. The effect of Re_ϕ appeared instead to be dependent on the type of geometry tested. Furthermore, the radial

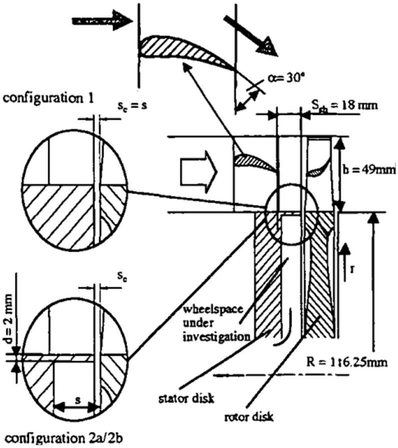

Figure 2.25: Representation of the test rig used by Bohn et al. [46].

profile of effectiveness within the cavity was investigated and it was found to be almost invariant with radius. This led the authors to conclude that the complete mixing between the ingress flow and the sealing flow occurred near the rim seal clearance. In addition, 3D CFD simulations were conducted on the configuration without blades leading to the identification of recirculation zones with variable diameter near the rotor disk.

In 2000, Bohn et al. [47] further examined the effect of rotor blades on the sealing effectiveness by performing CO_2 gas concentration measurements on the two rim seal geometries previously shown in Figure 2.25 and then comparing the results with previous experiments conducted without blades [44]. As shown in Figure 2.26, the obtained results were contradictory since, for configuration 1, the circumferential pressure asymmetry measured 1.5 mm downstream of the trailing edge of the vanes increased with the presence of rotor blades, resulting in a subsequent deterioration of the sealing performance (see Figure 2.26a). On the contrary, the addition of blades in configuration 2 led to an improvement of the sealing performance (see Figure 2.26b). In addition, 3D unsteady

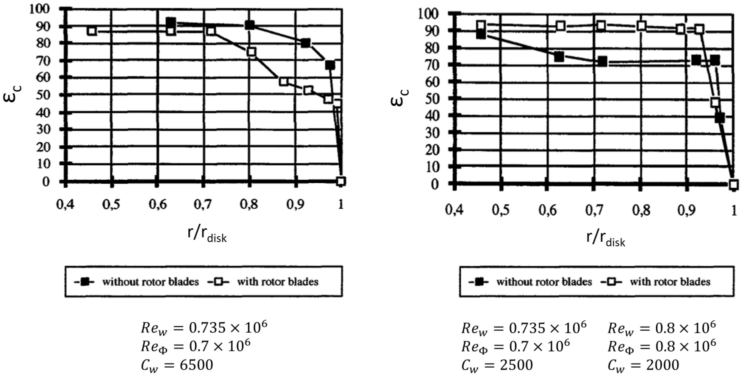

(a) Results for configuration 1 *(b) Results for configuration 2*

Figure 2.26: Radial profiles of effectiveness obtained with and without blades for the (a) Configuration 1 and (b) Configuration 2 shown in Figure 2.25. Adapted from Bohn et al. [47]

CFD simulations were conducted for configuration 2 and the results were compared with those obtained with steady calculations performed on the same configuration but without blades [46]. The numerical analysis predicted the existence of an ingestion region rotating at approximately half the rotor speed. Moreover, in accordance with the experimental data, the presence of rotor blades was observed to have a positive impact on the sealing performance.

In 2001, Khilnani and Bhavnani [48] conducted an experimental study to investigate the ingestion of air inside stator-rotor cavities in the presence of external annulus flow. In particular, they compared the performance of two different geometries: a simple configuration equipped with an axial rim seal (shown in Figure 2.27a) and a realistic engine configuration with two teeth (shown in Figure 2.27b). The tests were conducted for values of Re_ϕ up to 1.5×10^6 and values of Re_w up to 6×10^5 and the amount of sealing flow required to prevent the ingestion of external flow into the

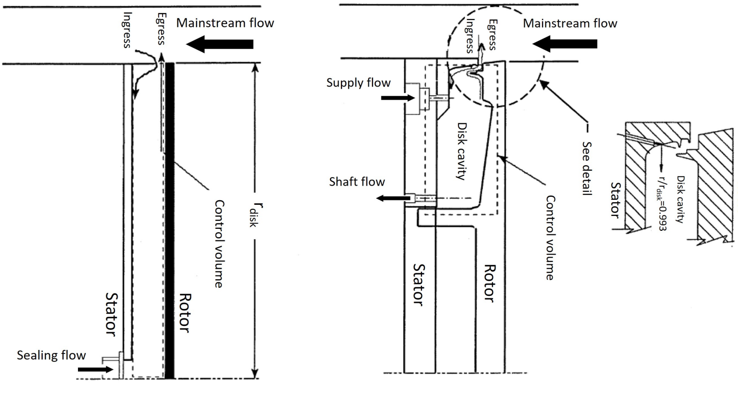

(a) Simple configuration (b) Realistic engine configuration

Figure 2.27: Schematic representation of the (a) Simple configuration and (b) Realistic engine configuration. Adapted from Khilnani and Bhavnani [48]

wheel-space was determined by using both static pressure measurements and CO_2 gas concentration measurements. The obtained results are presented in Figure 2.28 in terms of variation of $C_{w,min}$ with Re_w for different values of Re_ϕ and in Figure 2.29 in terms of variation of $C_{w,min}$ with the parameter $2\pi \cdot G_c \cdot P_{max}^{1/2}$. Despite the results of Khilnani and Bhavnani being in good agreement with those of Phadke and Owen [39], some discrepancies can be noticed. In particular, it can be observed that the results do not become completely independent of Re_ϕ at the highest tested values of Re_w. This behaviour can be attributed to the fact that the tests were conducted at relatively low values of Re_w which would correspond to the establishment of a CI regime rather than a completely EI regime. Finally, the authors showed that the sealing performance of the realistic engine configuration was significantly superior than that of the simplified geometry in terms of both required sealing flow rate to prevent ingestion and sealing effectiveness.

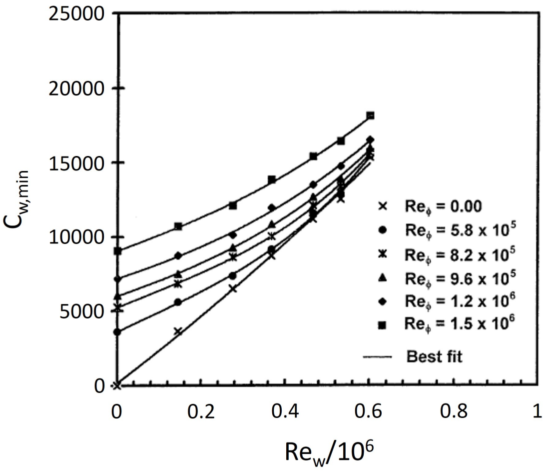

Figure 2.28: Impact of Re_ϕ on the variation of $C_{w,min}$ with Re_w. Adapted from Khilnani and Bhavnani [48]

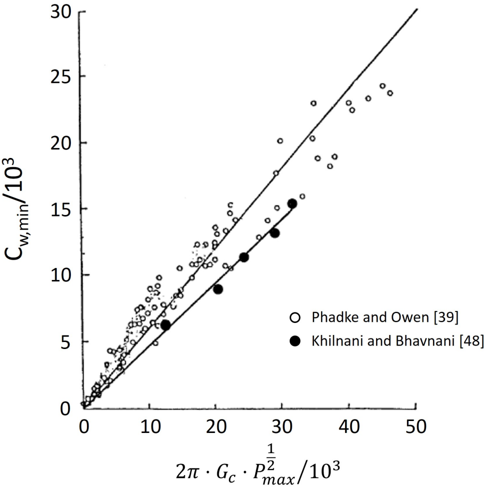

Figure 2.29: Variation of $C_{w,min}$ with $2\pi \cdot G_c \cdot P_{max}^{1/2}$. Adapted from Khilnani and Bhavnani [48]

In 2002, Hills et al. [49] conducted a series of CFD simulations on the ingestion of air in the EI regime, extending their work from 1997 [45]. In particular, the results obtained through unsteady 3D simulations showed significantly better agreement with experimental data compared to steady simulations. Moreover, the simulations revealed that the circumferential pressure asymmetries caused by the presence of pegs, used in the test rig to simulate the effect of rotor blades, had a considerable impact on the ingestion despite being smaller in magnitude than the pressure asymmetries generated by the vanes. This led the authors to suggest that the presence of rotor blades generally tends to increase the ingestion, indicating that the measurements shown in Figure 2.24 performed by Green and Turner [43] on the configuration containing only the vanes might be affected by an error. In conclusion, the authors suggested that also factors such as the number of vanes and blades, as well as the swirl velocity in the annulus, may significantly influence the amount of flow ingested within the wheel-space.

In 2003, Bohn and Wolff [50] used a test rig equipped with a single row of vanes and a single row of rotor blades to investigate the performance of four different rim seal configurations through pressure measurements and CO_2 gas concentration measurements. The value of $C_{w,min}$ measured for each configuration was associated with the respective value of seal clearance ratio G_c, axial Reynolds number Re_w and maximum external pressure asymmetry $C_{p,max}$, thus obtaining effectiveness curves which were then compared to the results obtained by Phadke and Owen [39] reported in Figure 2.22. As shown in Figure 2.30, although all the investigated geometries exhibited a linear relationship between $C_{w,min}$ and $C_{p,max}^{1/2}$, it is also evident that the empirical constant K varies from one configuration to another and it must be experimentally determined for each case through a least squares error minimization procedure. Therefore, the single value of $K = 0.6$ suggested by Phadke and Owen [39] could be

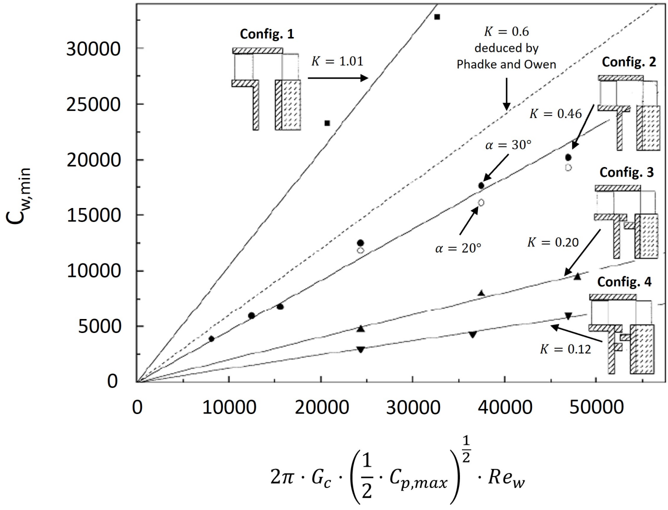

Figure 2.30: Comparison of different values of the empirical constant K experimentally determined for four different rim seal configurations. Adapted from Bohn and Wolff [50]

considered excessively conservative. Moreover, the authors demonstrated that varying the vane exit angle has only a minor impact on the ingestion level (filled versus empty circles in Figure 2.30).

In 2003, Gentilhomme et al. [51] presented the experimental results obtained on a new single stage test rig developed at the University of Sussex and equipped with 26 vanes and 59 rotor blades. Furthermore, since the facility allowed testing a wide range of vane exit Mach numbers, two different operating conditions were compared: OC1 (NGV exit $Ma = 0.963$) and OC2 (NGV exit $Ma = 0.390$). A variable sealing flow rate could be supplied to the stator-rotor cavity which was equipped with a simple axial clearance rim seal and the level of ingestion could then be estimated by performing pressure measurements and N_2O or CO_2 gas concentration measurements. As shown in Figure 2.31, the effectiveness values obtained for the two operating conditions were appropriately correlated through the use of the velocity ratio between the bulk-mean velocity through the rim-seal clearance U and the axial velocity in the annulus W. In conclusion, the authors suggested that the obtained results should not be

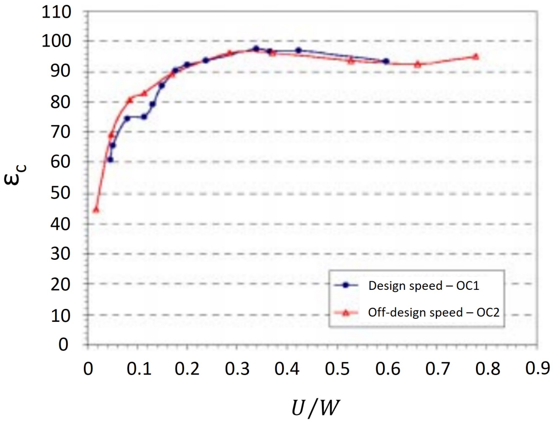

Figure 2.31: Variation of ε_c with U/W for two operating conditions (OC1 and OC2). Adapted from Gentilhomme et al. [51]

generalized to other rim seal configurations without a thorough evaluation as there are several factors, such as the number of vanes and blades, the distance between them and the entrance of the rim seal clearance and the specific geometry of the rim seal, that will have a fundamental impact on the resulting effectiveness values. Moreover, despite the relatively low impact of the Mach number, the authors pointed out that the rate at which the circumferential pressure asymmetries decay along the axial direction varies with the Mach number. Therefore, the impact of this factor could be fundamental in certain circumstances.

The test rig of the University of Aachen was then further upgraded in 2003 by Bohn et al. [52] who converted it into a 1.5-stage turbine equipped with 16 vanes on each side of 32 rotor blades. The authors performed 2D unsteady LDA measurements with high spatial and time resolution, capturing data at 17 circumferential positions. For each position, 5 different axial positions and 2 dimensionless radii, $r/r_{disk} = 0.985$ and $r/r_{disk} = 0.952$, were investigated. By conducting measurements at different sealing flow rates, the authors demonstrated that both the vanes and the rotor blades have a significant impact on the ingestion level and that, even at high values of sealing flow, the ingestion occurs in correspondence of the high-pressure regions located in front of the blades. Moreover, these regions appeared to intensify in correspondence of the interaction between the blades and the stator wakes.

In 2004, Jakoby et al. [53] conducted a study where different numerical approaches were used to investigate the performance of an axial rim seal configuration. The aim of the study was to perform a comprehensive simulation of the time-dependent flow field within the 1.5 stage test rig developed at the University of Aachen, including both the main annulus and the two stator-rotor cavities. To validate their numerical simulations, the authors compared the computed cavity pressure and the sealing effectiveness with the experimental data. However, despite the better agreement achieved with the 360 deg model with respect to the sector models, the CFD significantly underestimated the ingestion level. The study particularly focused on the detailed analysis of a large-scale rotating structure, initially identified in the front cavity of the test rig through unsteady pressure measurements. Interestingly, when the sealing flow rate was sufficiently low, the researchers observed the presence of low-pressure regions rotating at approximately 80% of the rotor speed which had a considerable impact on the ingestion level.

In 2004, Cao et al. [54] conducted a detailed study on the interaction between the main gas path and the sealing flow by using a combination of CFD and experimental measurements. Their research focused on a two-stage axial turbine where they measured the pressure in the cavity formed between the stage 2 rotor disk and the upstream diaphragm. The obtained results revealed that the ingestion of highly swirled annulus flow led to the formation of a vortex with increased strength within the cavity and this phenomenon was especially evident for larger values of axial clearance. The authors performed various steady and unsteady CFD simulations and a good agreement was found with the experimental data. In addition, the unsteady models revealed previously unknown unsteady flow features which were then confirmed experimentally through the use of fast response pressure transducers.

In 2006, Bohn et al. [20] compared the sealing performance of an axial rim seal with that of a radial rim seal in preventing the ingestion of air in the front cavity of the 1.5-stage Aachen test rig. The authors conducted static pressure measurements on the stator disk and on the rim seal lip as well as CO_2 concentration measurements within the cavity to determine the variation of effectiveness with different parameters such as the non-dimensional sealing flow rate, the axial Reynolds number and the rotational speed. The obtained results confirmed the superior sealing performance of the radial rim seal with respect to the axial one as the former required a smaller amount of purge flow to completely seal the cavity.

In 2006, Johnson et al. [55] developed a new method to predict the quantity of ingested air through a rim seal. Unlike previous methods that relied on the use of the averaged pressure distribution downstream of the vanes, this novel approach was based on the use of the 2D time-dependent pressure distribution on the turbine hub along with a basic Orifice Model. This approach allowed accounting for the influence of both the vane wakes and the bow waves generated by the blades on the pressure difference between the hub and the cavity at a specific circumferential position. The results obtained from the Orifice Model could then be used to determine the value of the discharge coefficient C_d that best matches the sealing effectiveness near the rim seal with the quantity of ingested air. The model was then validated through a comparison with the results obtained from both numerical simulations of a sector of the Aachen test rig (1 vane/2 blades) and with the experimental data obtained by Bohn et al. [52]. As shown in Figure 2.32, assuming a value of the discharge coefficient equal to $C_d = 0.4$ allowed the authors to obtain a good agreement with the experimental data. The authors also investigated the impact of changing the distance between the TE of the vanes and the LE of the blades by analysing a close-spaced and a far-spaced configuration. Therefore, it was shown that the time-dependent pressure field could be the dominant cause of ingestion for close-spaced turbines while it could be a less significant ingestion mechanism for more widely spaced configurations.

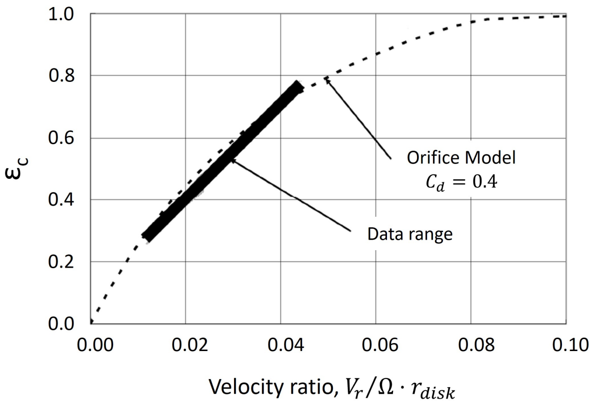

Figure 2.32: Comparison between the experimental data and the Orifice Model with $C_d = 0.4$. Adapted from Johnson et al. [55]

In 2007, Roy et al. [56] conducted a study at the Arizona State University where they performed experiments in a single-stage axial turbine test rig including vanes, blades and an axially overlapping radial clearance rim seal. In particular, they performed sealing effectiveness measurements and Particle Image Velocimetry (PIV) experiments that were used to determine the time-resolved velocity maps of the flow field developing in the wheel-space under different operating conditions in terms of external flow rate, rotor speed and sealing flow rate. The obtained results revealed the presence of regions characterised by high tangential velocity fluid, supposedly representing the ingested air, alternated to regions characterised by lower tangential velocity fluid, supposedly representing the air already present in the cavity. This conclusion was also supported by the results obtained from an unsteady 3D CFD simulation which indicated the presence of large-scale unsteady structures in the cavity leading to substantial velocity fluctuations.

In 2008, Johnson et al. [57] presented an updated version of the Orifice Model developed in their previous work [55]. Instead of using a single lumped discharge coefficient for both the ingress and egress flows, they employed two separate coefficients: $C_{d,i}$ for the ingress and $C_{d,e}$ for the egress. Additionally, a term was added to account for the effect of swirl in the mixing region of the rim seal. This model was validated by using the experimental results obtained by the Arizona State University on a single overlapped rim seal. As shown in Figure 2.33, a good agreement with the experimental data was achieved by using the following discharge coefficients: $C_{d,e} = 0.27$ and $C_{d,i} = 0.20$. Therefore, the authors concluded that the updated Orifice Model was able to characterize the performance of rim seals much more accurately than the previous version.

In 2011, Zhou et al. [58] conducted further experiments at the Arizona State University by testing three different rim seal configurations, including a double seal, to investigate the influence of the seal geometry on the ingestion of external flow. Thus, CO_2 gas concentration measurements and PIV experiments were respectively employed to determine the sealing effectiveness and the instantaneous velocity field inside the cavity. At low

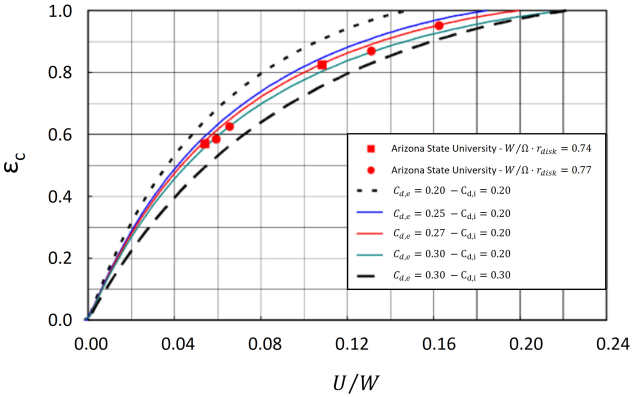

Figure 2.33: Comparison between different Orifice Model predictions and experimental data. Adapted from Johnson et al. [57]

values of sealing flow rate, multiple regions of ingress and egress were identified by examining the instantaneous radial velocity distribution near the rim seal. Moreover, an unsteady 3D CFD simulation of a sector model was performed but it was found to underestimate the quantity of ingested air. This discrepancy was attributed to the inability of the sector model to capture the presence of circumferentially rotating low-pressure regions, a phenomenon instead predicted by the complete 360 deg simulation.

In 2011, Balasubramanian et al. [59] conducted different tests on a new 1.5-stage axial-flow test rig of the Arizona State University in order to investigate the ingress of external air into the aft disk cavity. The investigated configuration included rotor and stator rim seals with radial clearance and axial overlap as well as an inner labyrinth seal. The experiments were conducted for two external flow rates, two rotor speeds and three sealing flow rates by using gas concentration and PIV to respectively measure the ingestion of external flow and the fluid velocity field in the wheel-space. The obtained results showed that, at the highest tested value of sealing flow rate, the inner wheel-space was completely sealed while ingestion of air still occurred in the outer wheel-space.

In 2012, a new 2-stage stator well test rig was developed at the University of Sussex by Coren et al. [60] and later used by Eastwood et al. [61] to quantify the re-ingestion of sealing flow within the wheel-space of an engine representative geometry. In particular, the results obtained from gas concentration measurements showed that the quantity of egress flow that was re-ingested into the downstream cavity was approximately equal to 7%. However, this percentage decreased as more sealing flow was injected into the wheel-space.

The extensive theoretical, experimental and numerical investigation on hot gas ingestion of the research group of the University of Bath was extended from the study of the RI case to the study of the EI case. In 2012, Sangan et al. [8] utilized an axial single-stage test rig equipped with 32 stator blades and 41 symmetric rotor blades to perform CO_2 gas concentration measurements in order to determine the sealing effectiveness on two rim seal configurations: an axial rim seal (shown in Figure 2.34a) and a radial rim seal (shown in Figure 2.34b). First, the circumferential variation of static pressure in the annulus was determined by using two sets

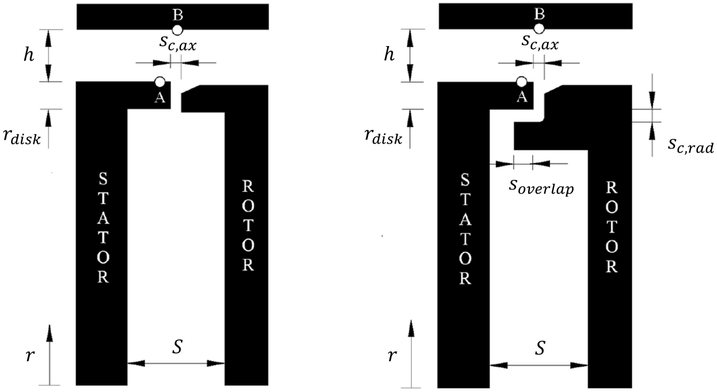

(a) Axial rim seal (b) Radial rim seal

Figure 2.34: Schematic representation of the (a) Axial rim seal and (b) Radial rim seal. Adapted from Sangan et al. [8]

of 15 pressure taps each. As shown in Figure 2.34, one was positioned on the stator platform 2.5 mm downstream of the TE of the vanes (location A) and the other on the outer casing in correspondence of the center line of the rim seal clearance (location B). Thus, the circumferential pressure distributions at locations A and B were obtained at design conditions that, for the present test rig, corresponded to a flow coefficient of $C_f = 0.538$. Moreover, the tests were conducted in complete absence of sealing flow ($\Phi_0 = 0$). The obtained results are presented in Figure 2.35 in terms of pressure coefficient C_p, which is defined as follows:

$$C_p = \frac{p_1 - p_{1,avg}}{\frac{1}{2} \cdot \rho \cdot \Omega^2 \cdot r_{disk}^2} \tag{2.16}$$

where p_1 is the pressure in the annulus measured with each tap and $p_{1,avg}$ is the average pressure over one vane pitch. As can be noticed from the results of the tests conducted at a constant value of C_f ($= Re_w/Re_\phi$), the measurements taken at position A appear to be independent of Re_ϕ. However, a significant difference can be noticed between position A and

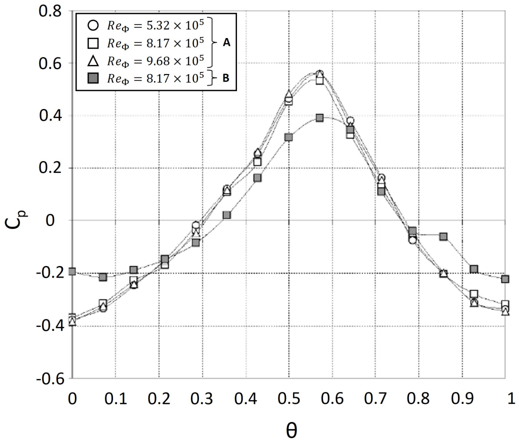

Figure 2.35: Circumferential distributions of C_p over the non-dimensional vane pitch at locations A and B. Adapted from Sangan et al. [8]

position B. In particular, the value of the non-dimensional peak-to-trough pressure difference is higher at position A. This parameter, commonly considered to be the driver for ingress in the EI regime, is denoted as ΔC_p and it is defined as follows:

$$\Delta C_p = C_{p,max} - C_{p,min} = \frac{p_{1,max} - p_{1,min}}{\frac{1}{2} \cdot \rho \cdot \Omega^2 \cdot r_{disk}^2} \tag{2.17}$$

where max and min refer to the maximum and minimum values measured over the vane pitch. Despite the pressure in the annulus increases in the radial direction due to the effect of the swirl, the decay in the axial direction appears to be the dominant effect thus causing the reduced distribution obtained at location B. This led the authors to observe that the value of ΔC_p depends on the location at which the pressure is measured, thus questioning the use of the empirical constant K proposed by Phadke and Owen [39] and Bohn and Wolff [50] to rank the performance of different rim seals. Another important observation was made by analysing the circumferential distributions of C_p obtained at design conditions ($C_f = 0.538$), constant rotational Reynolds number ($Re_\phi = 8.17 \times 10^5$) and fixed location (position A) but for three different values of Φ_0/Φ_{min}, where Φ_{min} represents the minimum value of Φ_0 required to completely prevent ingress. As can be noticed from the results reported in Figure 2.36, increasing Φ_0 leads to a slight decrease in ΔC_p. This behaviour can be attributed to the interaction of the egress flow with the external flow, a phenomenon defined as the "spoiling effect". Finally, the last observation concerning the pressure measurements regards the linear trend of $\Delta C_p^{\frac{1}{2}}$ with C_f reported in Figure 2.37. As expected, the linear trend is not affected by the value of Re_ϕ employed to perform the tests. Indeed, for a given vane and blade geometry, the value of C_f uniquely determines the velocity triangle of the stage and consequently the value of ΔC_p. Moreover, the value of $\beta - \beta_{design}$, which represents the variation of the blade inlet angle with respect to the design value, is reported on the upper x-axis. Subsequently, the variation of the sealing effectiveness ε_c with the non-dimensional sealing parameter Φ_0 was obtained by performing

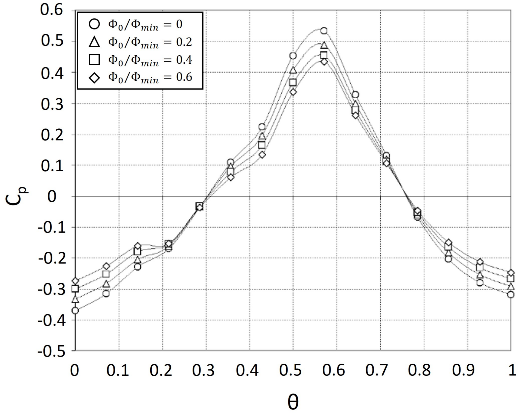

Figure 2.36: Effect of Φ_0/Φ_{min} on the circumferential distribution of C_p over the non-dimensional vane pitch. Tests conducted at $C_f = 0.538$, $Re_\phi = 8.17 \times 10^5$ and location A. Adapted from Sangan et al. [8]

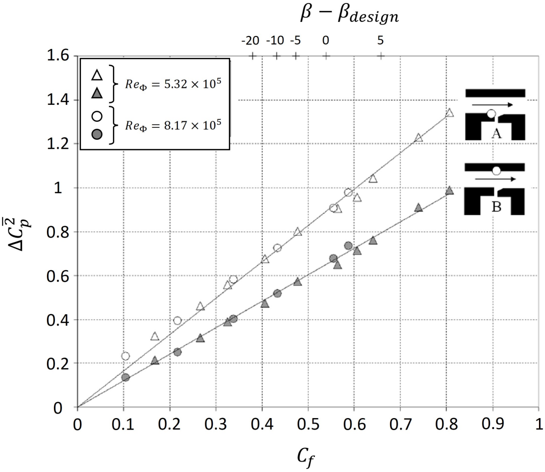

Figure 2.37: Variation of $\Delta C_p^{\frac{1}{2}}$ with C_f for different values of Re_ϕ at locations A and B. Adapted from Sangan et al. [8]

CO_2 gas concentration measurements on the stator surface at a radial position of $r/r_{disk} = 0.958$. The results obtained in this study for the EI regime were then compared with those obtained in the already mentioned parallel study [15] concerning the RI regime. This comparison is shown in Figure 2.38 for both a radial rim seal (open symbols) and an axial rim seal (solid symbols) and for different values of Re_{ϕ}. As can be noticed, the radial rim seal requires approximately 26% of the sealing flow required by the axial rim seal to fully seal the cavity and thus prevent EI ingress. As previously mentioned, this value turned out to be 38% for the RI case. Hence, in both cases the radial rim seal significantly outperformed the axial rim seal. Moreover, the non-dimensional sealing parameter Φ_0 required to prevent RI ingress appeared to be considerably lower than that required for EI ingress. In particular, for the axial rim seal, the ratio between the sealing flow rate necessary to prevent ingress in the RI regime and that required in the EI regime was approximately 26%. For the radial rim seal, this ratio was instead approximately 35%.

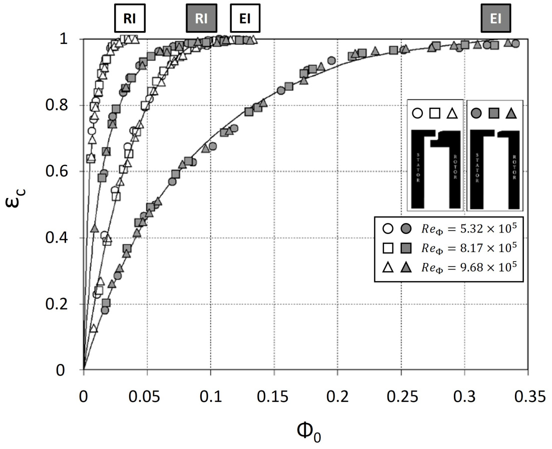

Figure 2.38: *Variation of* ε_c *with* Φ_0 *for a radial rim seal (open symbols) and an axial rim seal (solid symbols) and for RI and EI regimes. Adapted from Sangan et al. [15].*

In 2013, Sangan et al. [19] compared the performance of four single rim seals (S1: axial rim seal, S2a: radial rim seal, S2b: radial rim seal with reduced overlap and S2c: single rim seal with reduced overlap and reduced radial clearance) with that of two double rim seals (D1: axial rim seal derived from S1 and D2: radial rim seal derived from S2c). The six investigated geometries are shown in Figure 2.39 and the obtained results are presented in Figure 2.40 where the performance of the different configurations have been ranked in order of magnitude of Φ_{min} values. For the double rim seals, the Φ_{min} values measured in both the inner clearance (gray bar) and the outer clearance (green bar) have been

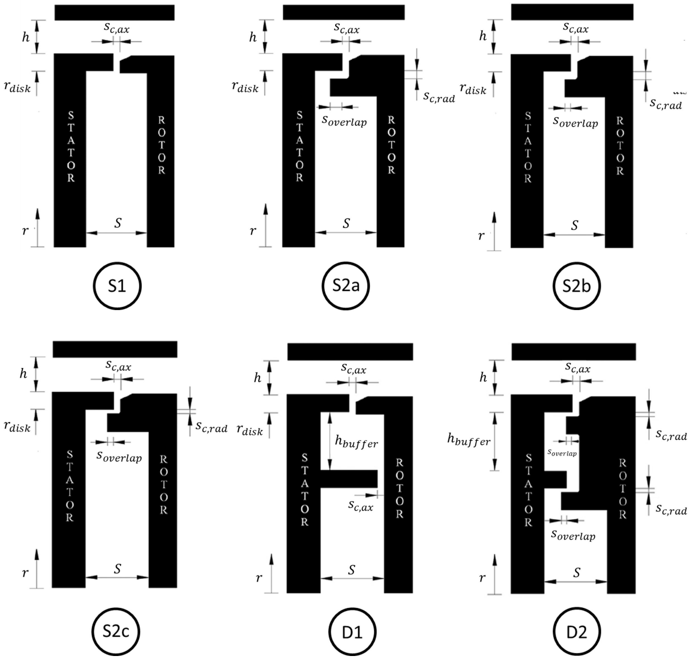

Figure 2.39: Schematic representation of four single rim seals (S1, S2a, S2b and S2c) and two double rim seals (D1 and D2). Adapted from Sangan et al. [19].

reported. Additionally, the red lines represent the Φ_{min} values obtained for the RI case where significantly greater values of sealing effectiveness were observed for all the rim seals. As can be seen, D2 exhibits the best performance while S1 the worst. Furthermore, when comparing the Φ_{min} value measured in rim seal D2 with that obtained from the single rim seal S2c, from which D2 was derived, it can be noticed that the double geometry provided a reduction in Φ_{min} by approximately 50%. The comparison between the single radial rim seals with different values of radial clearance and axial overlap (S2a, S2b and S2c) is also interesting. As expected, since rim seal S2b was characterized by the smallest axial overlap and the largest radial clearance, it exhibits the worst sealing performance among the three. When compared to rim seal S2a, which features an increased axial overlap, some improvement can be noticed. However, a more significant enhancement was achieved by reducing the radial clearance in rim seal S2c. Nevertheless, the magnitude of these variations is almost negligible when compared to the performance increase resulting from the transition from a single to a double rim seal.

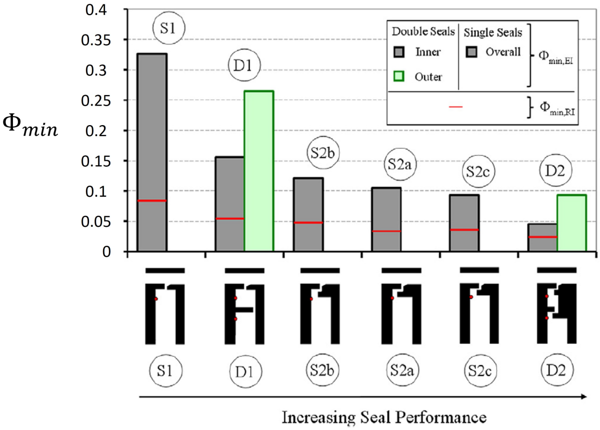

Figure 2.40: Ranking of the performance of the six investigated rim seals in order of magnitude of Φ_{min}. Adapted from Sangan et al. [19].

In 2013, Pountney et al. [62] conducted further experiments on the test rig of the University of Bath by performing transient measurements through the use of Thermochromic Liquid Crystal (TLC) in order to determine the adiabatic effectiveness on the rotor side of the cavity. This led to the publication of the first study addressing the effect of ingestion on the adiabatic temperature of the rotating disk. Hence, Figure 2.41 compares the adiabatic effectiveness obtained on the rotor side with the sealing effectiveness obtained on the stator side through simultaneous measurements of CO_2 gas concentration. All the measurements have been repeated at different values of Re_ϕ but the results consistently appear to be independent of the rotational speed. As can be noticed, the effectiveness values measured on the rotor were always significantly higher than those measured on the stator. This phenomenon was attributed to the presence of a thermal buffer layer generated by the boundary layer on the rotor which protects the rotating disk from the effects of ingestion. In this

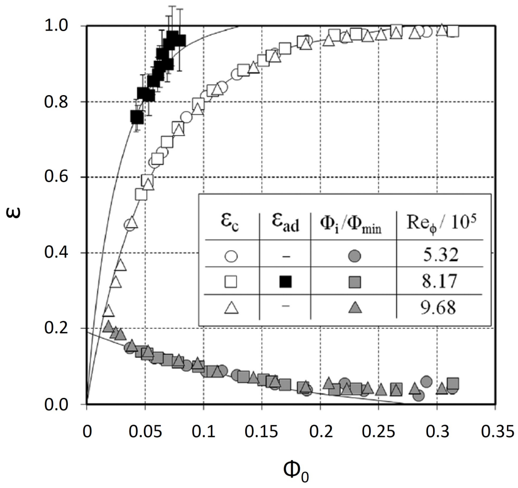

Figure 2.41: Variation of concentration effectiveness ε_c (stator side) and adiabatic effectiveness ε_{ad} (rotor side) with Φ_0 for different values of Re_ϕ. Adapted from Pountney et al. [62].

regard, a thermal buffer ratio was defined as the ratio between the sealing flow rate when ingestion first occurs and that at the moment it is first experienced by the rotor. Such parameter was found to depend on the turbulent flow parameter λ_{turb}. A simple buffer-ratio model was also used to correlate the adiabatic effectiveness data obtained for the rotor but, since the range of tested values was limited, no definitive conclusion could be drawn at low and high sealing flow rates.

In 2015, Cho et al. [12] further investigated the effectiveness on the rotor side of the cavity by conducting additional experiments on the test rig of the University of Bath. In particular, they developed infra-red sensors that were used to accurately measure the temperature history of the rotor surface during transient experiments. Then, by combining these measurements with a numerical solution of the Fourier's equation, the authors were able to determine the adiabatic wall temperature and thus the adiabatic effectiveness for different values of sealing flow rate injected into the cavity. This procedure is similar to the one previously developed by Pountney et al. [62]. As shown in Figure 2.42, the investigation of the performance of four rim seals (S1: single axial rim seal, S2: single radial rim seal, D1: double axial rim seal and D2: double radial rim seal) allowed the authors to demonstrate that the effectiveness on the rotor side is always significantly higher than that on the stator side. This phenomenon was again explained by taking into account the presence of a thermal buffering effect, in which the sealing air attaches itself to the rotating surface thus reducing the entrainment of ingested air into the rotor boundary layer (hence increasing the effectiveness). An interesting consequence of this observation is that a substantial amount of ingested air can enter into the wheel-space before its effects are sensed by the rotor.

The test rig of the University of Bath was then upgraded in 2014-2016 by Scobie [63] and Patinios et al. [64] who converted it into a 1.5-stage turbine equipped with 32 vanes on each side of 48 turned rotor blades. The authors conducted CO_2 gas concentration measurements in both the upstream and downstream wheel-spaces, demonstrating once again the exceptional sealing performance of double radial rim seals.

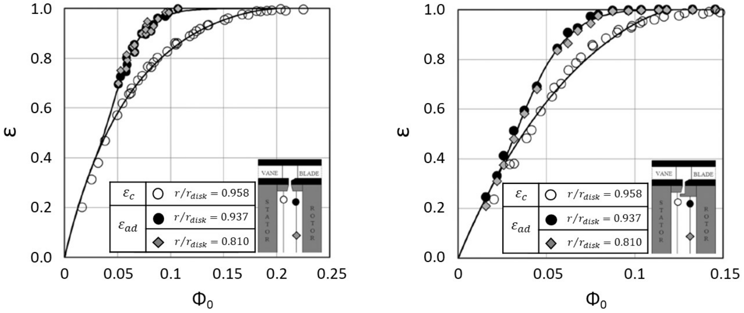

(a) S1 - Single axial rim seal *(b) S2 - Single radial rim seal*

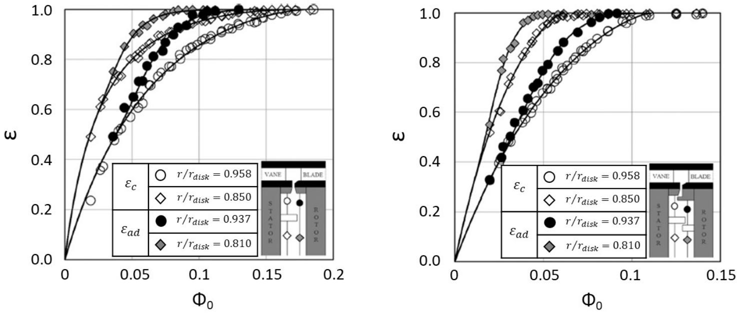

(c) D1 - Double axial rim seal *(d) D2 - Double radial rim seal*

Figure 2.42: Variation of concentration effectiveness ε_c (stator side) and adiabatic effectiveness ε_{ad} (rotor side) with Φ_0 for (a) S1 - Single axial rim seal, (b) S2 - Single radial rim seal, (c) D1 - Double axial rim seal and (d) D2 - Double radial rim seal. Adapted from Cho et al. [12].

This configuration effectively confined the majority of the ingested flow within the outer part of the rim seal, thus leaving the inner part greatly protected from the ingested gases. The obtained results also revealed that the flow that exited from the upstream cavity created a fluid barrier in correspondence of the downstream cavity that the external annulus flow had to cross before being ingested. Additionally, the resulting mixing between the ingress and egress flows at the entrance of the downstream cavity led to a reduction in the circumferential pressure distribution of the external flow. The combination of these two effects resulted in an increase in the sealing effectiveness measured in the downstream cavity compared to the values measured in the upstream one, regardless of the value of sealing flow rate.

In 2021, Graikos et al. [65] conducted an additional experimental study on hot gas ingestion by using the new 1.5-stage test rig developed at the University of Bath. The study focused on the upstream and downstream cavities equipped with double radial rim seals and investigated the alternative use of two rotor disks, one with blades and one without, to evaluate their influence on the ingestion in the upstream cavity. Similarly, two downstream stator disks were used, one with vanes and one without, to assess their impact on the ingestion in the downstream cavity. The tests were conducted under various operating conditions by varying the annulus mass flow rate and the injected sealing flow rate. Pressure and CO_2 gas concentration measurements were employed to determine the sealing effectiveness in both wheel-spaces. The results presented in Figure 2.43 were obtained for the upstream cavity and illustrate the variation of sealing effectiveness ε_c measured at $r/r_{disk} = 0.958$ with the flow coefficient C_f for three different values of injected sealing flow rate Φ_0. Each of these data series was obtained by keeping the sealing flow rate and the rotational speed constant while the flow coefficient was varied by changing the annulus mass flow rate. Furthermore, these experiments were repeated both in presence (solid symbols) and in absence (open symbols) of the rotor blades. As can be noticed, in the absence of blades, ε_c monotonically decreases with the increase in C_f while it increases for higher values of Φ_0. The introduction of the rotor blades generally leads to an increase in the ingestion level. However, despite the similar trend between the curves obtained with and without blades, a non-monotonic behaviour can be observed in a limited range of C_f for the bladed configuration. This phenomenon corresponded to a sweep of the relative flow angle equivalent to the LE of the blades and the departure from the monotonic trend was

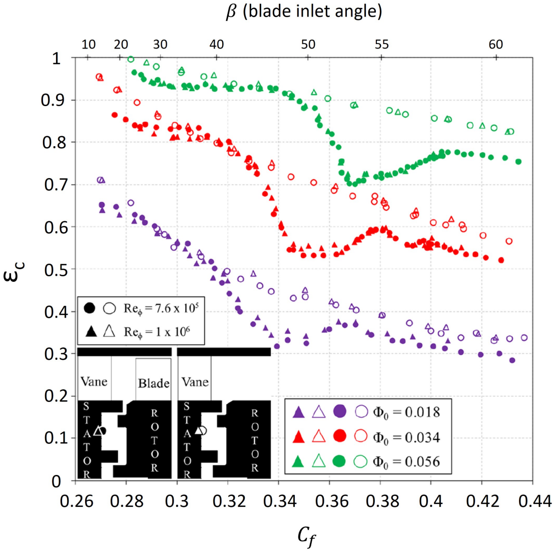

Figure 2.43: Variation of sealing effectiveness ε_c measured at $r/r_{disk} = 0.958$ with the flow coefficient C_f for three different values of injected sealing flow rate Φ_0. Comparison between a bladed (solid symbols) and a bladeless (open symbols) rotor disk. Adapted from Graikos et al. [65].

linked to an increase in the swirl ratio within the wheel-space. Moreover, this region appeared to shift to higher values of C_f for increasing values of Φ_0. This led the authors to conclude that this phenomenon was influenced by the interaction between the egress flow and the flow in the annulus. The resulting effectiveness curves obtained for the bladeless case followed a conventional shape where an increase in Φ_0 led to a pressurization of the cavity and thus to an increase in the effectiveness, in accordance with the behaviour thoroughly described by Scobie et al. [66]. The use of turned rotor blades led instead to effectiveness curves characterized by the presence of an inflexion over a limited range of Φ_0. Similar results were then found also for the downstream wheel-space.

2.7 Orifice Model at the University of Bath

The Orifice Model (OM) developed at the University of Bath by Professor Owen [9, 10, 14, 18] over the past few decades is a simple yet highly effective tool to determine the sealing effectiveness inside the wheel-spaces of gas turbines. This model is described here in a separate paragraph due to the importance it has assumed over the years and also because it is the theoretical model used in the course of this work to correlate the obtained experimental data. As shown in Figure 2.44, this model was derived by considering the seal as an ideal thin circular membrane with the same dimensions of the clearance. The egress flow originate within the cavity, flows through a stream-tube and then emerges into the external flow by passing through a small orifice characterized by a geometric elemental area δA_e. On the contrary, the ingress flow originate in the main annulus, flows through a different stream-tube and then enters inside the cavity by passing through another small orifice characterized by a geometric elemental area δA_i. The ideal membrane

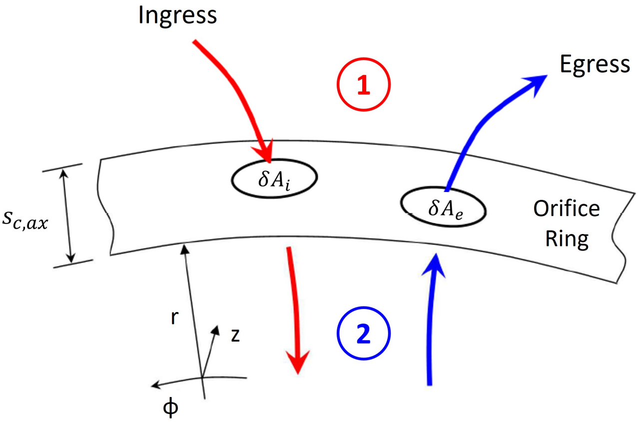

Figure 2.44: Schematic representation of the Orifice Model developed at the University of Bath. Adapted from Sangan [11].

defines a discontinuity in the static pressure which varies from p_1 in the external flow to p_2 in the wheel-space. The model assumes inviscid flow with continuity of mass and energy for both the egress and ingress stream-tubes and the conservation of angular momentum is also applied, ensuring the occurrence of the free-vortex flow. In order to account for viscous losses, two empirical discharge coefficients, $C_{d,e}$ for the egress and $C_{d,i}$ for the ingress, have been incorporated in the model, as previously done also by Johnson et al. [57]. The swirling equations of the OM were derived by Owen [9, 14] for both compressible and incompressible steady 1D flows but, in the latter case, they could be solved analytically. Although the complete derivation of the OM equations is not reported here for the sake of brevity, a set of useful definitions that were used to simplify the resulting solutions that will be later described is provided below. First, the definition of the non-dimensional sealing parameter Φ that was reported in Eq. 2.10 can be rearranged into the following expression:

$$\Phi = \frac{C_w}{2\pi \cdot G_c \cdot Re_\phi} = \frac{U}{\Omega \cdot r_{disk}} \tag{2.18}$$

where U is the bulk-mean velocity through the rim seal clearance. As can be noticed, the viscous terms cancel each other out thus showing that Φ is a pure inertial parameter. Moreover, employing the proper subscripts enables the application of the reported definition of Φ for the sealant flow at inlet (Φ_0), for the egress flow (Φ_e) and for the ingress flow (Φ_i). Then, these definitions can be used to write the continuity equation:

$$\Phi_0 = \Phi_e - \Phi_i \tag{2.19}$$

and the sealing effectiveness equation:

$$\varepsilon = 1 - \frac{\Phi_i}{\Phi_e} = \frac{\Phi_0}{\Phi_e} = \frac{\Phi_0}{\Phi_0 + \Phi_i} \tag{2.20}$$

which is valid when $\Phi_0 < \Phi_{min}$. As stated before, Φ_{min} represents the minimum value of Φ_0 required to completely prevent the ingestion of air inside the wheel-space. Hence, the definition of Φ reported in Eq. 2.18

can be also extended to Φ_{min}:

$$\Phi_{min} = \frac{C_{w,min}}{2\pi \cdot G_c \cdot Re_\phi} = \frac{U_{min}}{\Omega \cdot r_{disk}} \tag{2.21}$$

Another significant quantity of interest for the engine designer is the amount of air ingested inside the cavity when $\Phi_0 < \Phi_{min}$. By using the definition of sealing effectiveness reported in Eq. 2.20, the expression of Φ_i can thus be derived:

$$\frac{\Phi_i}{\Phi_0} = \varepsilon^{-1} - 1 \tag{2.22}$$

Lastly, it is useful to define two additional important parameters. In particular, Γ_c represents the ratio between the two discharge coefficients:

$$\Gamma_c = \frac{C_{d,i}}{C_{d,e}} \tag{2.23}$$

while ΔC_p, which represents the non-dimensional pressure difference in the external flow, is commonly considered to be the driver for ingress in the EI regime:

$$\Delta C_p = \frac{\Delta p}{\frac{1}{2} \cdot \rho \cdot \Omega^2 \cdot r_{disk}^2} \tag{2.24}$$

It is worth to notice that the definition of ΔC_p reported in Eq. 2.24 is equivalent to the definition used by Sangan et al. [8] that was reported in Eq. 2.17.

2.7.1 Effectiveness equation for RI ingress

The complex set of equations that was derived by Owen to determine the ingestion in the RI regime is reported in the Appendix B of his work [14]. However, these equations were rearranged by Sangan et al. [15] in order to obtain an explicit RI effectiveness equation:

$$\frac{\Phi_0}{\Phi_{min,RI}} = \frac{\varepsilon}{\left[1 + (1-\varepsilon)^{\frac{1}{2}}\right] \cdot \left[1 + \Gamma_c^{-2} \cdot (1-\varepsilon)\right]^{\frac{1}{2}}} \tag{2.25}$$

that was subsequently validated through the use of the obtained experimental results. As can be noticed, for values of $\Phi_0 > \Phi_{min,RI}$ the effectiveness will be equal to one and the cavity will be fully sealed. Moreover, by combining Eq. 2.20 and Eq. 2.22 with Eq. 2.25 it was possible to obtain an expression that can be used to determine the non-dimensional ingress flow rate for the RI regime:

$$\frac{\Phi_{i,RI}}{\Phi_{min,RI}} = \frac{1-\varepsilon}{\left[1+(1-\varepsilon)^{\frac{1}{2}}\right] \cdot \left[1+\Gamma_c^{-2} \cdot (1-\varepsilon)\right]^{\frac{1}{2}}} \tag{2.26}$$

Thus, the variation of ε, Φ_e and Φ_i with Φ_0 obtained by employing the above RI equations and by assuming $\Gamma_c = 1$ is shown in Figure 2.45.

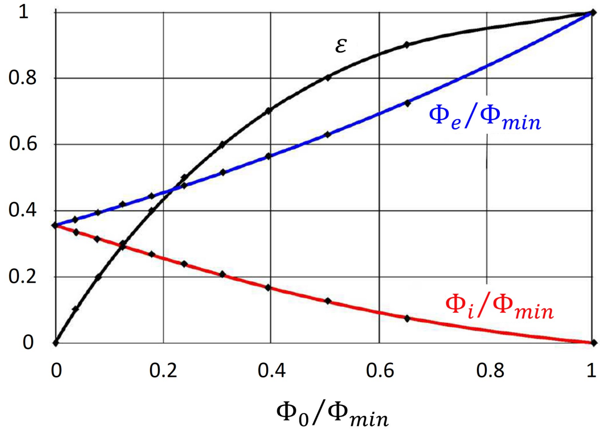

Figure 2.45: Variation of ε, Φ_e and Φ_i with Φ_0 obtained for the RI regime by assuming a value of $\Gamma_c = 1$. Adapted from Sangan [11].

2.7.2 Effectiveness equation for EI ingress

The complex set of equations used to determine the ingestion in the EI regime can be derived if the circumferential pressure distribution in the external annulus flow is known. Therefore, Owen [10] demonstrated that employing the saw-tooth approximation shown in Figure 2.46 enables analytical integration of the equations, whereas other distributions (cosine and experimentally determined pressure profile) require a numerical integration. Moreover, the saw-tooth model provided results in good agreement with both experimental and CFD data and it was thus used to derive the following equation for the EI regime:

$$\Phi_{min,EI} = \frac{2}{3} \cdot C_{d,e} \cdot \Delta C_p^{\frac{1}{2}} \tag{2.27}$$

However, as for the RI case, the equations derived by Owen were rearranged by Sangan et al. [8] in order to obtain an explicit EI effectiveness equation:

$$\frac{\Phi_0}{\Phi_{min,EI}} = \frac{\varepsilon}{\left[1 + \Gamma_c^{-\frac{2}{3}} \cdot (1-\varepsilon)^{\frac{2}{3}}\right]^{\frac{3}{2}}} \tag{2.28}$$

that was subsequently validated through the use of the obtained experimental results. As can be noticed, for values of $\Phi_0 > \Phi_{min,EI}$ the effectiveness will be equal to one and the cavity will be fully sealed. More-

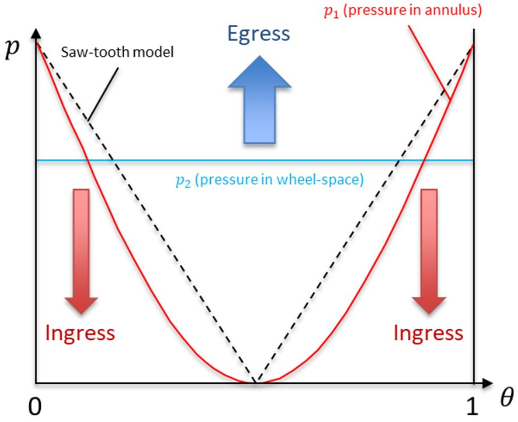

Figure 2.46: Saw-tooth model used to derive the OM equations for the EI regime. Adapted from Sangan [11].

over, by combining Eq. 2.20 and Eq. 2.22 with Eq. 2.28 it was possible to obtain an expression that can be used to determine the non-dimensional ingress flow rate for the EI regime:

$$\frac{\Phi_{i,EI}}{\Phi_{min,EI}} = \frac{1-\varepsilon}{\left[1+\Gamma_c^{-\frac{2}{3}}\cdot(1-\varepsilon)^{\frac{2}{3}}\right]^{\frac{3}{2}}} \tag{2.29}$$

The variation of ε with Φ_0 obtained by employing the above EI equations will have a qualitatively similar shape to that obtained for the RI regime which was reported in Figure 2.45. However, it is also interesting to notice from Figure 2.47 that different values of Γ_c will have an effect on the shape of the curves and in particular on their gradient. In conclusion, the advantage of using the solution of the OM equations is that they allow the correlation of the effectiveness data obtained from experiments by decoupling the cause (external pressure coefficient ΔC_p) from the effect (ingress level and thus effectiveness ε). Nevertheless, it is crucial to bear in mind that, as stated by Owen et al. [10], the correct value of ΔC_p

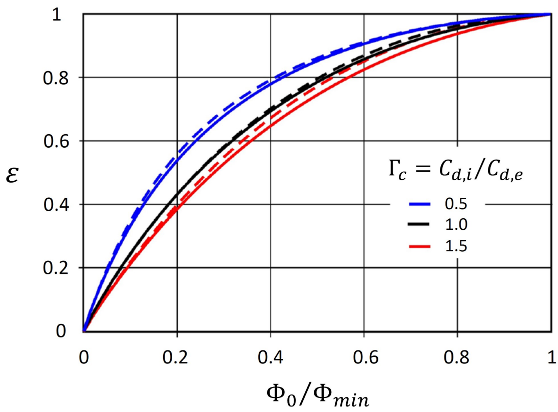

Figure 2.47: Variation of ε with Φ_0 obtained for different values of Γ_c. Comparison between EI regime (solid line) and RI regime (dashed line). Adapted from Sangan [11].

to be used in Eq. 2.27 must always be determined within the annulus locations defined by the consistency criterion. This criterion relies on the definition of a normalized axisymmetric pressure:

$$g = \frac{p_2 - p_{1,min}}{p_{1,max} - p_{1,min}} \tag{2.30}$$

that when calculated in the case of total absence of purge flow ($\Phi_0 = 0$) is renamed to g^*. By employing the usual saw-tooth approximation, the definition of g^* becomes:

$$g^* = \frac{1}{1 + \Gamma_c^{-\frac{2}{3}}} \tag{2.31}$$

Hence, after calculating the value of Γ_c by interpolating the experimental data with the Orifice Model, it is possible to use Eq. 2.31 to determine g^*. In the end, the positions within the annulus where g equals g^* indicate the locations where the pressure fluctuations ($p_1(\theta)$ and consequently ΔC_p) are consistent with the value of Γ_c determined by using the relationship between Φ_0 and ε.

2.8 Buffer Ratio model at the University of Bath

The experimental data that were obtained by Cho et al. [12] on the rotor side have been then used by Mear et al. [13] to derive a theoretical Buffer Ratio (BR) model that is based on the assumption that a buffer layer generated by the boundary layer on the rotor protects the rotating disk from the effects of ingestion. This phenomenon can be better explained by looking at Figure 2.48 where the effects of different sealing flow rates on the flow structure developing inside the cavity are reported. As can be noticed, the color of the arrows represent the different concentration inside the boundary layer of both the stator and the rotor side. In particular, Figure 2.48a represents the case of total absence of sealing flow ($\Phi_0 = 0$) where the concentration inside the wheel-space must be uniform and equal to $c_R = c_S = c_{an}$. Figure 2.48b shows instead the case where a certain quantity of sealing flow with concentration $c_0 > c_{an}$

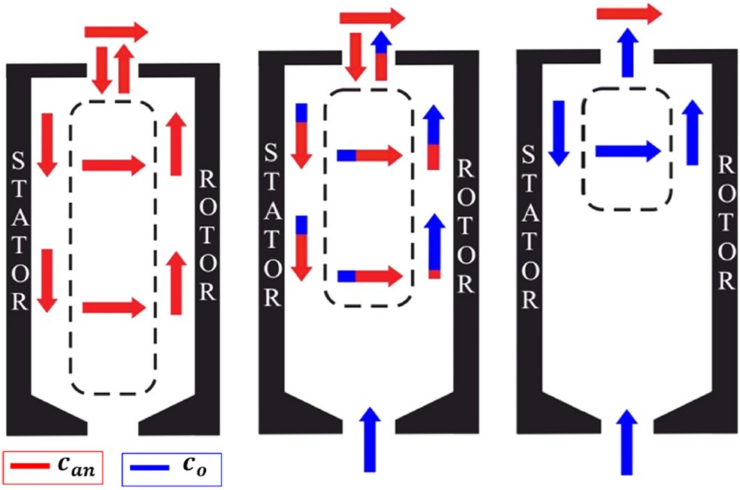

(a) $\Phi_0 = 0$ (b) $\Phi_0 < \Phi_{min}$ (c) $\Phi_0 = \Phi_{min}$

Figure 2.48: Schematic representation of the buffer effect with the flow structure developing at (a) $\Phi_0 = 0$, (b) $\Phi_0 < \Phi_{min}$ and (c) $\Phi_0 = \Phi_{min}$. Adapted from Mear et al. [13].

enters the cavity. However, this quantity is not sufficient to completely prevent the ingestion ($\Phi_0 < \Phi_{min}$) and a certain amount of ingress is present on the stator side. From here, the flow passes across the rotating core and mixes with the sealing flow that is being pumped up by the rotor surface, thus resulting in a concentration value $c_R > c_S$. In addition, the concentration on the rotor side can be seen to decrease with the radius. Then, Figure 2.48c represents the case of completely sealed cavity ($\Phi_0 = \Phi_{min}$) where the concentration inside the wheel-space must be again uniform but this time equal to $c_R = c_S = c_0$. The development of the BR model started by adapting the definition of sealing effectiveness reported in Eq. 2.9 in order to use it on the stator side:

$$\varepsilon_S = \frac{c_S - c_{an}}{c_0 - c_{an}} \tag{2.32}$$

and on the rotor side:

$$\varepsilon_R = \frac{c_R - c_{an}}{c_0 - c_{an}} \tag{2.33}$$

From these definitions the parameter $\Delta\varepsilon$, that represents the buffer effect, was derived:

$$\Delta\varepsilon = \varepsilon_R - \varepsilon_S = \frac{c_R - c_S}{c_0 - c_{an}} \tag{2.34}$$

and then, by defining the buffer ratio BR as follows:

$$BR = \frac{\varepsilon_R - \varepsilon_S}{1 - \varepsilon_S} = \frac{c_R - c_S}{c_0 - c_S} \tag{2.35}$$

it was possible to rearrange Eq. 2.34 into the following form:

$$\Delta\varepsilon = BR \cdot (1 - \varepsilon_S) \tag{2.36}$$

Subsequently, the previously reported description of the flow structure that develops inside the cavity allowed the authors to derive an explicit expression to determine the value of the buffer ratio:

$$BR = exp\left(-A \cdot \left(\frac{\Phi_{min}}{\Phi_0} - 1\right)^n\right) \tag{2.37}$$

which implies that $BR \to 0$ when $\Phi_0 \to 0$, $c_R \to c_S$ and that $BR \to 1$ when $\Phi_0 \to \Phi_{min}$, $c_R \to c_0$. Moreover, A and n represent empirical constants that have to be determined experimentally. The BR model was then successfully validated with the experimental data obtained by Cho et al. [12] thus becoming a useful tool to predict the sealing effectiveness on the rotor side.

Chapter 3

Design of the test rig

Contents

3.1 Test rig overview

According to the expected outcomes of this Ph.D. work, which were described at the end of Chapter 1, a new Rotating Cavity Rig has been developed to experimentally investigate the ingestion of hot gas inside the stator-rotor cavity of an axial turbine stage. The purpose of this chapter is to describe the design of the facility which has been conducted by performing CFD simulations of the external annulus flow and FEM simulations to verify the suitability of the chosen layout in terms of stress, deformation and vibration values. Moreover, the nominal operating conditions of the test rig will be compared with those of the different hot gas ingestion experimental facilities present in literature. A photograph of the single stage test rig, installed in the THT Lab of the University of Florence, can be seen in Figure 3.1.

Figure 3.1: Photograph of the single stage test rig installed in the THT Lab of the University of Florence.

3.2 Description of the test rig

The complete 3D model of the experimental facility is shown in Figure 3.2 where its four main macro components are indicated in red: feeding volute, stator frame, rotor frame and basement. Although Figure 3.2 illustrates the entrance position of both the flowpath and the purge flow, a more detailed view of the directions of the two flows is provided in the cross section of the test rig reported in Figure 3.3. Here, the test section constituted by a stator disk which features 44 integrated vanes and a rotor disk which instead features 66 integrated blades can be observed. On each disk, it is possible to fit a cover plate that has been designed as to represent a real engine rim seal as close as possible. Moreover, the interchangeability and modularity of the covers allow replacing them with different geometries in order to evaluate the impact of different

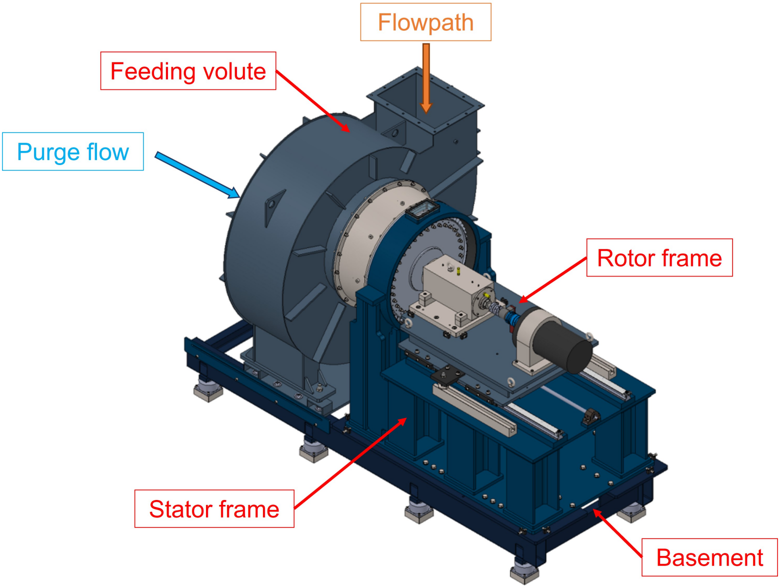

Figure 3.2: Complete 3D model of the Rotating Cavity Rig.

geometrical parameters on the sealing performance. For this purpose, standard pressure and CO_2 gas sampling measurements can be performed on the stator surface, as per standard practice in literature. However, the main innovation of the current test rig resides in the possibility to employ optical measurement techniques such as Pressure Sensitive Paint (PSP) to obtain 2D effectiveness maps on both the stator and the rotor sides of the cavity through the optical accesses placed on the stator disk. Moreover, the convergent duct that feeds the turbine stage can also be observed. The presence of a feeding volute located before the convergent duct enables the uniform distribution of the annulus flow in the circumferential direction. Although the use of a spiral design for the volute is rather unconventional for this kind of experimental facilities, it is necessary to leave an optical access to the back of the test rig to perform PSP measurements.

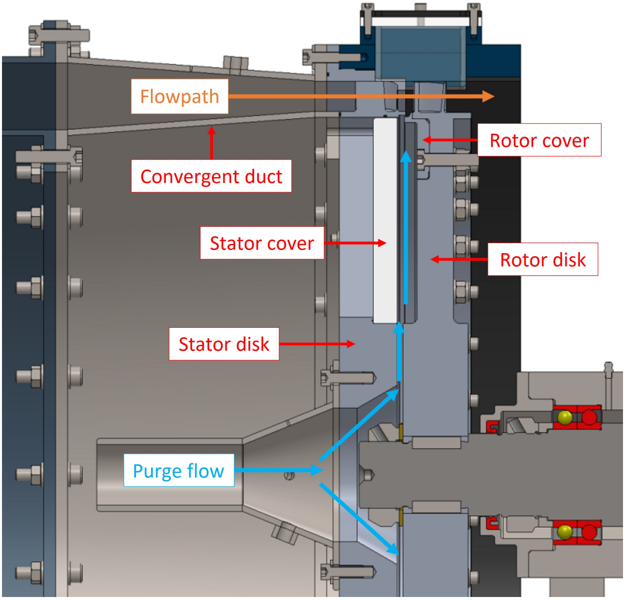

Figure 3.3: Cross section of the Rotating Cavity Rig.

3.3 Operating conditions of the test rig

The present test rig has been designed to be operated under non-reactive conditions. However, despite the undeniable differences with the operating conditions of actual gas turbines, the cold flow approach is consistent with the majority of the experimental facilities described in literature (see Chapter 2). By using this approach, it is in fact possible to avoid the necessity of more complex and thus expensive setups that operate at higher temperature and pressure. Moreover, the validity of this approach has been further confirmed by Boutet-Blais et al. [67] who performed CFD simulations to compare the effectiveness values obtained by monitoring a CO_2 tracker injected in a cold rig with the thermal effectiveness values obtained on the same setup but run under actual engine operating conditions. As shown in Figure 3.4, both the ingress (I and III) and egress (II and IV) conditions were compared for the two investigated setups. Although the values of the thermal effectiveness were found to be slightly lower due to the temperature rise resulting from the viscous work term, which has no equivalent in the cold rig, both setups

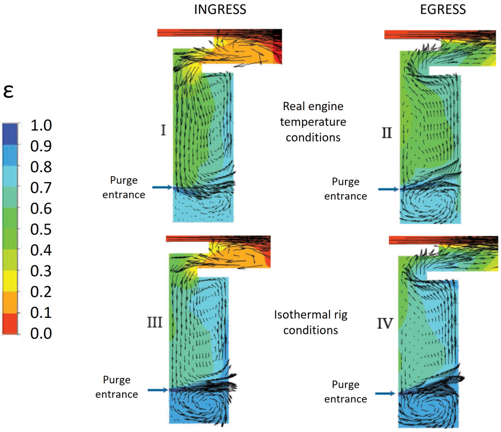

Figure 3.4: Effectiveness maps obtained for the hot and cold CFD setup at both ingress (I and III) and egress (II and IV) conditions [67].

exhibited a very similar behaviour thus proving the validity of this widely employed approach. Another point worth mentioning is that the values of Re_Φ commonly observed in actual gas turbines typically fall within the range $2-3\times10^7$ [21]. According to Figure 3.5, this value is approximately an order of magnitude higher than the majority of the values commonly found in the experimental facilities present in literature. However, as stated by Wisler [68], this size and speed scaling enables experiments to be conducted with greater accuracy as well as reduced cost and risk. In addition, as shown by Owen and Rogers [26] and then later experimentally demonstrated by Sangan et al. [8], this discrepancy does not represent a significant issue since gas turbine stages with similar velocity triangles exhibit only a weak sensitivity to Re_Φ. In conclusion, the operating point of the current facility has been included in Figure 3.5 which highlights that it will be run under conditions similar to those of the majority of the hot gas ingestion experimental facilities present in literature.

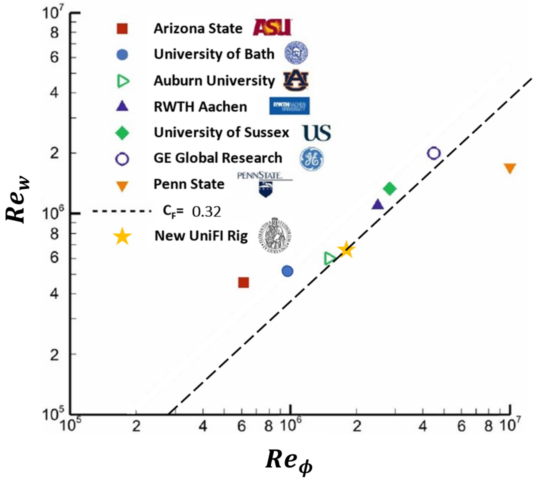

Figure 3.5: Operating points in terms of Re_w and Re_Φ of the different hot gas ingestion experimental facilities present in literature. Adapted from Scobie et al. [66].

3.4 CFD design of the facility

The design of the facility, which has been thoroughly described in Orsini et al. [69], began with a detailed characterization of the test section in order to determine the optimal number and shape of both the vanes and the blades. This selection was crucial in order to achieve the desired fluid-dynamic conditions necessary to study the phenomenon of hot gas ingestion. Initially, a preliminary 1D analysis was conducted to determine the design velocity triangles shown in Figure 3.6 that are necessary to ensure the compliance with the overall rig requirements and to confirm the feasibility of the design. As can be noticed, for simplicity it has been assumed that at the entrance of the test section the flow has a purely axial velocity W (coming from above) and, consequently, the resulting vane inlet angle is equal to 0 deg. The rotor blades rotate at an angular velocity Ω thus being responsible for the tangential velocity component $\Omega \cdot r_{disk}$. Moreover, in the stator frame of reference the flow exits from the vanes with a velocity C which is inclined at an angle α while, in the rotating frame of reference, the vane exit velocity is equal to V and it has an inclination equal to β with respect to the axial direction.

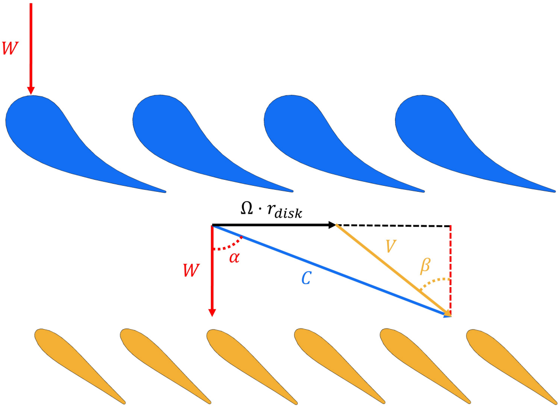

Figure 3.6: Preliminary design velocity triangles.

Subsequently, the TRAF computational code [70] was used to carry out a detailed design by performing uncooled steady CFD simulations. The TRAF code, which has been successfully validated and used in a large number of turbomachinery applications [71, 72, 73], is a Q3D/3D multi-row and multi-block CFD solver for RANS/URANS equations. For the purpose of this work, it is worth to point out that all the results presented in this section have been obtained by performing 3D numerical simulations which employ meshes of approximately 2×10^6 cells. Moreover, the standard mixing plane approach and the Wilcox's $\kappa - \omega$ turbulence model were used to perform the computations. The main geometrical parameters and the resulting maximum operating conditions of the current facility are respectively reported in Table 3.1 and Table 3.2. Given the number of vanes (44) and blades (66), two nozzles and three blades have been simulated in order to simplify the comparison with eventual future unsteady calculations. Moreover, the flow path incorporates a few geometrical simplifications such as constant tip and hub radius while the nozzles and the blades are uncooled and designed to maintain a constant section along the span. As shown earlier in Figure 3.6, the velocity triangle has been designed with the intent to achieve a value of the vane

Table 3.1: Main geometrical parameters of the test rig.

Parameter	**Dimension**
Number of vanes	44
Number of blades	66
Vane exit angle	75.8 [deg]
Blade inlet/exit angle	51 [deg]
Hub radius	300 [mm]
Tip radius	325 [mm]
Vane aspect ratio	0.718 [-]
Blade aspect ratio	0.927 [-]
Vane hub solidity	0.779 [-]
Blade hub solidity	0.906 [-]
Interstage distance	13 [mm]

Table 3.2: Maximum operating conditions of the test rig.

Parameter	**Dimension**
Rotational velocity	3000 [RPM]
Total pressure (vane inlet)	1.15 [bar]
Total temperature (vane inlet)	35 [°C]
Mass flow rate (vane inlet)	1.80 [kg/s]
Mach number (vane exit)	0.43 [-]
Developed power	-0.97 [kW]
Axial Reynolds number	6.75×10^5 [-]
Rotational Reynolds number	1.82×10^6 [-]

exit angle (α) which exceeds 70 deg, aiming to be representative of the first stage nozzle of an HPT. In addition, despite not being fully engine representative, the blade has been designed unturned since a symmetric profile enables the minimization of the developed power especially when the rig is operated at off-design conditions. In fact, as demonstrated also by Sangan et al. [8], a configuration where the shaft absorbs power has two important advantages: firstly, there is no need to dissipate the otherwise produced power thus avoiding the necessity to employ a dynamometer and, secondly, it is inherently safer as any potential failure of the motor would lead to the unavoidable deceleration of the shaft. Consequently, the value of the blade inlet/exit angle (β) has been set at 51 deg in order to absorb the desired power at design conditions. Furthermore, the need to reduce the value of the mass flow rate led to the adoption of aspect ratios lower than 1.0, despite the significant deviation from the values found in real engines. However, this choice does not represent a limitation since the results of the CFD simulations performed by Berdanier et al. [74] have confirmed that the channel height does not have a significant impact on the resulting effectiveness values within the wheel-space. On the contrary, to ensure consistency with an actual engine, the values of hub solidity and interstage distance have been kept coherent with those observed in real engines due to their potentially significant influence on the seal pressure distribution. Consequently, the selected values of hub solidity and interstage distance alongside the thick shape of the vanes LE ensured a realistic unsteady pressure distribution in the flowpath despite the presence of unturned blades. Moreover, the vane exit Mach number exceeds 0.4, which has been considered an acceptable value despite being significantly different from the typical values found in an HPT. However, as explained in Da Soghe et al. [75], the differences in terms of main annulus Mach number between test rig and engine do not affect the ability of the rig to satisfactorily match the engine data. A deeper insight into the distribution of the Mach number is presented in Figure 3.7, which displays the Mach contour at midspan as predicted by the TRAF code. As can be observed, the flow exhibits smooth incidences and sufficiently regular pressure gradients that confirmed the correct design of the flowpath.

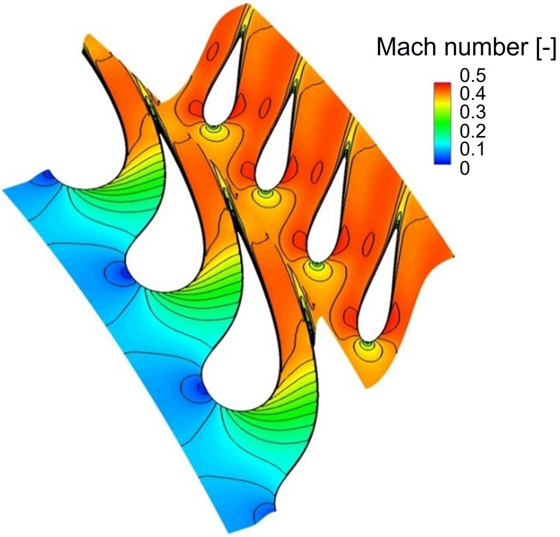

Figure 3.7: Contour of Mach number at midspan as predicted by the TRAF code [69]. © 2024 Baker Hughes Company - All rights reserved

3.4.1 Feeding system design

The feeding system placed upstream of the test section has been then numerically simulated in order to evaluate its performance in terms of both flow uniformity and pressure losses, thus improving the fluid-dynamic characterization of the flowpath. The numerical domain employed to perform the simulations is shown in Figure 3.8 and it consists of the volume enclosed by the volute, the convergent duct and the vane passage area. A final extrusion was then added at the stator exit in order to prevent backflow issues. The commercial software Ansys Fluent v.194 was employed to perform steady RANS simulations on a poly-hexa mesh with 20 prisms near the walls and a total of 15.3 million elements, resulting in a good compromise between accuracy and computational time. Regarding the boundary conditions, as shown in Figure 3.8, the mass flow rate, the total temperature and the turbulence intensity were set at the inlet of the

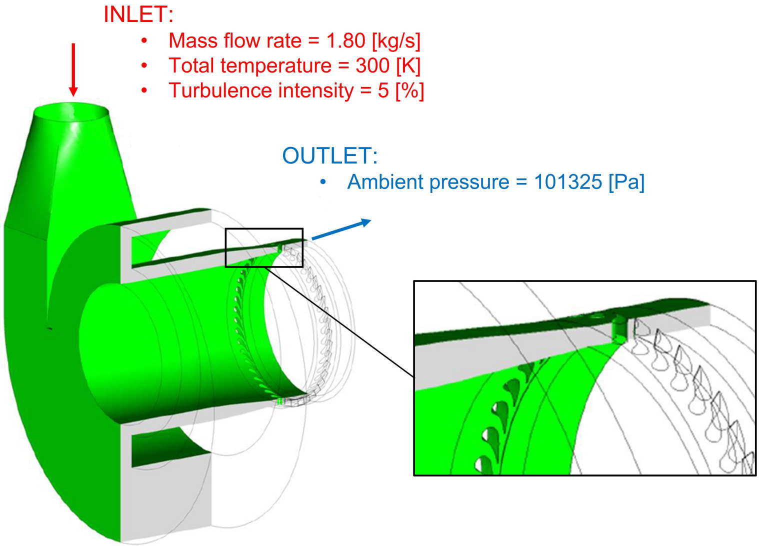

Figure 3.8: Numerical domain employed to perform the CFD simulations of the feeding system [69].

volute while ambient pressure was set at the outlet of the test section. The solid surfaces were modelled as adiabatic and treated as no-slip walls while the ideal gas model was chosen for the working fluid (air). Additionally, the $\kappa - \omega$ SST turbulence model was employed in combination with an automatic wall treatment. Regarding the obtained results, the numerical simulations estimated that the average static pressure at the inlet of the volute is approximately 14750 Pa. When comparing this result with the contour reported in Figure 3.9b, which has been obtained on a plane placed at the exit of the convergent duct (= stator inlet), it can be observed that the pressure loss connected to the feeding system is approximately equal to an average value of 600 Pa. Although this value was considered sufficiently low to meet the requirement of minimizing pressure losses, a slight non-uniformity could be noticed at the stator inlet due to the absence of blades in the radial diffuser placed upstream of the convergent duct. However, the more critical aspect lies in the determination of the circumferential uniformity in correspondence of the rim seal region which is placed at the stator exit. To address this concern, Figure 3.10 displays both the velocity (Figure 3.10a) and the pressure (Figure 3.10b) contours alongside the respective polar diagrams (Figure 3.10c and Figure 3.10d) that have been extracted on a plane located 0.3 mm downstream

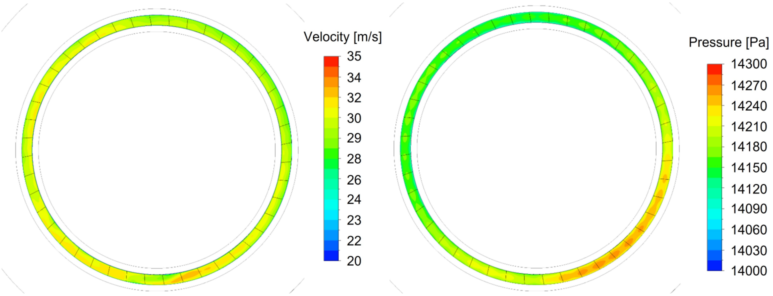

(a) Velocity contour *(b) Pressure contour*

Figure 3.9: Resulting contours of (a) Velocity and (b) Pressure obtained at the exit of the convergent duct [69].

of the TE of the vanes. According to these results, it is thus possible to conclude that the stator vanes are able to effectively smooth out the modest circumferential flow non-uniformities observed at the exit of the convergent duct, therefore assuring to perform accurate hot gas ingestion measurements in correspondence of the rim seal region.

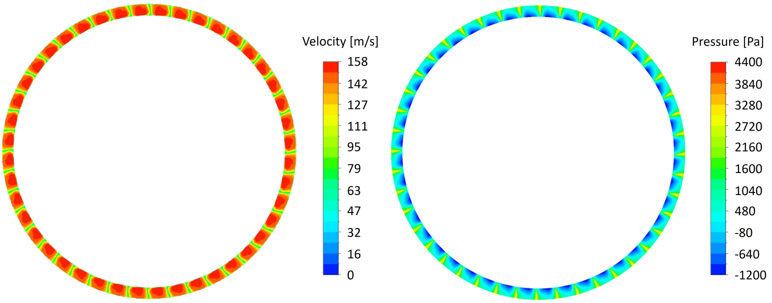

(a) Velocity contour *(b) Pressure contour*

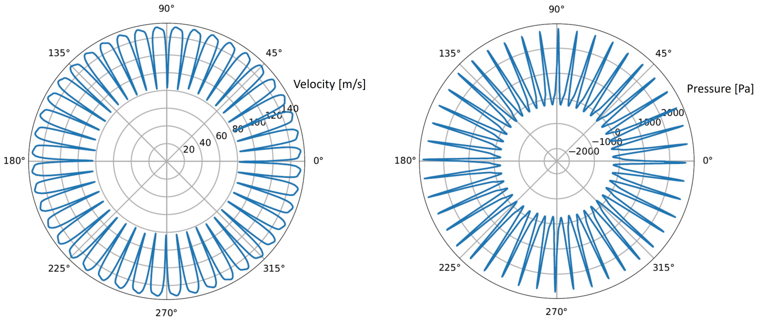

(c) Velocity polar diagram *(d) Pressure polar diagram*

Figure 3.10: Resulting contours of (a) Velocity and (b) Pressure alongside the polar diagrams of (c) Velocity and (d) Pressure obtained at the exit of the stator [69].

3.5 FEM design of the facility

The mechanical design of the facility has been conducted by performing multiple FEM simulations with the commercial software Ansys v.194. These simulations, which will be described in detail in the following subsections, can be divided into three main categories:

- Static structural simulations (Section 3.5.1);
- Dynamic modal simulations (Section 3.5.2);
- Dynamic harmonic simulations (Section 3.5.3).

3.5.1 Static structural simulations

Regarding the structural simulations, since the rotor disk and its relative cover are the key components of the whole test rig, significant emphasis has been placed on the analysis of the stress and deformation values of these two components. To achieve this objective and considering the axisymmetry of the setup, the numerical domain has been limited to the periodic sector reported in Figure 3.11a, which corresponds to the pitch between two consecutive bolts employed to anchor the cover to the rotor disk. For this reason, rotational periodicity has been enforced between the two sides of the domain while circumferential and axial constraints have been applied at the disk bore. Regarding the materials, aluminium has been selected for both the rotor disk and its cover while standard steel has been selected for the bolt.

Concerning the applied loads, as shown in Figure 3.11b, a rotational velocity of 3000 RPM has been gradually applied with a ramp-up approach to all the bodies within the numerical domain while a pretension value of 15 kN has been applied to the bolt. The most suitable pretension value has been chosen according to a sensitivity analysis (not reported here for the sake of brevity) where the results obtained for a pretension of either 10, 15, 20 or 25 kN have been compared. The results of these simulations have shown that increasing the preload applied to the bolt leads to higher stresses on the aluminium disk caused by the imprinting of the bolt head.

In particular, a linear relationship has been found between the pretension applied to the bolt and the stress measured on the rotor disk. In this regard, it has been decided that a preload of 15 kN represents a good compromise between the necessity to reduce the stress on the aluminium and the mandatory requirement to prevent the potential detachment of the cover from the rotor disk during the rig operation. Additionally, since the test rig will be always operated at cold flow conditions, no heat load has been applied and the temperature has been set to a constant value of 20 °C.

Subsequently, since the choice of the contact type between the different components turns out to be a critical aspect to obtain physical results, the contacts shown in Figure 3.11c have been selected as the most suitable for the current simulation. The choice to employ non-linear frictional contacts is particularly important and it has been dictated by the necessity to simulate a more realistic situation despite causing a considerable rise in the computational time. For the present case, the friction coefficient has been set equal to 0.15 after performing a sensitivity analysis (not reported here for the sake of brevity) where the results obtained by setting either 0.10, 0.15 or 0.20 have been compared. The results of these simulations have shown that the employed value of the friction coefficient does not substantially impact either the stress values obtained on the bolts or the status of the contact between the disk and the cover, which remains assured due to the chosen preload of 15 kN. In this regard, it has been decided that a reasonable intermediate value of 0.15 is well suitable for the current simulation.

Lastly, the mesh employed to perform the simulations is shown in Figure 3.11d. It consisted of a combination of both tetrahedral and hexahedral elements which were generated by setting the global sizing equal to 3 mm. Then, additional local refinements were added in order to well capture the gradients in specific regions such as the disk-cover contact surface (1.5 mm), the bolt surface (1 mm) and the regions with small chamfers and fillets (0.2 mm). The total number of elements approached nearly 1.77×10^5.

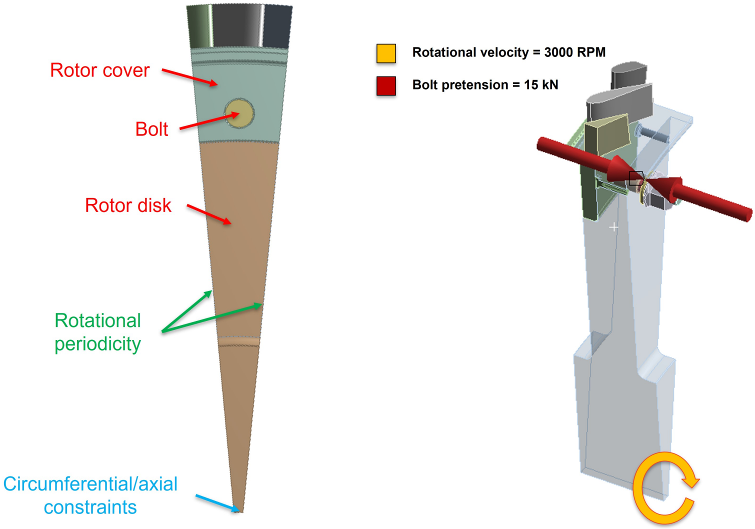

(a) Periodic domain and constraints *(b) Applied loads*

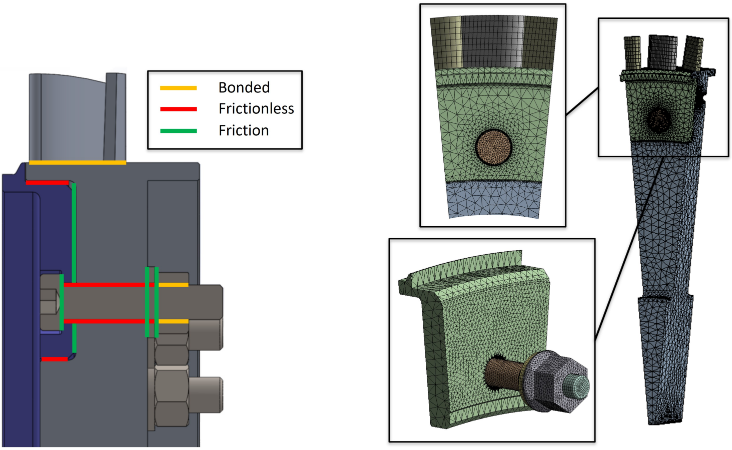

(c) Contacts *(d) Mesh*

Figure 3.11: Main settings of the setup employed to carry out the static structural FEM simulations: (a) Periodic domain and constraints, (b) Applied loads, (c) Contacts between the different components and (d) Mesh with details of the local refinements [69].

The most suitable mesh was chosen according to a sensitivity analysis where three different meshes (coarse, medium and fine) obtained by varying the value of the global sizing were compared. The selection criterion was based on the comparison of the radial deformation values obtained in correspondence of the seal tooth of the rotor cover (see Figure 3.12a). This approach was chosen because the value of radial deformation obtained in this region have a direct impact on the actual value of the radial gap that characterizes the different rim seal geometries. As shown in Figure 3.12b, an excessively coarse mesh overpredicts the values of radial deformation while increasing the number of elements progressively results in lower deformation values although at the expense of increasing the computational cost. Since the current setup had the goal to provide an accurate yet fast tool to define the different geometries to be tested, the medium mesh was considered to be the best compromise between computational time and accuracy, also proving to be conservative when compared to the fine mesh.

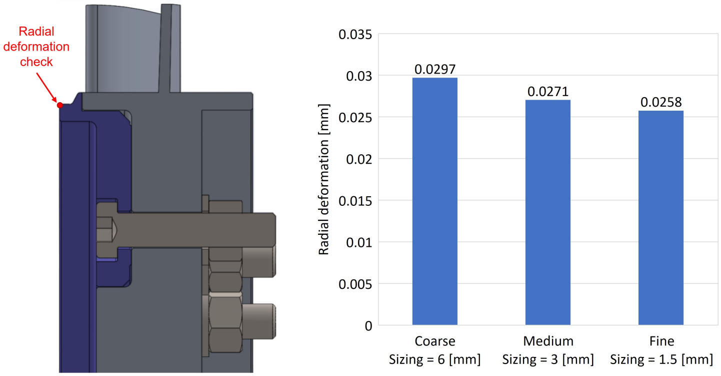

(a) Check position *(b) Results of the mesh sensitivity*

Figure 3.12: Mesh sensitivity for the static structural simulations: (a) Position where the radial deformation values have been measured and (b) Results of the mesh sensitivity.

The results of the structural simulation indicate that, as shown in Figure 3.13, the highest stress for the aluminium components occurs in correspondence of the contact surface between the bolt and the rotor cover. Although the mechanical stress in this region reaches a value of approximately 211 MPa, the yield tensile strength of Al7050 T7451 ensures a safety factor greater than 2. Additionally, it is important to notice that this maximum stress value appears to be axisymmetric since being mostly due to the applied pretension of 15 kN and localized near the edge. Hence, it can be attributed to the presence of a small fillet which acts as a stress concentration factor.

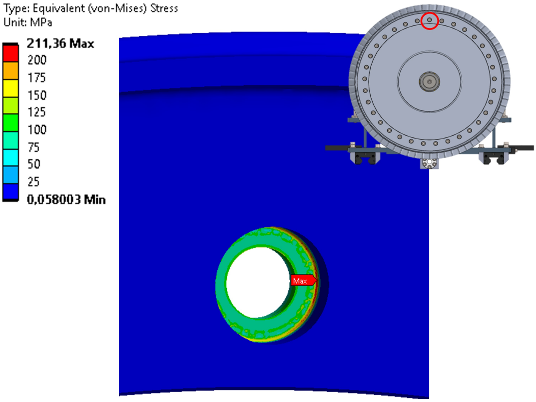

Figure 3.13: Contour of equivalent von-Mises stress over the cover [69].

Then, it is also interesting to evaluate the impact of the centrifugal load by comparing the stress values obtained on the bolt between a non-rotating case and the case with the nominal rotational speed of 3000 RPM. Hence, a maximum stress of approximately 500 MPa was found but with marginal differences between the two cases. In this regard, given the mechanical properties of the structural steel selected for the bolts, such stress values do not raise any significant concern. The centrifugal load is not a concern either for the blades since their very low mass results in a stress at the blade hub that remains below 2 MPa.

Moreover, the suitability of the chosen pretension load to avoid the potential detachment of the cover from the rotor disk during the operation of the test rig can be further confirmed by looking at both the resulting contours of contact pressure (Figure 3.14a) and residual gap (Figure 3.14b) between the two components. As can be seen, the selected bolt pretension ensures that the contact pressure remains consistently greater than zero across the entire surface, with an average value of approximately 23.44 MPa. In parallel, the residual gap between the two components has an average value over the entire contact surface approximately equal to 0 mm. These two results definitively confirm that the pretension of 15 kN is sufficient to effectively prevent any dangerous detachment of the cover from the rotor disk during the operation of the rig.

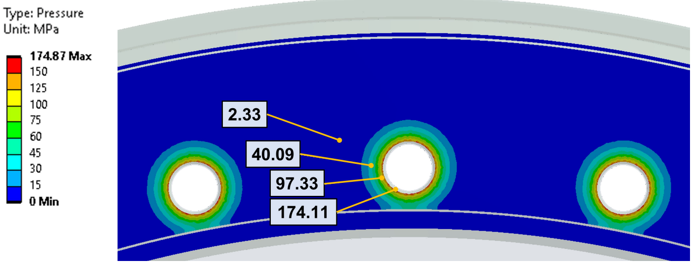

(a) Disk-cover contact pressure

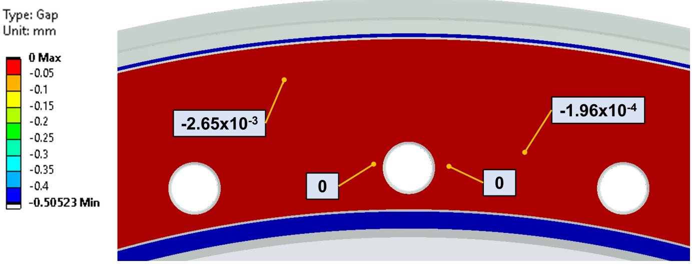

(b) Disk-cover residual gap

Figure 3.14: Resulting (a) Contact pressure and (b) Residual Gap between the cover and the rotor disk during the operation of the test rig.

Finally, a conclusive contour of the equivalent von-Mises stress distribution over the whole simulated sector is provided in Figure 3.15. The plot highlights that the stress on both the rotor disk and the cover is generally very low across the entire domain, except for the relatively higher values in the area affected by the bolt pretension. However, these values of stress do not represent an issue given the selected aluminium alloy. Concerning the fatigue analysis necessary to assess the lifespan of the rotor disk, it was noted that an ”infinite life” can be reasonably expected due to the relatively small magnitude of the loads and the limited number of cycles to which the test rig will be subjected.

In order to complete the analysis, it is also important to check the obtained values of radial deformation. For this reason, a contour depicting the distribution of these values over the whole simulated sector is provided in Figure 3.16. Hence, the following observations can be made by taking into consideration the highlighted positions:

- **A and B** → Both the back and the front sides of the rotor platform exhibit a very similar behaviour thus indicating that the center of mass is well-positioned. Hence, this allows avoiding potential bending and dishing effects;

- **C and D** → Close values of deformation near the contact interface between the disk and the cover suggest that the selected pretension value applied to the bolt effectively limits the reciprocal sliding of the two components, ensuring enhanced stability;

- **E** → The radial deformation of the rim seal lip is a critical parameter which has a direct impact on the actual value of radial seal clearance during the experiments. However, the value of radial deformation obtained in this region is approximately equal to 2.7×10^{-2} mm, a very low value which can be considered perfectly suitable for the purpose of this investigation.

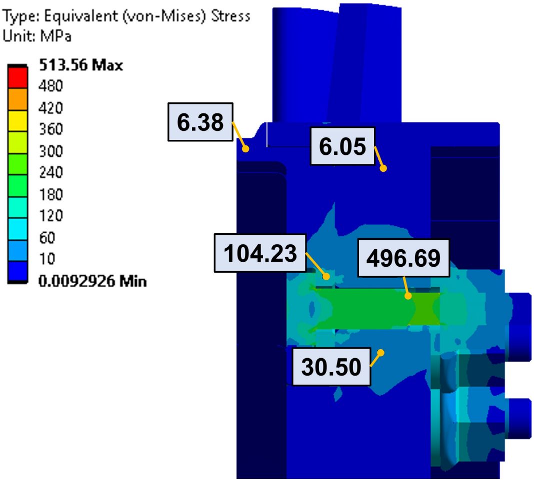

Figure 3.15: Contour of equivalent von-Mises stress over the whole simulated sector [69].

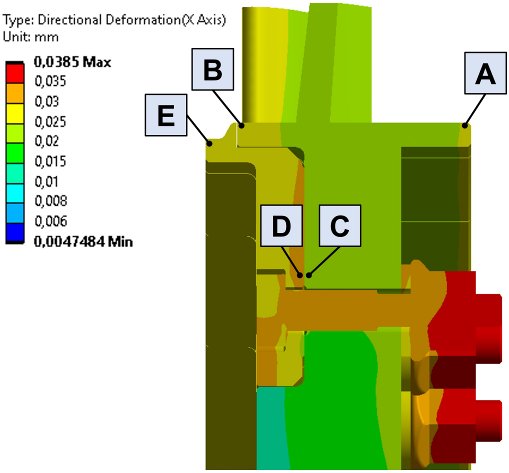

Figure 3.16: Contour of radial deformation over the whole simulated sector [69].

3.5.2 Dynamic modal simulations

The setup employed to perform the dynamic modal simulations is comparable to the one used for the structural simulations but with a few distinctions that are outlined below:

- The entire disk with the addition of the shaft, the bearings case and the supporting frame has been simulated by using a mesh that reached approximately 1×10^6 elements. (see Figure 3.17);
- The model has been treated as a single rigid body in order to ease the convergence;
- The bearings have been treated as shaft-case (body-body) connections (see Figure 3.18) and their stiffness values, which are summarized in Table 3.3 and Table 3.4, have been directly provided by the manufacturer (SKF). As can be seen, only the diagonal terms, K_{xx} and K_{yy} in the radial directions and K_{zz} in the axial direction, have been considered. On the other hand, the damping values have been set to zero to simulate the most severe condition.

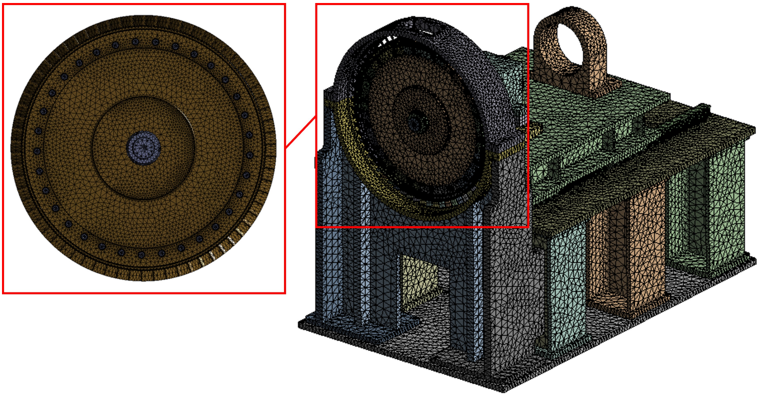

Figure 3.17: Domain and mesh of the dynamic modal simulations.

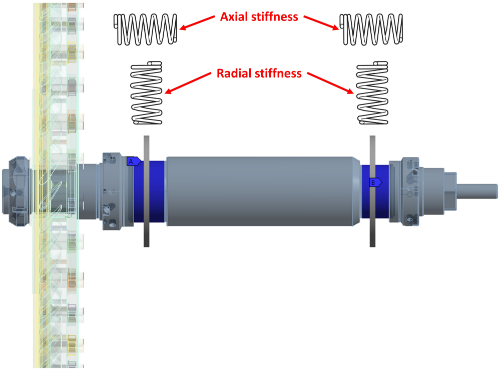

Figure 3.18: Bearings schematization for the dynamic modal simulations.

Table 3.3: Stiffness coefficients K_{xx}, K_{yy} and K_{zz} for the coupled 7015 ACD bearings.

Stiffness coefficients for the coupled 7015 ACD bearings [N/m]			
Force [N]	1/Displacement [1/m]		
	$1/\delta_x$	$1/\delta_y$	$1/\delta_z$
F_x	9.01×10^8	-	-
F_y	-	9.01×10^8	-
F_z	-	-	1.01×10^8

Table 3.4: Stiffness coefficients K_{xx}, K_{yy} and K_{zz} for the coupled 7013 CD bearings.

Stiffness coefficients for the coupled 7013 CD bearings [N/m]			
Force [N]	1/Displacement [1/m]		
	$1/\delta_x$	$1/\delta_y$	$1/\delta_z$
F_x	9.12×10^8	-	-
F_y	-	9.12×10^8	-
F_z	-	-	4.40×10^7

Before performing the modal simulation to determine the bending modes of the rotor disk with the stiffness values provided by SKF, a sensitivity analysis was carried out in order to verify the impact that potential uncertainties would have on the results. Thus, the setup previously described was used to simulate four different values of radial stiffness:

- $K_{xx} = K_{yy} = 1 \times 10^7$ N/m
- $K_{xx} = K_{yy} = 5 \times 10^7$ N/m
- $K_{xx} = K_{yy} = 1 \times 10^8$ N/m
- $K_{xx} = K_{yy} = 1 \times 10^9$ N/m

The results of these simulations allowed obtaining the undamped critical speed map shown in Figure 3.19, where the nominal rotational speed (black curve) is compared with the critical speeds of both the first mode (BW - red curve) and the second mode (FW - orange curve). Considering the values of radial stiffness provided by SKF ($K_{xx} = K_{yy} \approx 9 \times 10^8$ N/m), the design point can be considered far enough from the critical frequencies to ensure its safe operation.

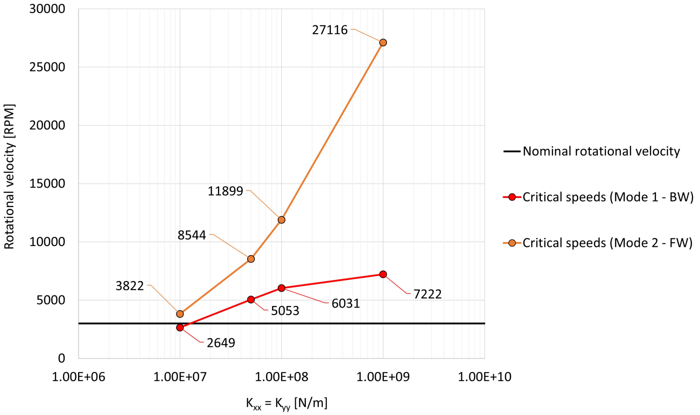

Figure 3.19: Undamped critical speed map of the test rig.

Subsequently, the resulting Campbell diagram obtained by employing the nominal stiffness values reported in Table 3.3 and Table 3.4 has been reported in Figure 3.20. The diagram reports the first eight eigenmodes of the test rig by distinguishing them between those associated with the rotor and those related to the frame. As can be observed and in accordance with the undamped critical speed map seen in Figure 3.19, all the eight critical speeds appear to be located significantly beyond the design point of the test rig. Even the first mode, identified as a backward whirling mode of the rotor, exhibits a critical speed at approximately 6800 RPM which is more than double the nominal design point. The critical speeds of all the other reported modes exceed instead 9000 RPM. Thus, from the results of the modal analysis it can be concluded that the chosen configuration is perfectly suitable to ensure the correct and safe operation of the test rig in the whole expected operational range (0-3000 RPM).

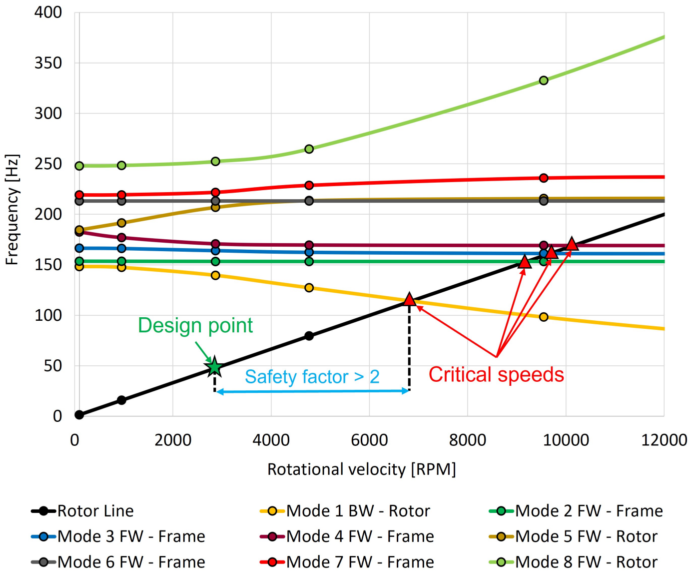

Figure 3.20: Campbell diagram of the test rig [69].

3.5.3 Dynamic harmonic simulations

The dynamic harmonic simulations have been conducted as a precautionary measure since, as shown in Section 3.5.2, all the critical speeds are significantly higher than the design rotational speed and thus no excitations of the eigenmodes are likely to be expected within the whole operating range of the test rig. As shown in Figure 3.21, the harmonic simulations are based on the same setup used for the modal simulations but with the addition of a point mass on the rotor disk that induces an unbalancing effect. The magnitude of the added mass has been calculated with the intent to achieve a balance grade G2.5 which, according to ISO 1940 and considering the weight of the assembly composed by the rotor disk and the cover (approximately 29 kg) and the nominal rotational speed (3000 RPM), corresponds to a maximum allowable imbalance of 245 g*mm.

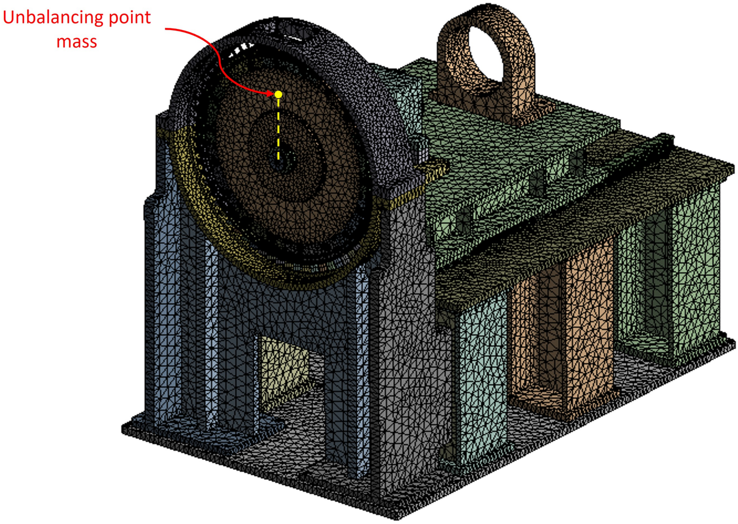

Figure 3.21: Mesh and setup of the dynamic harmonic simulations.

Therefore, the maximum admissible imbalance has been employed to perform the harmonic simulations and the resulting Bode diagram has been reported in Figure 3.22. In particular, three vibration curves are provided, corresponding respectively to the radial vibrations of the bearings (green curve), those of the bearings case (blue curve) and the net values obtained by performing the difference between the two aforementioned ones (yellow curve). As can be observed, extremely low values of radial vibrations, approximately in the order of magnitude of 1×10^{-4} mm, can be found in proximity of the nominal operating region of the test rig (50 Hz). As anticipated by the modal simulations, all the peaks due to the resonances can be found at frequencies higher than 100 Hz and therefore they do not represent a relevant concern for the current application. Finally, additional verifications included simulating imbalance values that are respectively the double and triple of the one calculated according to the ISO standard.

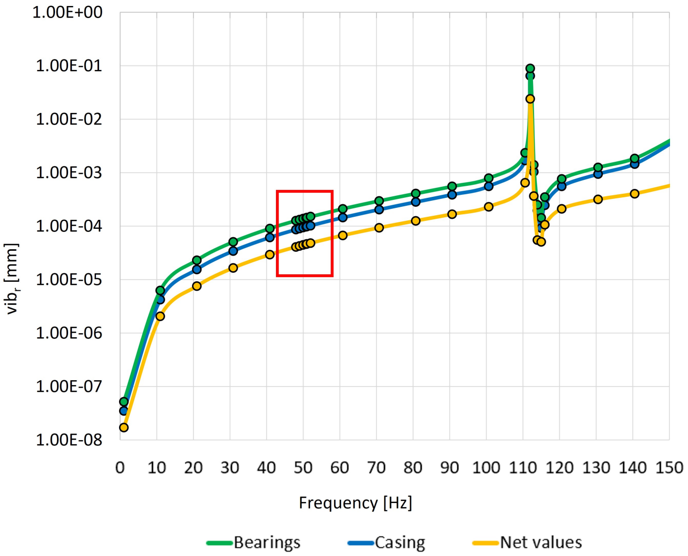

Figure 3.22: Bode diagram of the test rig [69].

The obtained results demonstrated that the system responds in a perfectly linear manner, predicting radial vibration values that are respectively the double and triple of those shown in Figure 3.22. Hence, this minimal level of vibrations, which can be attributed to the significant stiffness of the designed system, does not raise any concerns neither for the control of the actual dimension of the radial gap nor for safety reasons. Consequently, the balance grade G2.5 was considered to be sufficient to ensure a correct and safe operation of the facility. Furthermore, it is reminded here that the presence of any eventual imbalance can be monitored through the use of monoaxial accelerometers placed on the bearings case. Then, if necessary, a correction can be applied by installing balancing grub screws of varying lengths, and thus different weights, into the rotor disk in staggered position with respect to the bolts that anchor the cover, as shown in Figure 3.23.

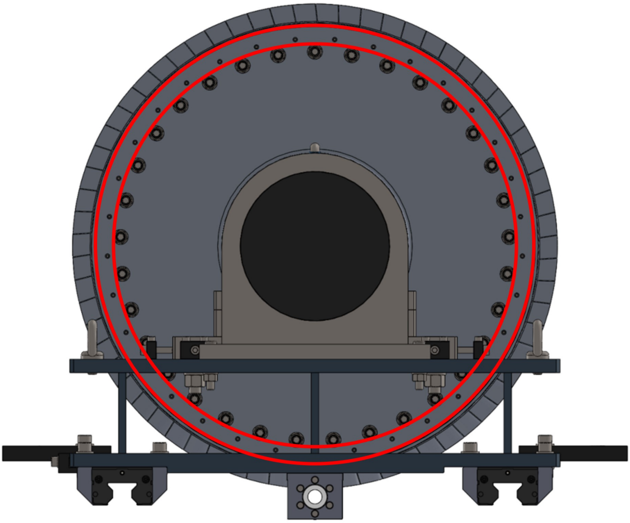

Figure 3.23: Position where the balancing grub screws can be installed to correct any eventual imbalance of the rotor disk.

Chapter 4

Commissioning of the test rig

Contents

4.1 Installation of the test rig

After positioning the test rig inside the test cell, the correct assembly of the facility was verified before proceeding with the connection to the air supply lines, the instrumentation and the commissioning tests. Hence, the flatness of both the rotor and the stator surfaces as well as their mutual parallelism was thoroughly checked. Furthermore, the proper positioning of the rotor disk on the main axis line was inspected in order to ensure the coaxial alignment between the two disks. These measurements allowed to verify that eventual deviations in flatness, parallelism and coaxiality due to either the manufacturing or the assembly procedure fell within the tolerances specified by the design procedure. Additionally, this process allowed verifying that the actual radial gap between the rotor and stator matched the design specifications in order to prevent any potential rubbing between the two components during the tests.

4.1.1 Annulus flow supply line

The annulus mass flow rate is provided to the test rig by the supply line shown in Figure 4.1. A centrifugal blower (1) with a nominal power of 90 kW draws air from inside the laboratory and directs it towards the test section of the facility through a pipeline (2) with a total length of approximately 12 m. Given the mass flow rates involved, the resulting average flow velocity inside the line is approximately 20 m/s. A flow conditioner (3) consisting of a square mesh grid is placed between the two pipe sections (2a and 2b). The purpose of this conditioner is to straighten the flow and eliminate any disturbances that could arise due to the presence of valves and bends upstream. A mass flow meter FCI ST50 (4) is used to monitor the mass flow rate. According to the data-sheet, the presence of the flow conditioner (3) ensures the compliance with the minimum distance from the test section required to achieve satisfactory measurement accuracy. For safety reasons, the test rig (5) is placed inside the test cell while the control panel (6) used to monitor the execution of the tests is positioned outside the test cell.

The author of this work designed the layout of the annulus flow supply line, ensuring its proper integration with the components already present in the laboratory and in accordance with the design requirements of the test rig.

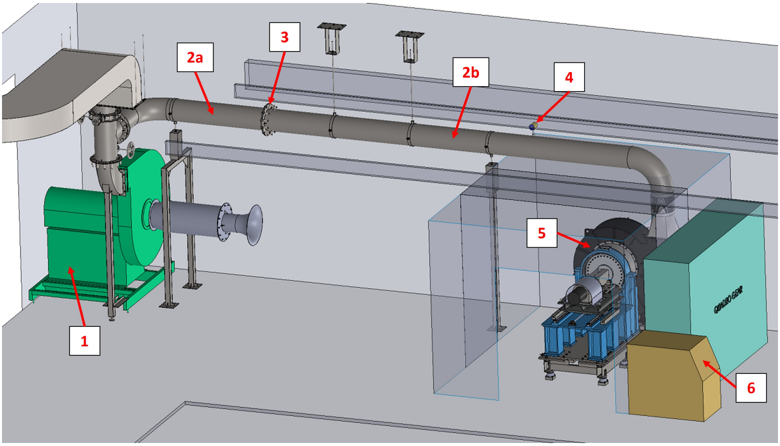

Figure 4.1: General layout of the supply line that provides the annulus mass flow rate to the test rig.

4.1.2 Purge flow supply line

The purge mass flow rate used to seal the wheel-space is provided to the test rig by an additional supply line which is schematically represented in Figure 4.2. A compressed air line was diverted from the compressed air circuit already present in the laboratory to direct the flow towards the purge flow inlet located at the center of the stator disk. Two calibrated orifice plates with a size of either 12.5 or 25 mm can be alternatively employed to measure the mass flow rate, where the choice between the two aims to maximise the measurement accuracy in accordance with the different operating conditions being tested. Furthermore, as will be later explained more in details, the purge flow can be seeded with a small percentage of CO_2 before being injected inside the cavity. This procedure is necessary to perform gas sampling measurements and, consequently, to determine the values of sealing effectiveness on the stator surface. The CO_2 line was derived from the technical gas line of the laboratory by installing a pipe equipped with a throttling valve. The discharge from the test rig occurs directly inside the test cell which is equipped with specific sniffers to prevent an eventual under-oxygenation of the room. Moreover, an extraction fan is used to ensure an adequate recirculation of air.

The author of this work designed the layout of the purge flow supply line, ensuring its proper integration with the components already present in the laboratory and in accordance with the design requirements of the test rig.

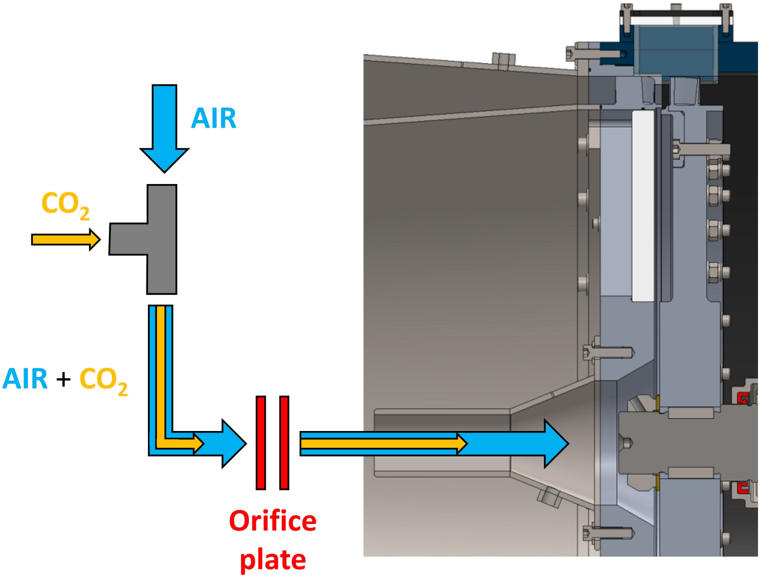

Figure 4.2: General layout of the supply line that provides the purge flow to seal the wheel-space.

4.1.3 Different rim seal configurations

In the course of this work, three distinct rotor side covers were designed and tested in order to evaluate the impact of different geometrical parameters on the resulting effectiveness values. The combination of these three geometries with the one placed on the stator side led to the definition of three single radial rim seal configurations, named M1, M2 and M3 which are characterized by distinct shapes of the rotor side lip and different values of the seal clearance ratio G_c. Since all the investigated configurations are radial rim seals, the value of G_c has been calculated by using Eq. 2.8 where the numerator has been substituted with the value of the radial clearance $s_{c,rad}$. Furthermore, given the possibility to vary the axial position of the rotor disk, different values of axial overlap $s_{overlap}$ were achieved for each of these configurations. In total, the seven different rim seal configurations shown in Figure 4.3 were tested. As can be seen, the letters A, B and C denote the different values of axial spacing S and hence overlap of the rim seals, where configuration A always represents the design distance between the vanes TE and the blades LE. The configuration M1A can be considered the baseline geometry from which all the other rim seals have been derived. As can be noticed, configurations M1 and M2 share the same value of seal clearance ratio but they differ in the design value of axial overlap, whereas M3 features a value of G_c that is 2.4 times greater than that of M1 and M2. In addition, it should be noted that the direction of the external flow is from left to right, from the stator to the rotor.

Additionally, it is important to highlight that the different geometrical parameters reported in Figure 4.3 have been normalized with respect to a reference value indicated by the subscript “ref” in order to protect industrially sensitive data. Similarly, this approach will also be used in subsequent chapters to normalize the obtained results. However, this normalization process does not have any impact on the considerations that can be drawn from the presented results.

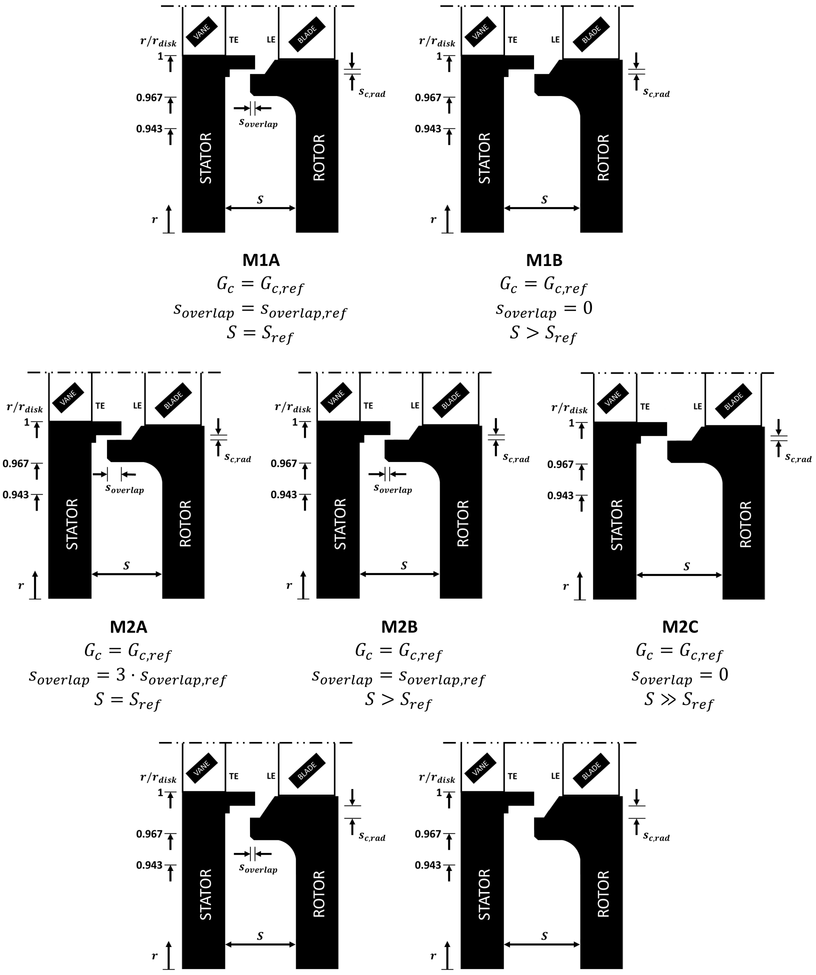

M1A
$G_c = G_{c,ref}$
$s_{overlap} = s_{overlap,ref}$
$S = S_{ref}$

M1B
$G_c = G_{c,ref}$
$s_{overlap} = 0$
$S > S_{ref}$

M2A
$G_c = G_{c,ref}$
$s_{overlap} = 3 \cdot s_{overlap,ref}$
$S = S_{ref}$

M2B
$G_c = G_{c,ref}$
$s_{overlap} = s_{overlap,ref}$
$S > S_{ref}$

M2C
$G_c = G_{c,ref}$
$s_{overlap} = 0$
$S \gg S_{ref}$

M3A
$G_c = 2.4 \cdot G_{c,ref}$
$s_{overlap} = s_{overlap,ref}$
$S = S_{ref}$

M3B
$G_c = 2.4 \cdot G_{c,ref}$
$s_{overlap} = 0$
$S > S_{ref}$

Figure 4.3: Different rim seal configurations investigated in this study.

4.2 Instrumentation of the test rig

The instrumentation of the test rig mainly consists of static and total pressure probes, thermocouples, concentration taps for CO_2 gas sampling, the setup to perform PSP measurements and a concentration probe equipped with an oxygen sensor element. The main instrumentation placed in the test section is indicated in Figure 4.4. However, there are also a large number of measurement points used to monitor the proper execution of the tests that are not shown in the figure. Hence, all the measuring points present in the facility will be described in detail in the following sections.

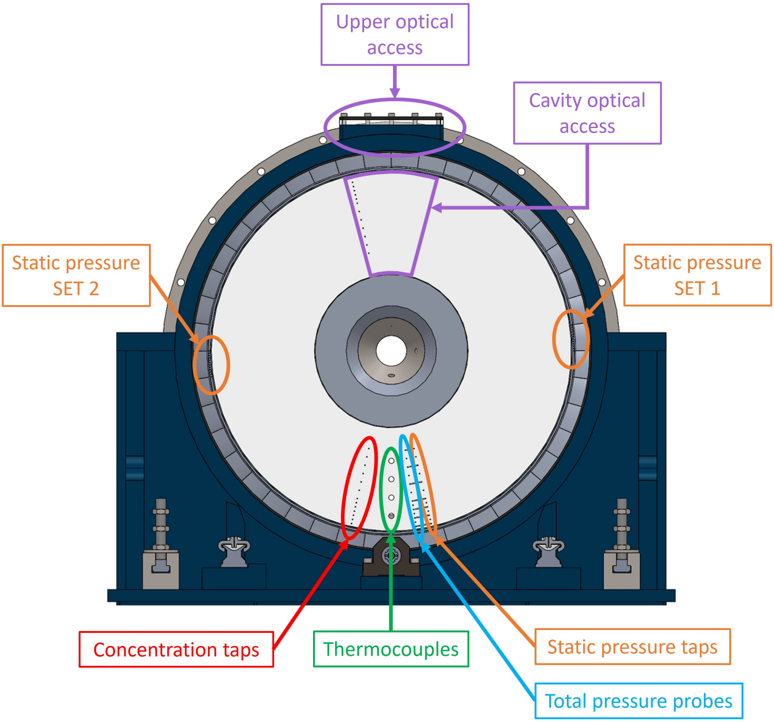

Figure 4.4: Main instrumentation placed in the test section [76].

4.2.1 Static pressure taps

Numerous static pressure taps have been installed at different locations on the test rig. Starting from the main flow inlet, the first static pressure tap is positioned at the beginning of the feeding volute (Figure 4.5a) and it is used to monitor the conditions of the flow coming directly from the blower. Subsequently, four pressure taps are positioned equally spaced in the circumferential direction on the convergent duct at stator inlet (Figure 4.5b). Their purpose is to monitor the circumferential uniformity of the flow entering the test section. Moving forward, there are two sets of twelve pressure taps each placed between the TE of the vanes and the end of the stator platform. These pressure taps were indicated in Figure 4.4 as “SET 1” and “SET 2”. Moreover, one of these two sets is shown in details in Figure 4.5c. The two sets cover two vane pitches which are 180 deg spaced and they can be used to check the flow circumferential uniformity at the entrance of the wheel-space. However, the play a more fundamental role since they are used to measure the pressure coefficient C_p (Eq. 2.16) and, consequently, the non-dimensional pressure difference ΔC_p (Eq. 2.17) that characterize the operating condition of the test rig.

Considering the purge flow, another pressure tap is positioned at the sealant flow inlet to monitor the conditions of the flow entering the wheel-space. Finally, there are thirteen pressure taps arranged radially inside the wheel-space (Figure 4.5d) that can be used to determine the radial distribution of static pressure. These pressure taps can also be seen in the previously reported Figure 4.4.

For each pressure tap, a PVC pipe was used to carry the output signal to a pressure scanner placed inside the test cell. Two different pressure scanners were used to acquire all the pressure measurements. The first pressure scanner has a measurement range of 0-1 PSI (0-7000 Pa) with an uncertainty of 10 Pa (±0.15% FS) while the second one has a measurement range of 0-5 PSI (0-35000 Pa) with an uncertainty of 17 Pa (±0.05% FS) for all the ports except for two which have a measurement range of 0-15 PSI (0-105000 Pa) with an uncertainty of 52 Pa (±0.05% FS).

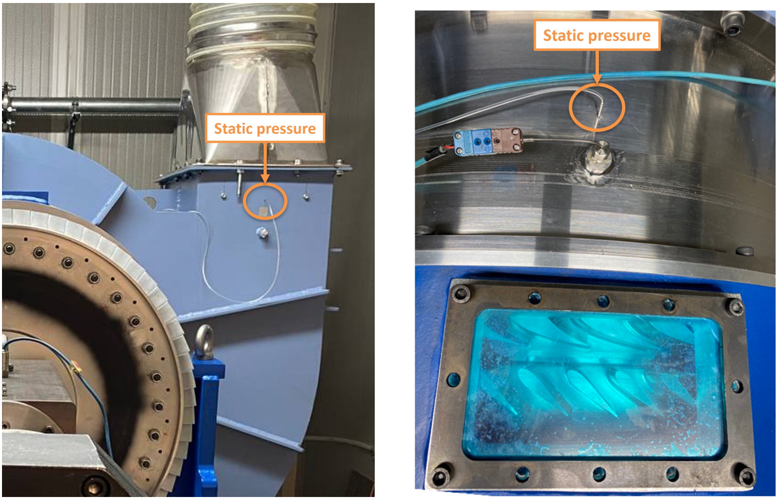

(a) Feeding volute *(b) Stator inlet - Top view*

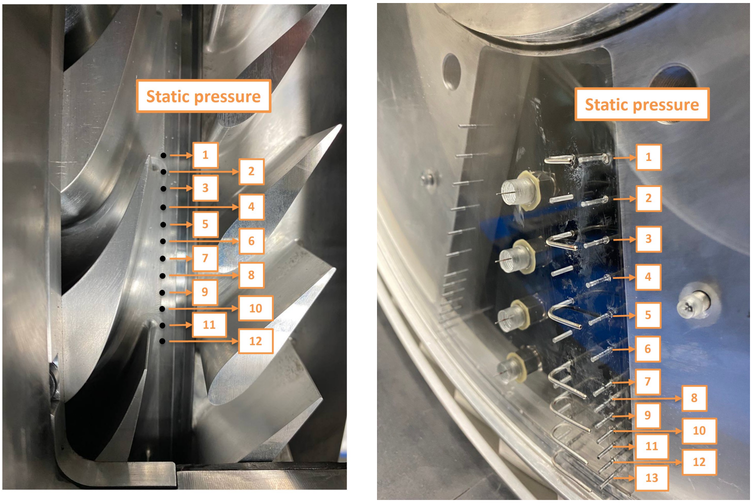

(c) Stator platform - SET 2 *(d) Wheel-space*

Figure 4.5: Static pressure taps installed on the test rig: a) Feeding volute, b) Stator inlet, c) Stator platform and d) Wheel-space.

4.2.2 Total pressure probes

Seven total pressure probes have been installed inside the wheel-space to measure the radial distribution of total pressure. These probes were obtained by properly bending and shaping capillary tubes with a diameter of 1.6 mm which were installed on the stator side of the cavity with the inlet pointing in the circumferential direction (Figure 4.6). They were positioned at $z/S = 0.25$ where z is the axial direction and S is the axial width between stator and rotor, enabling measurements to be conducted outside the stator boundary layer. Moreover, aligning the probe inlets with adjacent static pressure taps enabled swirl ratio calculation, in accordance with the procedure found in similar studies [11, 63].

Each total pressure probe was connected to a PVC pipe used to carry the output signal to a pressure scanner with a measurement range of 0-5 PSI (0-35000 Pa) and an uncertainty of 17 Pa (±0.05% FS). The total pressure probes can also be seen in the previously reported Figure 4.4.

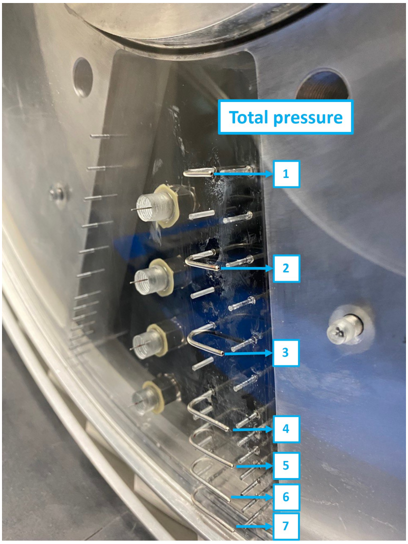

Figure 4.6: Seven total pressure probes installed inside the wheel-space.

4.2.3 Thermocouples

Despite the test rig is operated at cold flow conditions, several thermocouples have been installed to monitor the temperature of the flows during the execution of the tests. The thermocouples were installed at different locations on the test rig by using compression joints and then immersed in the flow by the required value to ensure accurate measurements. Starting from the main flow inlet, the first thermocouple is positioned at the beginning of the feeding volute (Figure 4.7a) and it is used to monitor the conditions of the flow coming directly from the blower. Following that, four thermocouples are positioned equally spaced in the circumferential direction on the convergent duct at stator inlet (Figure 4.7b). Their purpose is to monitor the circumferential uniformity of the flow entering the test section.

Considering the purge flow, another thermocouple is positioned at the sealant flow inlet to monitor the conditions of the flow entering the wheel-space. Finally, there are four thermocouples arranged radially inside the cavity (Figure 4.7c) that can be used to monitor the radial distribution of temperature. These thermocouples can also be seen in the previously reported Figure 4.4.

All the thermocouples were connected to an Agilent data acquisition system placed inside the test cell to read the measured values. T-type thermocouples with an uncertainty of 0.8°C were used for all the measuring points and the temperature inside the test cell was taken as reference temperature (i.e. cold junction temperature). Moreover, thermocouples with a diameter of 1 mm were used for all the measuring points except for the four points arranged radially inside the cavity. Here, thermocouples with a diameter of 0.5 mm were employed to ensure a faster response time in correspondence of the test section.

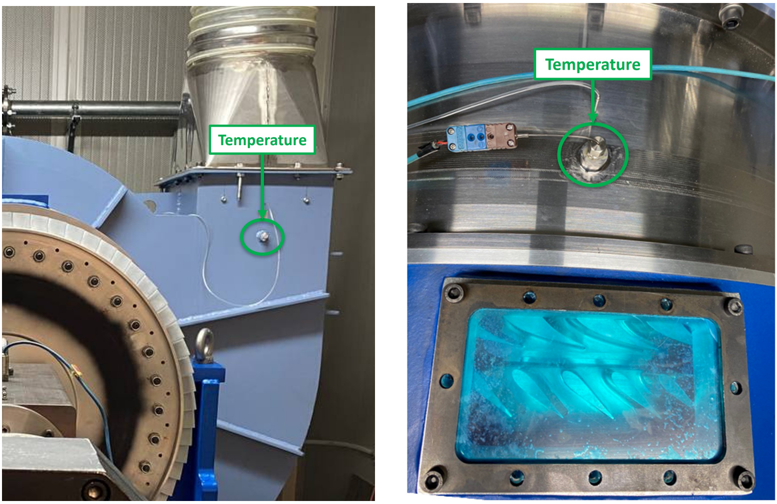

(a) Feeding volute (b) Stator inlet - Top view

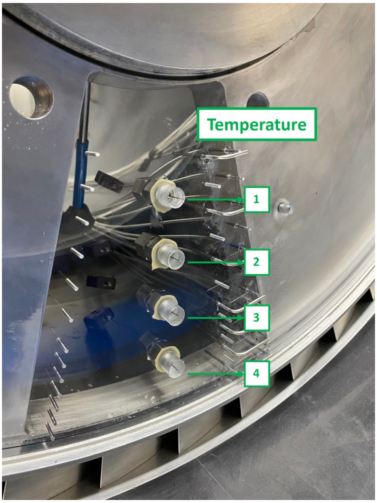

(c) Wheel-space

Figure 4.7: Thermocouples installed on the test rig: a) Feeding volute, b) Stator inlet and c) Wheel-space.

4.2.4 Gas sampling setup

The setup used to perform the CO_2 gas concentration measurements is shown in Figure 4.8 where the position of the thirteen radial concentration taps has been highlighted in order to better visualize where the sampling measurements are performed. These concentration taps can also be seen in the previously reported Figure 4.4. From the concentration taps, the acquisition setup allows performing simultaneous gas sampling measurements at two different radial positions by employing two distributors equipped with different valves. An additional line is reserved to the continuous acquisition of the concentration of CO_2 in the purge flow supply line. The air is extracted from the cavity through the use of three

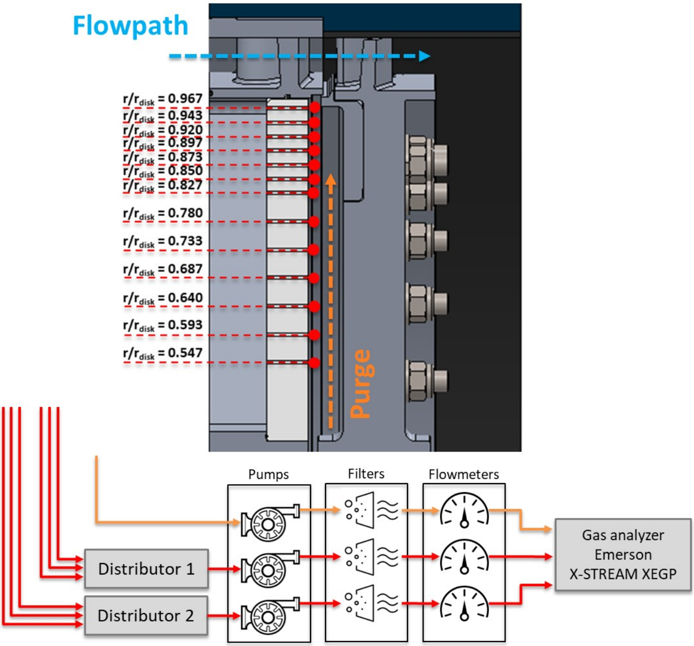

Figure 4.8: Setup used to perform the CO_2 gas concentration measurements [76].

small pumps since the pressure inside the wheel-space was observed to be insufficient to overcome the pressure losses associated to the use of the long ducts necessary to connect the concentration taps to the gas analyser. Then, three air filters are placed at the exit of the pumps in order to avoid clogging the gas analyser with the eventual presence of small particles. Lastly, three flow-meters are used to measure the quantity of air extracted from the cavity and directed towards the continuous infra-red gas analyser (Emerson X-STREAM XEGP) whose optimal working range is between 0.2 and 1.5 l/min. Finally, the effectiveness values could be derived from the concentration measurements by employing the standard expression reported in Eq. 2.9.

4.2.5 PSP setup

Pressure Sensitive Paint is a non-intrusive optical diagnostic technique which is based on the use of organic molecules sensitive to the concentration of oxygen in the surrounding environment. These molecules, incorporated into the paint through the use of a polymeric binder permeable to oxygen, are elevated from their ground electronic state to a more energetic state through the absorption of a photon provided by an incident light of a known frequency. Although after a certain amount of time these molecules tend to return to their initial state through a radiative process, there is also another non-radiative mechanism, known as oxygen quenching, that allows them to return to their initial state. This mechanism concerns the interaction with the oxygen molecules present in the surrounding environment and it is the relevant pathway for the exploitation of the PSP technique. In this case, the intensity of the light emitted by the paint is inversely proportional to the partial pressure of oxygen and therefore to its concentration, a characteristic that makes PSP well-suited to perform surface effectiveness measurements [77, 78].

Hence, the PSP setup shown in Figure 4.9 was developed with the intent to acquire 2D effectiveness maps on both the stator and the rotor side of the cavity by exploiting the optical access provided by the stator cover made of transparent PMMA (Polymethylmethacrylate). To perform measurements on the rotor side, a thin layer of PSP (single component UniFib®) was directly applied on a circumferential sector of the rotor disk. On the contrary, to perform measurements on the stator side, a thin layer of glass was first applied to the PMMA cover onto which the same paint formulation used for the rotor was subsequently applied. In this case, the use of an intermediate surface was considered to be necessary in order to prevent an eventual contamination of the PMMA surface which could influence the resulting effectiveness values. Therefore, the stator cover was alternatively considered both as a transparent optical access for rotor measurements and as a target surface for stator measurements. In this regard, it is interesting to notice that for measurements on the stator side, the emitted light is captured from the "backside" rather than looking directly at the painted surface. As far as the author's knowledge on PSP

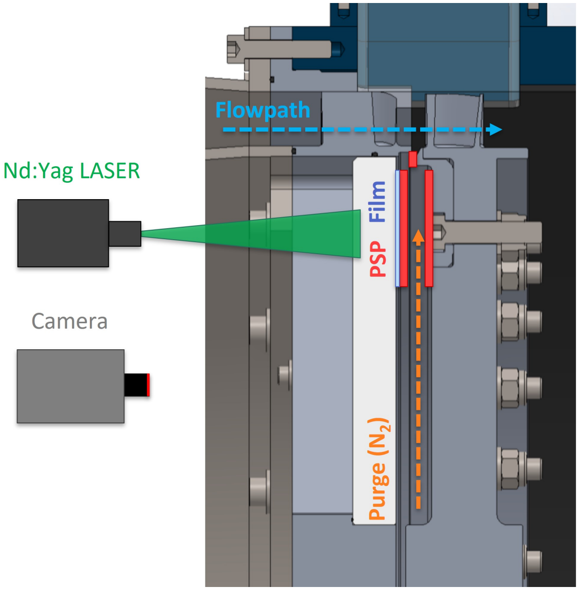

Figure 4.9: Setup used to perform the PSP measurements on both the stator and the rotor side of the cavity [79].

measurements is concerned, the effectiveness measurements performed in this study represent the first instance in the open literature where a “backside” arrangement is used. Thus, demonstrating the feasibility of this unconventional approach will also prove the potential of this technique to be used in test rigs characterized by limited optical access on the front side. Furthermore, an Nd:YAG LASER commonly employed for PIV applications was used to illuminate the PSP with high-energy density bursts at a wavelength of 532 nm. These bursts were converted into laser sheets through the use of a series of cylindrical lenses, carefully chosen to uniformly illuminate the painted region. In the case of measurements conducted on the rotor side, these bursts were also synchronized with the passage of the painted sector in front of the optical access by using a laser trigger. Subsequently, the intensity of the light emitted from the paint was captured by using a high-speed camera (Phantom Speed Sense M340) equipped with a CMOS sensor with an aspect ratio of 4:3 and a resolution of 2560 × 1600 pixels. The camera also featured a f150 mm lens to appropriately focus the region of interest and a 610 nm red filter to avoid capturing the exciting light of the laser. Moreover, the laser pulse and the camera shutter were synchronized by using a timer box, which allowed an accurate control of the timing of both the instruments. The acquisition of the images was performed by setting an exposure time of 0.05 ms in order to prevent obtaining blurred images due to the rotation of the rotor. Otherwise, the acquired images would have required a specific and complex post-processing based on deconvolution algorithms, as demonstrated by Gregory et al. [80].

Subsequently, a value of PSP effectiveness (ε_{PSP}) based on the measured partial pressure of oxygen (p_{O_2}) and on the molecular weight (MW) of the gases was defined [81, 82]:

$$\varepsilon_{PSP} = 1 - \frac{1}{\left[1 + \left(\frac{p_{O_2,air}/p_{O_2,off}}{p_{O_2,fg}/p_{O_2,off}} - 1\right) \cdot \frac{MW_{fg}}{MW_{air}}\right]} \tag{4.1}$$

where the subscript “off” designates images acquired without the presence of purge flow in the cavity, which were used to account for potential irregularities in paint distribution or illumination. The subscripts "air" and "fg" instead respectively refer to images obtained under the desired flow conditions but using either air or a foreign oxygen-free gas, such as N_2. It is important to note that all the intensities measured in the previously mentioned cases have been adjusted by using values obtained from a "dark" test, where the laser is turned off. This allowed taking into account the background noise of the camera. For more detailed information on the successful application of the PSP technique to the study of mixing flows, refer to Caciolli et al. [83].

4.2.6 Concentration probe

In order to connect the PSP effectiveness measurements carried out separately on the stator and rotor surfaces of the wheel-space, an innovative probe was also used to directly measure the level of mixing between the sealing flow and the external annulus flow. This probe has been developed at the University of Florence [84] and it is equipped with a fibre-optic oxygen sensor element (FOSPOR-AL 300) which is based on the use of a ruthenium compound in a sol-gel film matrix. Moreover, a K-type thermocouple with a diameter of 0.5 mm and a pressure port obtained by appropriately bending and shaping a capillary tube are used to correct the concentration measurement in the case of highly 3D flows characterized by significant pressure and velocity gradients. These three sensors have been inserted inside a 3D printed Kiel-like shield that creates a "dead volume" inside which the flow velocity is negligible. This allows ensuring that the measured values of pressure and temperature are the same as those seen by the oxygen sensor element. The external diameter of the shield and therefore its resolution is 3.7 mm while the probe stem, necessary to allow the installation of the probe on any support, has a diameter of 2.5 mm. These values have been chosen as small as possible in order to limit the intrusiveness of the probe which thus results to be comparable to that of other more conventional measurement systems. The model of the probe head is shown in Figure 4.10 where the main features just described have also been highlighted.

The operating principle on which this oxygen sensor element is based is the fluorescence behaviour which is essentially the same previously described for the PSP. Hence, a pulsed blue light with a wavelength of about 475 nm is provided by the optical fiber and used to excite the sol-gel which then emits light at a wavelength of about 600 nm corresponding to the red portion of the spectrum. Part of this energy is transferred to the oxygen molecules through the oxygen quenching mechanism while the remaining part is collected and analysed by the probe in order to determine the partial pressure of oxygen and therefore its concentration. The tests were conducted by inserting the probe inside the cavity from the stator side at a radial position of $r/r_{disk} = 0.80$ and then traversing it in the direction of the rotor surface in order to obtain the effectiveness profile in the axial direction. Moreover, pure N_2 was used as sealing flow in order to determine the level of mixing between the purge and the annulus flow which was instead constituted by ambient air. Then, the sealing effectiveness was determined by using the expression reported in Eq. 2.9 which was also used for the gas sampling measurements.

Since the complete description of the design, validation and capabilities of this probe is beyond the scope of this thesis, additional details can be found in Babazzi et al. [84, 85].

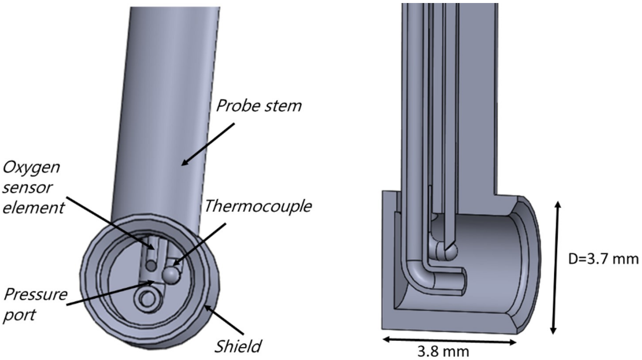

Figure 4.10: Model of the concentration probe head [84].

4.2.7 Measurement uncertainty

In this study, numerous physical quantities of interest are derived through the direct measurement of other variables. For this reason, it is necessary to determine the resulting uncertainty by using the uncertainty propagation theory developed by Kline and McClintock [86]. This theory states that a generic resulting quantity R, which is a function of other variables, can be written as:

$$R = f(v_1, v_2, ..., v_n) \tag{4.2}$$

where $v_1, v_2, ..., v_n$ are the directly measured physical quantities with their respective uncertainties $w_1, w_2, ..., w_n$. The uncertainty associated with the generic quantity R can then be calculated by using the following expression:

$$w_R = \sqrt{\left(\frac{\partial f}{\partial v_1} \cdot w_1\right)^2 + \left(\frac{\partial f}{\partial v_2} \cdot w_2\right)^2 + ... + \left(\frac{\partial f}{\partial v_n} \cdot w_n\right)^2} \tag{4.3}$$

Therefore, the application of Eq. 4.3 to the main parameters used in this study allowed the determination of the resulting uncertainty values reported in Table 4.1 (level of confidence ±95%).

Table 4.1: Measurement uncertainties of the main parameters used in this study.

Measurement uncertainties	
Re_w	2%
Re_Φ	0.7%
ΔC_p	2.2%
β	1-4%
Φ	1.6%
ε_c	2.8%
ε_{PSP}	2-3%

4.3 Commissioning results

Before starting the actual experimental campaign, a series of commissioning tests were conducted to ensure the correct and safe operation of the experimental facility. In particular, the vibrations in both axial and radial directions were monitored by using two accelerometers positioned on the bearings case. The vibration tests were conducted with a gradual ramp-up to a rotational speed of 3000 RPM, followed by a subsequent ramp-down where the correct shut-down of the test rig was also verified. The measured vibration values were assessed in accordance with the ISO10816-5:2001 standard, both in terms of acceleration, which is the parameter used to monitor the health condition of the bearings, and in terms of velocity, the actual parameter used to determine the operational acceptability. The recorded vibrations consistently remained well below the threshold value indicating the safe operation of the test rig and therefore no further details regarding the vibrations will be provided here. Instead, this section focuses on more crucial aspects such as the determination of the allowable operating range in accordance with the constraints of the facility, the verification of the circumferential uniformity of the annulus flow and the quantification of the impact of the quantity of purge air extracted from the cavity on the effectiveness measurements.

4.3.1 Operating range of the facility

One of the first important results of the commissioning phase concerned the verification that the obtained results are independent of the rotational velocity. This observation derives from the research conducted by Sangan et al. [8] who suggested that hot gas ingestion experiments are characterized by a consistent linear relationship between $\Delta C_p^{0.5}$ and the flow coefficient C_f, regardless of the employed value of Ω. This behaviour was confirmed also for the present test rig by conducting experiments at three different values of Ω (1000, 2000 and 3000 RPM) while adjusting the value of C_f by varying the mass flow rate in the annulus. The results reported in Figure 4.11 demonstrate that the measurements performed at

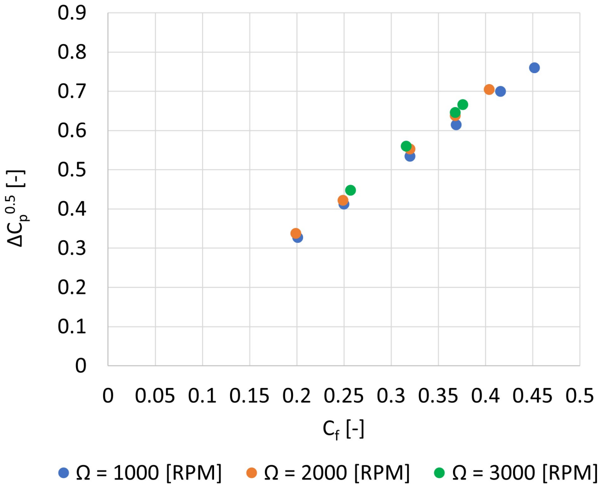

Figure 4.11: Linear variation of $\Delta C_p^{0.5}$ *with* C_f *for three different values of* Ω *(1000, 2000 and 3000 RPM) [76].*

different rotational velocities all lie quite satisfactorily in the same line, thus confirming the independence of the measurements from the rotational velocity. Hence, this observation implies that the experiments can be conducted by selecting specific values of C_f or ΔC_p than can be achieved through different combinations of rotational velocity and flow path mass flow rate without significantly affecting the results. Furthermore, this observation led to the definition of the operational map shown in Figure 4.12 which outlines the possible operating points of the current test rig. As can be noticed, the regions where the experiments cannot be conducted are marked with distinct colors. In particular, the red regions correspond to torque values beyond the operational limits of the torquemeter (0-20 Nm), the yellow region corresponds to values of feeding pressure that cannot be sustained by the blower for long periods of time and the blue region corresponds to rotational velocities greater than 3000 RPM, the maximum speed at which the rotor was verified. By analysing the data points reported on the map, it becomes evident that opting for a velocity of 3000 RPM is not practical due to significant limitations on the allowable C_f range imposed by design and facility constraints. On the contrary, a velocity of 1000 RPM allows the investigation of a much broader range of C_f but at the expense of reduced accuracy. This is due to the fact that the measured points are very close to each other with minimal differences in terms of $\Delta C_p^{0.5}$. Consequently, a rotational velocity of 2000 RPM was identified as the optimal compromise between the allowable range of C_f and the measurement accuracy.

Subsequently, a series of measurements at $C_f = 0.32$ and $\Omega = 2000$ RPM were conducted for different values of Φ to assess the extent of the "spoiling effect" described by Sangan et al. [8]. As previously shown in Figure 2.36, this effect involves a reduction in ΔC_p as Φ increases due to the interaction between the external annulus flow and the egress flow. Although this reduction is typically limited, all the results presented in this study refer to the value of ΔC_p obtained for the case of $\Phi = 0$.

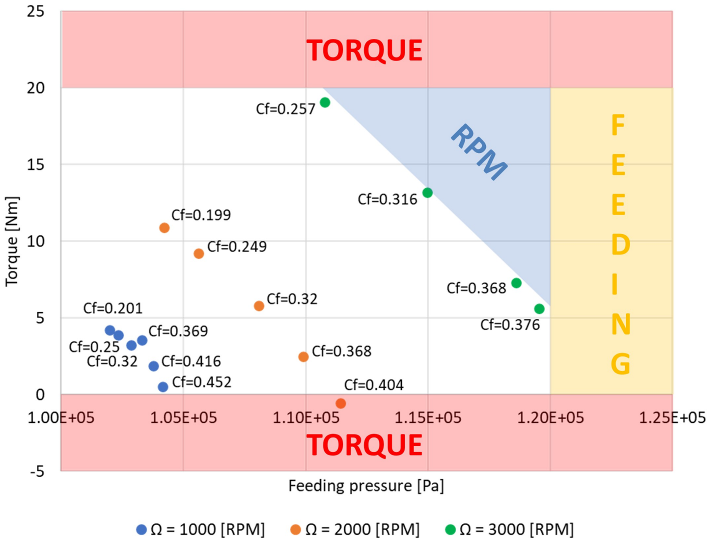

Figure 4.12: Operational map of the current test rig [76].

4.3.2 Circumferential flow uniformity

The circumferential uniformity of the annulus flow at stator exit, thus in correspondence of the rim seal entrance, is a critical factor that required to be examined by using the two sets of static pressure taps positioned after the TE of the vanes that are shown in Figure 4.4. As already mentioned, the two sets are positioned 180 deg apart and they have been tagged as "SET 1" and "SET 2". Thus, the circumferential uniformity of the flow was assessed by comparing the $C_p - \theta$ profiles measured at design conditions and in total absence of purge flow, where θ represents the non-dimensional vane pitch. As shown in Figure 4.13, the comparison revealed a minimal difference between the two profiles, indicating that the flow in the rim seal region is reasonably uniform in the circumferential direction, thus ensuring accurate measurements.

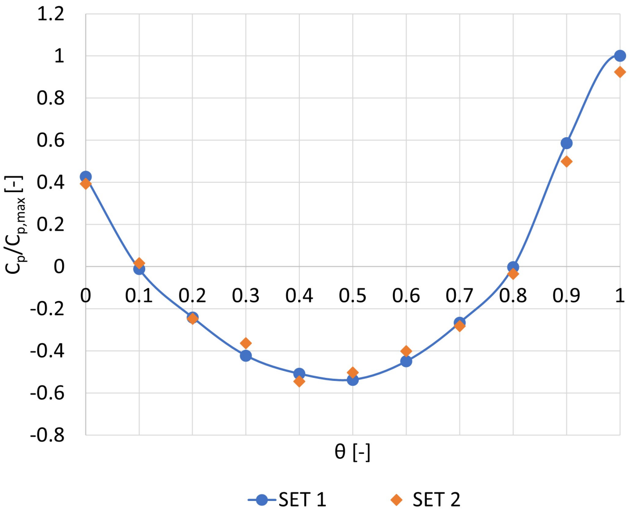

Figure 4.13: Comparison between the $C_p - \theta$ profiles measured with "SET 1" and "SET 2" [76].

4.3.3 Radial pressure profiles

Several radial profiles of static and total pressure were measured inside the wheel-space by respectively using the pressure taps and the total pressure probes that are shown in Figure 4.4. The measurements were performed at different values of Φ and the obtained results are reported in Figure 4.14. As can be noticed, the measurements of static pressure (Figure 4.14a) and total pressure (Figure 4.14b) were then combined together to obtain the radial distribution of swirl ratio (Figure 4.14c) by using the following expression:

$$\beta = \frac{\sqrt{2 \cdot \frac{p_{tot} - p_s}{\rho}}}{\Omega \cdot r} \tag{4.4}$$

which was directly derived from the previously reported Eq. 2.2. According to literature, the ingestion of highly swirled flow from the annulus leads to an increase in β which explains the gradual rise in swirl at increasing values of radius (i.e. close to the rim seal entrance). However, an increase in Φ results in a reduced quantity of ingress which, in turn, explains the progressive decrease in β at increasing values of purge flow. In addition, it is worth to notice that the profiles of $C_{p,tot}$ and, consequently, β tend to deviate backward at higher radii for the highest values of Φ. This phenomenon could be linked to the pumping effect of the rotor which causes a significant amount of air to rise towards the rim seal, hence generating complex flow fields in correspondence of the last probes.

4.3.4 Gas analyser flow rate

To ensure the consistency of the effectiveness measurements, a test was conducted to examine whether the volume of air extracted from the cavity and directed towards the gas analyser affected the results. According to the datasheet of the gas analyser, the measurement accuracy is optimal within a flow rate range of 0.2-1.5 l/min. Therefore, two radial profiles of effectiveness were obtained within the cavity by using all the radial concentration taps shown in Figure 4.8. The two profiles were obtained

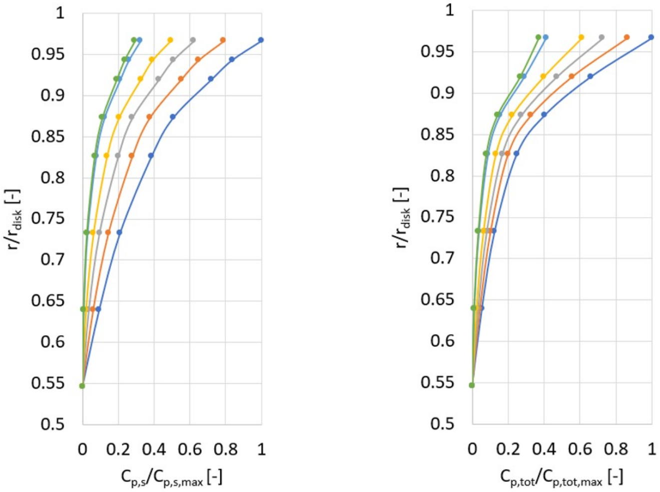

(a) Static pressure

(b) Total pressure

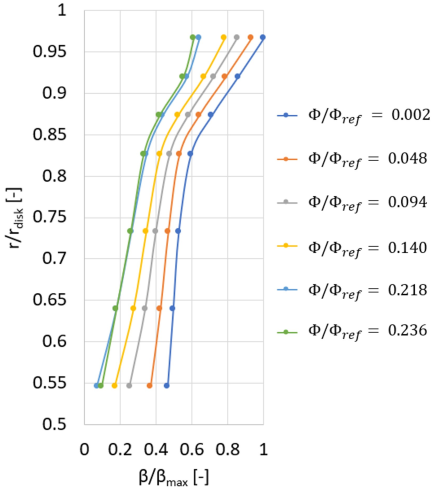

(c) Swirl ratio

Figure 4.14: Radial profiles of (a) Static pressure, (b) Total pressure and (c) Swirl ratio [76]. © 2024 Baker Hughes Company - All rights reserved

by extracting a mass flow rate of either 1.25 l/min or 0.5 l/min. As shown in Figure 4.15, the difference between the two radial profiles is negligible. This indicates that the effectiveness measurements are highly repeatable and that the intrusiveness of the gas sampling technique, in which air is extracted from the stator boundary layer, appears to be minimal within the optimal range of the employed gas analyser.

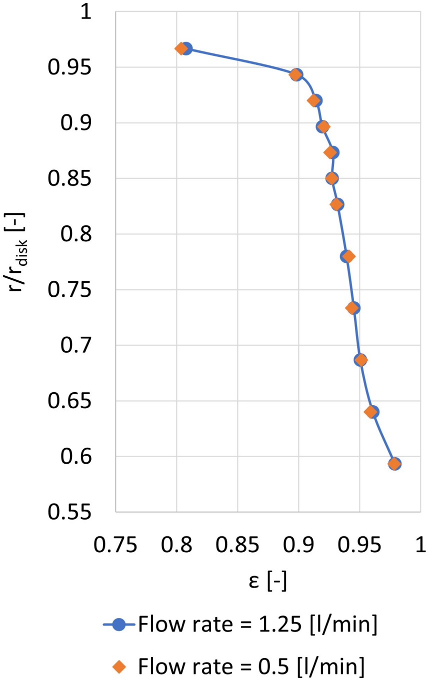

Figure 4.15: Radial profiles of ε_c obtained at $\Phi/\Phi_{ref} = 0.308$ for two different values of gas analyzer flow rate [76]. © 2024 Baker Hughes Company - All rights reserved

4.3.5 Effectiveness measurements

Multiple effectiveness measurements were performed on the baseline rim seal configuration (M1A) by applying the standard CO_2 gas sampling technique in order to assess its accuracy in the determination of $\Phi - \varepsilon_c$ curves. The tests were conducted at $C_f = 0.32$ (EI design condition) and at different rotational velocities (1000 and 2000 RPM) and the concentration of the gas was recorded at two different radial positions, $r/r_{disk} = 0.943$ and $r/r_{disk} = 0.967$, which correspond to the two outermost taps available in the current test rig. Then, the measured concentration values were converted into effectiveness values by applying Eq. 2.9. As can be noticed from the results reported in Figure 4.16, the obtained $\Phi - \varepsilon_c$ curves further confirm the independence of the results from the rotational speed and thus from Re_Φ. These results, which are reported in this section only to

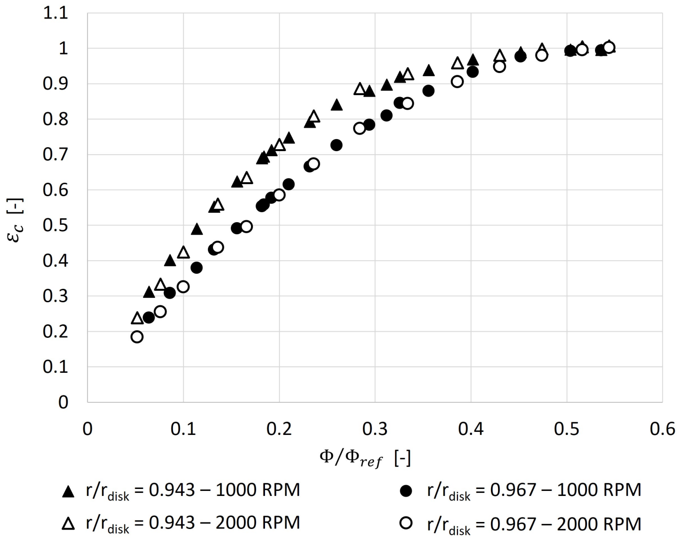

Figure 4.16: Comparison between $\Phi - \varepsilon_c$ curves obtained at 1000 and 2000 RPM and at $r/r_{disk} = 0.943$ and $r/r_{disk} = 0.967$ at $C_f = 0.32$ (EI design condition) [76]. © 2024 Baker Hughes Company - All rights reserved

highlight the capabilities of the gas sampling technique, will be discussed in greater detail in the next chapter where the complete characterization of the sealing performance of the M1A baseline configuration will be reported and discussed. Furthermore, the performance of M1A will be compared with that of all the other configurations described in Figure 4.3 in order to understand the impact of different geometric parameters on the sealing performance of rim seals.

Chapter 5

Characterization of the sealing performance of different rim seals

Contents

5.1 Sealing performance results overview

The intent of this chapter is to report and discuss the experimental results obtained through the use of the gas sampling setup described in Figure 4.8, starting from the complete characterization of the M1A baseline configuration. Hence, the sealing performance of the rim seal will be characterised first at design conditions both in terms of $\Phi - \varepsilon_c$ curves and radial profiles. In particular, attention will be directed towards the significant reduction in effectiveness recorded at higher radii which will be attributed to the ingestion of air from the external annulus flow. Then, several $\Phi - \varepsilon_c$ curves obtained for different values of C_f will be compared in order to investigate the different sealing performance of the rim seal between design and off-design conditions. This will highlight that a monotonic increase in C_f $(= \Delta C_p)$ does not always correspond to a monotonic decrease in ε_c, possibly attributing this phenomenon to rotational and unsteady effects but also to the potential effect of the LE of the blades.

Subsequently, the second part of the chapter will be dedicated to the study of the other six rim seal configurations shown in Figure 4.3. By comparing the results obtained for these configurations with those previously described for the M1A configuration, it will be possible to determine the impact of different geometric parameters on the sealing performance of the rim seals. In particular, the study will focus on assessing the influence of different values of axial overlap $s_{overlap}$, different distances between the vanes TE and the blades LE (hence different values of the axial width between stator and rotor S) and different values of radial gap $s_{c,rad}$ (hence different values of the seal clearance ratio G_c).

5.2 Complete characterization of the baseline configuration

The detailed sketch of the M1A baseline configuration, which will be investigated in the first part of this chapter, is presented in Figure 5.1. Here, the position of the vanes and blades has been indicated in order to clearly visualize the distance between the TE and the LE in relation to the characteristic dimensions of the investigated overlapped radial rim seal. Additionally, Figure 5.1 includes the radial positions of the two outermost concentration taps available in the current test rig, $r/r_{disk} = 0.943$ and $r/r_{disk} = 0.967$. These concentration taps will be used to conduct multiple gas sampling measurements, allowing the comparison of the behaviour of $\Phi - \varepsilon_c$ curves at both design and off-design conditions.

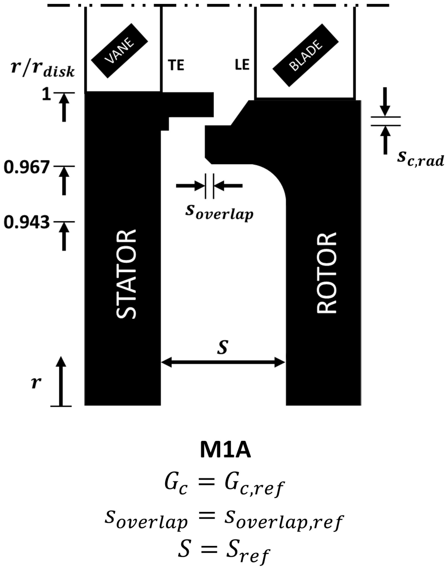

Figure 5.1: Sketch of the M1A baseline configuration.

5.2.1 Results at design conditions

The results of the tests conducted at $C_f = 0.32$ (EI design condition) by applying the standard CO_2 gas sampling technique to the M1A baseline configuration are presented in Figure 5.2. As mentioned earlier, the effectiveness values were simultaneously recorded at two different radial positions, $r/r_{disk} = 0.943$ (triangles) and $r/r_{disk} = 0.967$ (circles). In addition, the experimental data points have been fitted by using the Orifice Model equations derived by Owen [9, 14] and rearranged by Sangan et al. [8] into the explicit EI effectiveness Eq. 2.28. As can be noticed, the resulting curves obtained at both $r/r_{disk} = 0.943$ (dashed line) and $r/r_{disk} = 0.967$ (continuous line) appear to be in excellent agreement with the measured data. In general, the shape of the obtained curves appear to be consistent with the trends found in literature, as

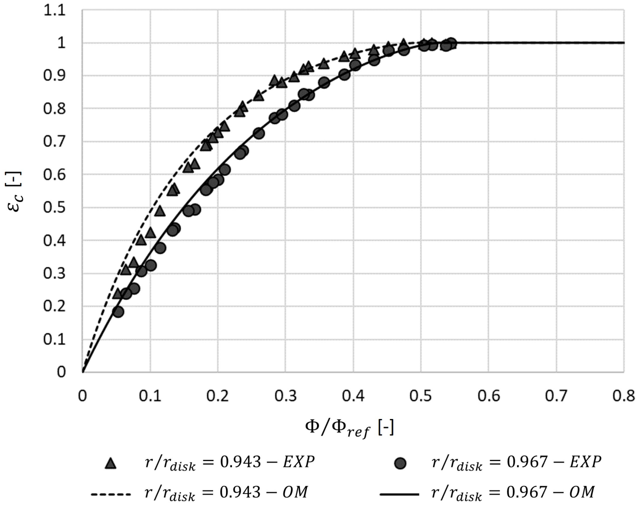

Figure 5.2: Comparison between $\Phi - \varepsilon_c$ curves obtained at $r/r_{disk} = 0.943$ and $r/r_{disk} = 0.967$ at $C_f = 0.32$ (EI design condition) for the M1A baseline configuration. © 2024 Baker Hughes Company - All rights reserved

for example those obtained by Johnson et al. [57] (see Figure 2.33) and those obtained by Sangan et al. [15] (see Figure 2.38). Moreover, the asymptotic behaviour of the curves that was first described by Graber et al. [31], in which 80% of the effectiveness is achieved by injecting a purge flow rate equal to half of what is required for complete sealing (Φ_{min}) while the remaining 20% is achieved by injecting the second half, appears to be confirmed by the experimental curves reported in Figure 5.2. This behaviour remarks that achieving higher levels of protection becomes progressively more expensive and explains why it might often be better to tolerate a reasonable level of ingestion rather than completely prevent it. Moreover, an important aspect to take into consideration regards the fact that the effectiveness values measured at higher radius ($r/r_{disk} = 0.967$) are lower than those obtained at lower radius ($r/r_{disk} = 0.943$). This implies that the effectiveness on the stator side is not radially constant, in particular close to the rim seal entrance.

Consequently, the radial variation of effectiveness on the stator surface has been further investigated by conducting dedicated tests to obtain the radial profiles of ε_c reported in Figure 5.3. These tests were again carried out at $C_f = 0.32$ (EI design condition) and the following three values of Φ/Φ_{ref} were selected:

- $\Phi/\Phi_{ref} = 0.162 \rightarrow \varepsilon_c \approx 0.50$
- $\Phi/\Phi_{ref} = 0.228 \rightarrow \varepsilon_c \approx 0.65$
- $\Phi/\Phi_{ref} = 0.300 \rightarrow \varepsilon_c \approx 0.80$

These values of Φ/Φ_{ref} were chosen in order to obtain the corresponding values of ε_c at higher radius ($r/r_{disk} = 0.967$), thus allowing the comparison of the radial variation of effectiveness under different sealing conditions. As can be noticed, for each tested value of Φ/Φ_{ref}, the radial effectiveness remains relatively constant up to $r/r_{disk} \approx 0.90$. However, the three probes located at higher radii record a great decrease in effectiveness which can be attributed to the ingestion of air from the external annulus flow. The reduction in effectiveness between $r/r_{disk} = 0.90$ and

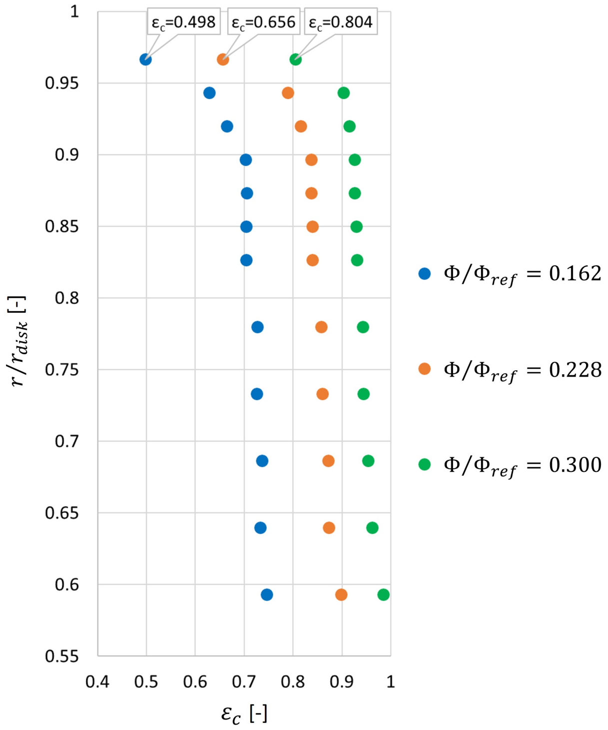

Figure 5.3: Comparison between radial profiles of ε_c obtained for three values of Φ/Φ_{ref} at $C_f = 0.32$ (EI design condition) for the M1A baseline configuration. © 2024 Baker Hughes Company - All rights reserved

$r/r_{disk} = 0.967$ is significant, with variations of 34%, 24% and 14% respectively for the three increasing values of Φ/Φ_{ref}. As expected, this effect is more evident at lower values of sealing flow supplied to the system due to the resulting lower pressurization of the wheel-space which leads to increased ingestion of air. Hence, the obtained radial profiles confirm that the effectiveness exhibits variations along the radial direction and therefore it does not appear to be perfectly constant, as found for example by Sangan [11]. However, this trend has been recently documented in other studies, such as in Robak et al. [87], Horwood et al. [88] and Roy et al. [89] and it has been attributed to the impingement of the rotor boundary layer on the stator surface. This would imply the presence of an expanded mixing region where the ingested flow and the purge flow pumped through the rotor boundary layer interact to a greater extent.

5.2.2 Results at off-design conditions

After characterizing the M1A baseline configuration under design conditions, several $\Phi - \varepsilon_c$ curves were obtained for different values of C_f, thus allowing the comparison of the sealing performance of the rim seal between design and off-design conditions. The resulting curves obtained for both the investigated radial positions, $r/r_{disk} = 0.943$ (triangles) and $r/r_{disk} = 0.967$ (circles), are respectively reported in Figure 5.4a and Figure 5.4b. As can be observed, the test matrix used to conduct the present study includes seven different values of C_f. The design condition has been highlighted in yellow in order to distinguish it from the off-design conditions, which are instead indicated in blue for $C_f < C_{f,design}$ and in green for $C_f > C_{f,design}$. Furthermore, darker shades of blue/green correspond to C_f values that progressively deviate further from the design conditions. A detailed analysis of the obtained $\Phi - \varepsilon_c$ curves indicates that an increment in C_f generally results in lower values of ε_c for the same value of Φ/Φ_{ref}. This behaviour is in accordance with Figure 4.11, where an increase in C_f corresponds to a linear increase in ΔC_p, the driving force for ingress in the EI regime. However, this behaviour is not consistently true across the entire investigated range of C_f. In fact, a certain degree of overlap between the curves can be identified in the range $C_f = 0.32 - 0.35$ for both the investigated radial positions.

Given this rather unexpected effectiveness trend, additional dedicated tests were conducted to determine whether this non-monotonic behaviour was indeed a distinctive characteristic of the current rim seal. The additional tests were performed by gradually varying the value of C_f (and consequently of ΔC_p) while keeping the value of Φ/Φ_{ref} constant. The resulting $C_f - \varepsilon_c$ curves are reported in Figure 5.5 for both $r/r_{disk} = 0.943$

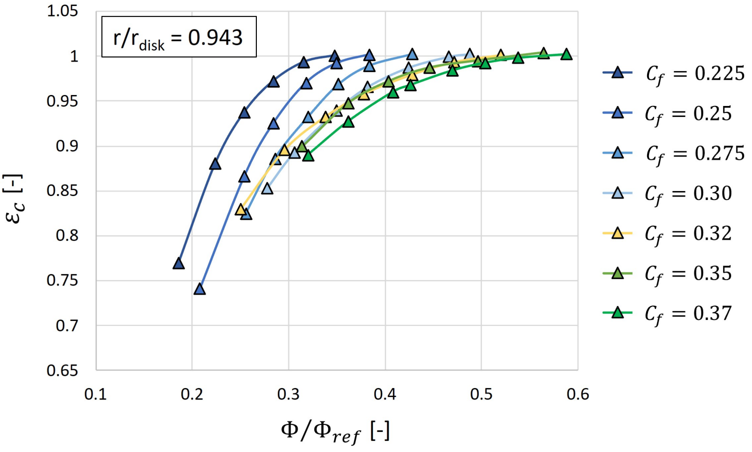

(a) M1A - $r/r_{disk} = 0.943$

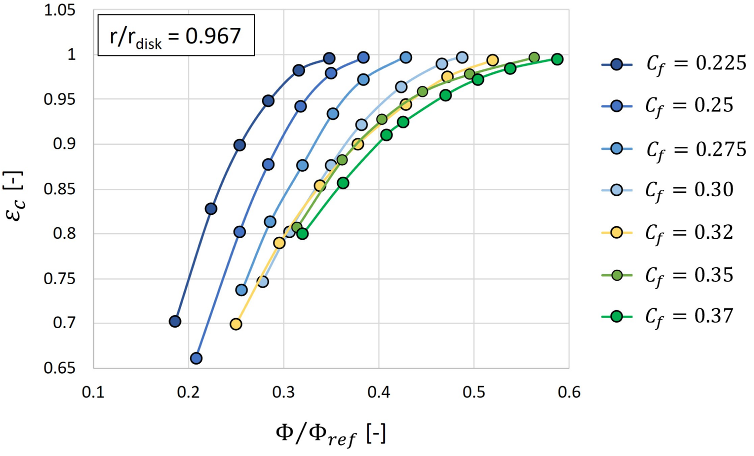

(b) M1A - $r/r_{disk} = 0.967$

Figure 5.4: Comparison between design and off-design $\Phi - \varepsilon_c$ curves obtained for the M1A baseline configuration at (a) $r/r_{disk} = 0.943$ and (b) $r/r_{disk} = 0.967$. © 2024 Baker Hughes Company - All rights reserved

(triangles) and $r/r_{disk} = 0.967$ (circles) and for two different values of sealing flow, $\Phi/\Phi_{ref} = 0.30$ (filled symbols) and $\Phi/\Phi_{ref} = 0.40$ (empty symbols). Once again, the data points measured under design conditions have been highlighted in yellow in order to distinguish them from those obtained under off-design conditions. As can be noticed, for both the investigated radial positions and for both the values of Φ/Φ_{ref}, the variation of ε_c with C_f does not follow a monotonic decreasing trend but, instead, a plateau region or rather a slight increase in effectiveness is confirmed to be present in the range $C_f = 0.32 - 0.35$. This peculiar trend has been recently observed in literature and, although a comprehensive understanding is still lacking, according to Roy et al. [89] it may be attributed to rotational and unsteady effects. However, the author of this work would like to suggest that the incidence angle between the flow path and the rotor blades might also play a role in the occurrence of this

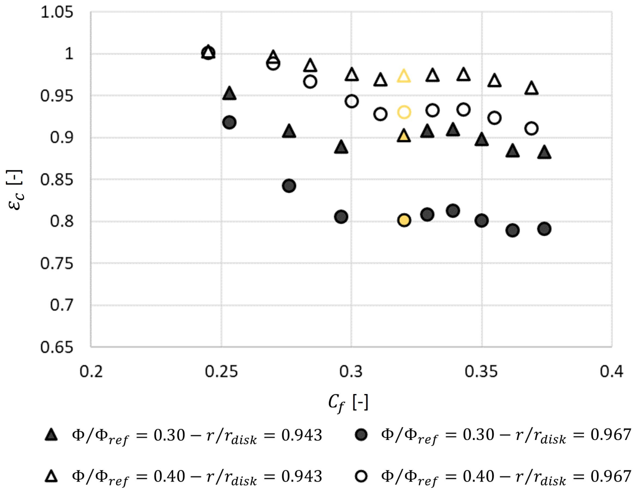

Figure 5.5: Comparison between $C_f - \varepsilon_c$ curves obtained at $r/r_{disk} = 0.943$ and $r/r_{disk} = 0.967$ for two constant values of Φ/Φ_{ref} for the M1A baseline configuration. © 2024 Baker Hughes Company - All rights reserved

phenomenon. This would imply a direct interaction of the potential effect of the LE of the blades on the sealing performance of the rim seal. To support this statement, the variation of the stage velocity triangles for different values of C_f is reported in Figure 5.6. Here, the design condition ($C_f = 0.32$) is indicated in yellow while the lowest tested value of C_f is represented in deep blue ($C_f = 0.225$) and the highest tested value of C_f is represented in deep green ($C_f = 0.37$). As can be noticed, to vary the value of C_f while keeping the rotational velocity constant, it is necessary to progressively adjust the annulus mass flow rate. This leads to a distortion of the velocity triangles and to a variation of the blade inlet angle β. Consequently, the position of the stagnation point on the blades changes accordingly, hence potentially influencing the ingestion level and the sealing performance of the rim seal.

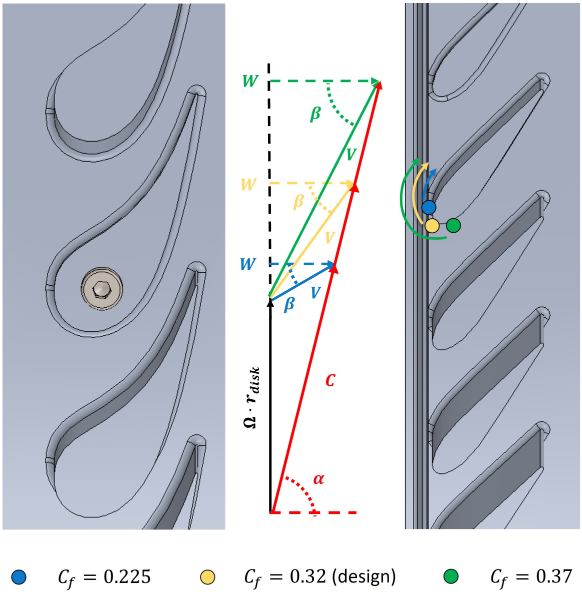

Figure 5.6: Variation of the stage velocity triangles for different values of C_f. © 2024 Baker Hughes Company - All rights reserved

In order to complete the full characterization of the M1A baseline configuration, it is extremely interesting to analyse the values of Φ_{min} and Γ_c obtained for the different tested values of C_f through the application of the Orifice Model EI effectiveness Eq. 2.28. In this regard, the trends of $\Phi_{min}/\Phi_{min,ref}$ and $\Gamma_c/\Gamma_{c,ref}$ as a function of $\Delta C_p^{0.5}$ are respectively reported in Figure 5.7a and Figure 5.7b for both the investigated radial positions, $r/r_{disk} = 0.943$ (triangles) and $r/r_{disk} = 0.967$ (circles). It is worth to mention that the OM fitting of all the curves has not been reported for the sake of brevity, as the agreement with the experimental data consistently proved to be very good, in analogy with the agreement shown in Figure 5.2 for the design conditions. As can be noticed, the design condition has been again highlighted in yellow and the angle $\beta - \beta_{design}$ has been plotted on the upper x-axis. In accordance with the velocity triangles shown in Figure 5.6, $\beta - \beta_{design} = 0$ at design conditions. However, $\beta - \beta_{design} \neq 0$ as the test rig operates at progressively further values of C_f from the design conditions. In particular, $\beta - \beta_{design} < 0$ for $C_f < C_{f,design}$ and $\beta - \beta_{design} > 0$ for $C_f > C_{f,design}$. Regarding the $\Delta C_p^{0.5} - \Phi_{min}/\Phi_{min,ref}$ curves, as already extensively discussed, the higher radius appears to be less protected than the lower one for a given operating condition. Although the trend of $\Phi_{min}/\Phi_{min,ref}$ appears to generally increase with $\Delta C_p^{0.5}$ for both radii, the appearance of a flat region is evident in proximity of the design conditions. This appears to be a secondary effect causing a slight deviation from the otherwise linear trend, which can be attributed to the previously discussed overlapping behaviour of the $\Phi - \varepsilon_c$ curves shown in Figure 5.4. As for the $\Delta C_p^{0.5} - \Gamma_c/\Gamma_{c,ref}$ curves, the trend appears to be very similar between the two radii. At low values of C_f, there is an initial increase until a maximum is reached and then a clear decrease occurs around the design condition. Instead, at high values of C_f, the trend of $\Gamma_c/\Gamma_{c,ref}$ appears to remain relatively constant.

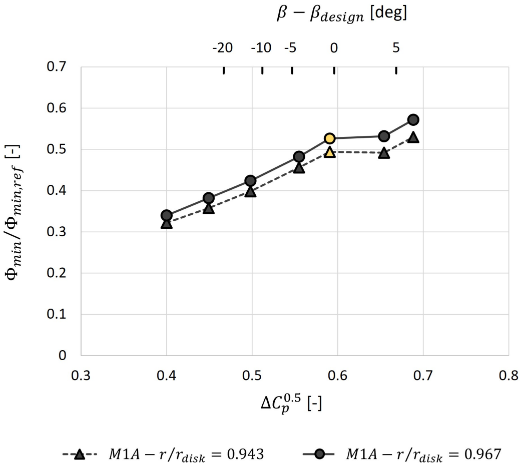

(a) M1A - $\Delta C_p^{0.5} - \Phi_{min}/\Phi_{min,ref}$

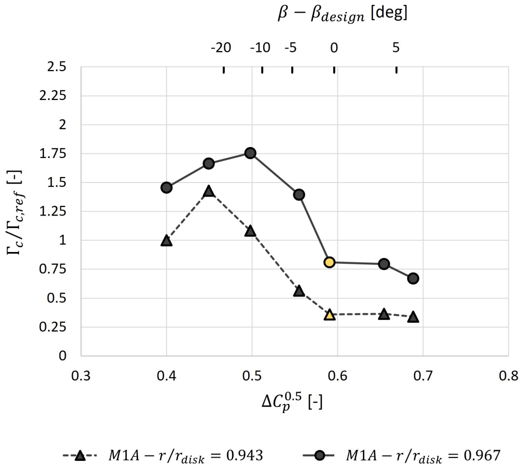

(b) M1A - $\Delta C_p^{0.5} - \Gamma_c/\Gamma_{c,ref}$

Figure 5.7: Trends of (a) $\Delta C_p^{0.5} - \Phi_{min}/\Phi_{min,ref}$ and (b) $\Delta C_p^{0.5} - \Gamma_c/\Gamma_{c,ref}$ obtained at $r/r_{disk} = 0.943$ and $r/r_{disk} = 0.967$ for the M1A baseline configuration by fitting the experimental data points with the Orifice Model. © 2024 Baker Hughes Company - All rights reserved

5.3 Impact of different geometric parameters on the sealing performance

After completely characterizing the M1A baseline configuration under both design and off-design conditions, the experimental campaign was extended to the study of the other six rim seal configurations shown in Figure 4.3. In order to compare the sealing performance of different rim seals, the trends of $\Phi_{min}/\Phi_{min,ref}$ and $\Gamma_c/\Gamma_{c,ref}$ as a function of $\Delta C_p^{0.5}$ will be directly compared without reporting the OM fitting of all the curves, which consistently proved to be very good, in analogy with the agreement shown for the M1A configuration. Moreover, as the curves reported in Figure 5.7 for the M1A configuration exhibit essentially similar trends at the two investigated radial positions, only the results obtained at the radial position $r/r_{disk} = 0.967$ will be discussed here. In the end, this study will allow the determination of the impact of the following geometric parameters on the sealing performance of the cavity:

- Axial overlap (Section 5.3.1);
- Distance between the vanes TE and the blades LE (Section 5.3.2);
- Radial gap (Section 5.3.3);

5.3.1 Impact of the axial overlap

The impact of the axial overlap on the sealing performance of different rim seals can be investigated by comparing the results obtained for M1A with those obtained for M2A. To ease the comparison between the different geometries, the sketches of the two configurations are shown in Figure 5.8. As can be noticed, M1A and M2A share the same value of radial gap $s_{c,rad}$ (hence the same seal clearance ratio G_c) and the same distance between the vanes TE and the blades LE (hence the same value of the axial width between stator and rotor S) but they differ in the value of the axial overlap $s_{overlap}$, with the M2A configuration having a value three times higher than M1A.

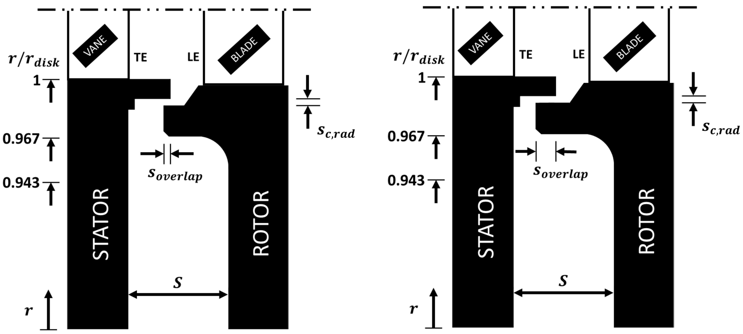

M1A
$G_c = G_{c,ref}$
$s_{overlap} = s_{overlap,ref}$
$S = S_{ref}$

M2A
$G_c = G_{c,ref}$
$s_{overlap} = 3 \cdot s_{overlap,ref}$
$S = S_{ref}$

Figure 5.8: Comparison between M1A and M2A which differ for the value of the axial overlap.

As can be noticed from the results reported in Figure 5.9a, the trend of $\Phi_{min}/\Phi_{min,ref}$ appears to generally increase with $\Delta C_p^{0.5}$ for both the rim seals. However, the flat region appears to be located around the design condition for M1A, while it appears to be shifted to higher values of C_f for M2A. As could be expected, the greater overlap of M2A seems to result in a generally slightly better protection for a given value of $\Delta C_p^{0.5}$. In particular, an axial overlap three times greater results in an average reduction in Φ_{min} of approximately 5%. However, this value appears to be higher (12%) at low values of C_f while it tends to decrease (4%) at high values of C_f due to the presence of the flat region.

The trends of $\Gamma_c/\Gamma_{c,ref}$ reported in Figure 5.9b appear to be very similar between the two rim seals. However, M2A shows relatively lower values of $\Gamma_c/\Gamma_{c,ref}$ both at low and high values of C_f. Although the importance of Γ_c in the evaluation of the sealing performance may not be immediately evident as with Φ_{min}, it is interesting to notice that a lower value of Γ_c results in a steeper gradient in the orifice curve (see Figure 2.47), indicating a higher level of protection across the entire range of Φ.

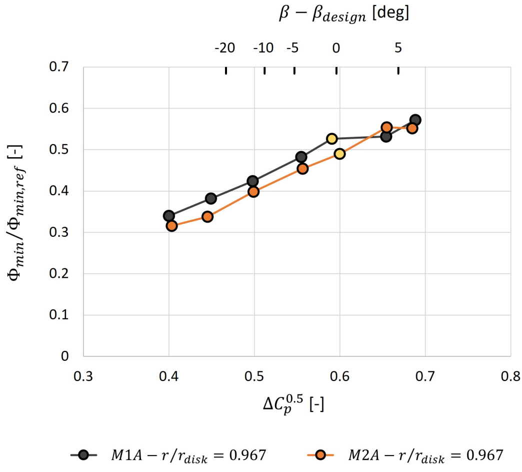

(a) M1A vs M2A - $\Delta C_p^{0.5} - \Phi_{min}/\Phi_{min,ref}$

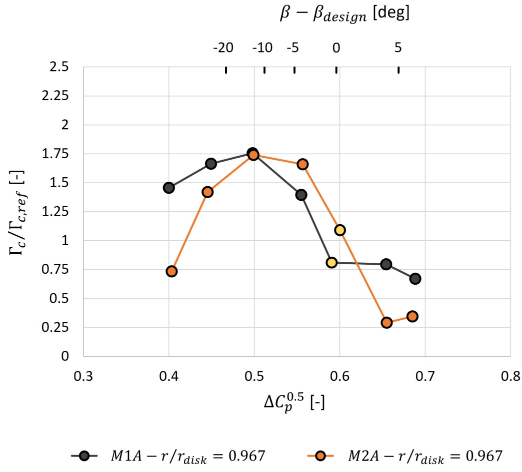

(b) M1A vs M2A - $\Delta C_p^{0.5} - \Gamma_c/\Gamma_{c,ref}$

Figure 5.9: Evaluation of the impact of the axial overlap by comparing M1A and M2A in terms of trends of (a) $\Delta C_p^{0.5} - \Phi_{min}/\Phi_{min,ref}$ and (b) $\Delta C_p^{0.5} - \Gamma_c/\Gamma_{c,ref}$ obtained at $r/r_{disk} = 0.967$ by fitting the experimental data points with the Orifice Model. © 2024 Baker Hughes Company - All rights reserved

5.3.2 Impact of the TE-LE distance

The impact of the TE-LE distance on the sealing performance of different rim seals can be investigated by comparing either the results obtained for M1A with those for M2B or the results obtained for M1B with those for M2C. To ease the comparison between the different geometries, the sketches of the four configurations are shown in Figure 5.10. As can

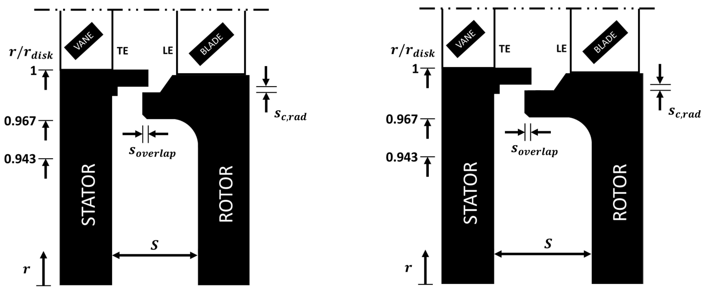

M1A
$G_c = G_{c,ref}$
$s_{overlap} = s_{overlap,ref}$
$S = S_{ref}$

M2B
$G_c = G_{c,ref}$
$s_{overlap} = s_{overlap,ref}$
$S > S_{ref}$

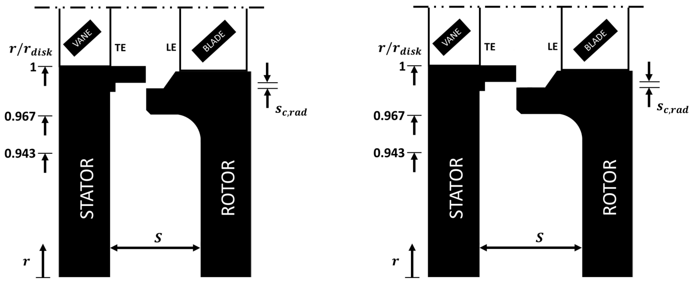

M1B
$G_c = G_{c,ref}$
$s_{overlap} = 0$
$S > S_{ref}$

M2C
$G_c = G_{c,ref}$
$s_{overlap} = 0$
$S \gg S_{ref}$

Figure 5.10: Comparison between M1A, M2B, M1B and M2C which differ for the TE-LE distance. M1A and M2B have the same axial overlap while M1B and M2C have no overlap.

be noticed, the four rim seals share the same value of radial gap $s_{c,rad}$ (hence the same seal clearance ratio G_c). Moreover, M2B has the same value of axial overlap $s_{overlap}$ of M1A but it is characterized by a greater distance between the vanes TE and the blades LE (hence a greater value of the axial width between stator and rotor S). The same situation occurs in the comparison between M1B and M2C, with the only difference being that these two rim seals do not have any axial overlap. Thus, the obtained results will be compared in separate figures for improved clarity.

As can be noticed from the results reported in Figure 5.11a, the trend of $\Phi_{min}/\Phi_{min,ref}$ appears to generally increase with $\Delta C_p^{0.5}$ for both M1A and M2B. However, M2B appears to be slightly better protected, a phenomenon likely due to the reduced impact of the rotor potential effect given the greater vane-blade distance. Nevertheless, this behaviour does not consistently hold true across the entire investigated range of $\Delta C_p^{0.5}$. In fact, at low values of C_f, the values of $\Phi_{min}/\Phi_{min,ref}$ seem to be very similar between the two configurations while a greater difference can be noticed at high values of C_f. Therefore, slightly increasing the TE-LE distance results in an average reduction in Φ_{min} of approximately 6%, with a variation between a minimum of approximately zero and a maximum of 10%. Similar conclusions can be drawn by looking at the comparison between M1B and M2C reported in Figure 5.11b, where the average reduction in Φ_{min} is approximately equal to 4%, with a variation between zero and a maximum of 7%.

The trends of $\Gamma_c/\Gamma_{c,ref}$ reported in Figure 5.12a appear to be qualitatively similar between M1A and M2B. However, the trend of M2B seems to be characterized by smaller amplitude variations, possibly due to the reduced impact of the rotor potential effect. Similar conclusions can be drawn by looking at the comparison between M1B and M2C reported in Figure 5.12b, where a remarkable reduction in amplitude can be observed for M2C. To support the previous observation regarding the reduced influence of the potential effect, it is interesting to keep in mind that M2C has the highest TE-LE distance among all the tested configurations.

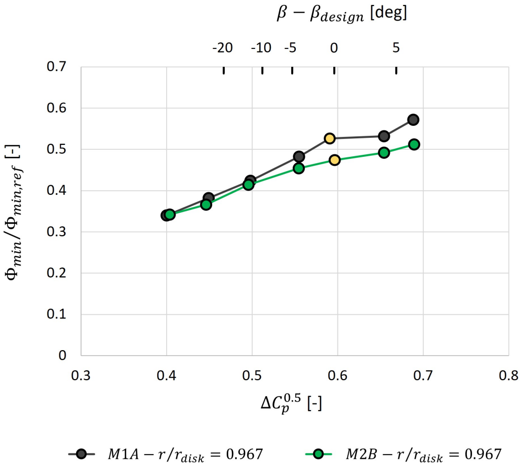

(a) M1A vs M2B - $\Delta C_p^{0.5} - \Phi_{min}/\Phi_{min,ref}$

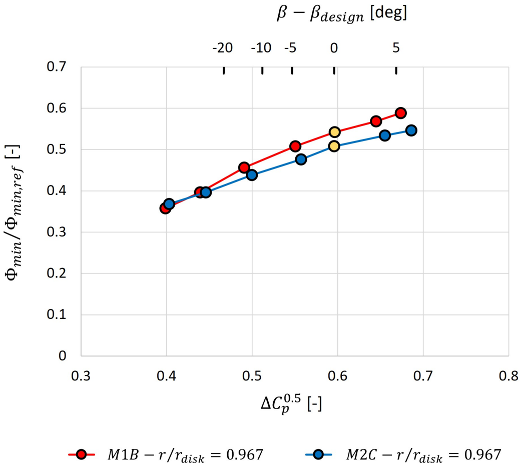

(b) M1B vs M2C - $\Delta C_p^{0.5} - \Phi_{min}/\Phi_{min,ref}$

Figure 5.11: Evaluation of the impact of the TE-LE distance by comparing (a) M1A vs M2B and (b) M1B vs M2C in terms of trends of $\Delta C_p^{0.5} - \Phi_{min}/\Phi_{min,ref}$ obtained at $r/r_{disk} = 0.967$ by fitting the experimental data points with the Orifice Model. © 2024 Baker Hughes Company - All rights reserved

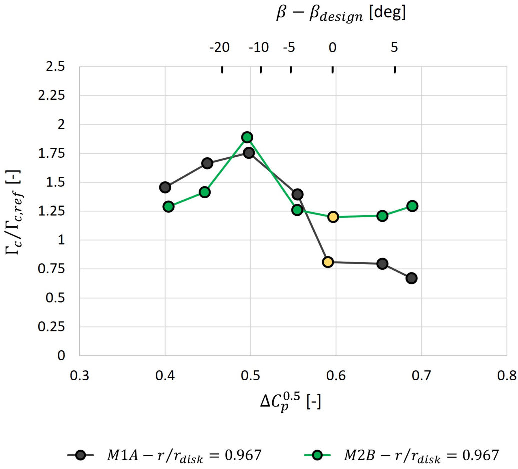

(a) M1A vs M2B - $\Delta C_p^{0.5} - \Gamma_c/\Gamma_{c,ref}$

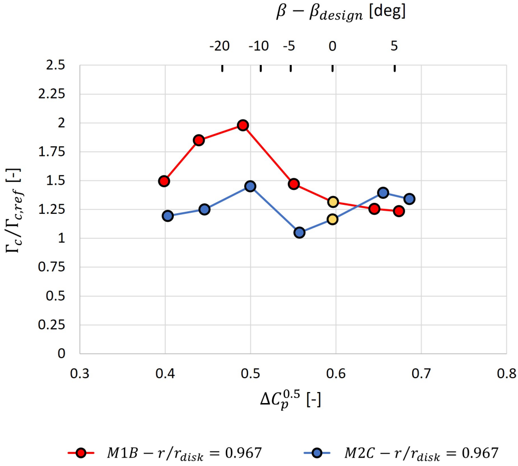

(b) M1B vs M2C - $\Delta C_p^{0.5} - \Gamma_c/\Gamma_{c,ref}$

Figure 5.12: Evaluation of the impact of the TE-LE distance by comparing (a) M1A vs M2B and (b) M1B vs M2C in terms of trends of $\Delta C_p^{0.5} - \Gamma_c/\Gamma_{c,ref}$ *obtained at* $r/r_{disk} = 0.967$ *by fitting the experimental data points with the Orifice Model. © 2024 Baker Hughes Company - All rights reserved*

5.3.3 Impact of the radial gap

The impact of the radial gap on the sealing performance of different rim seals can be investigated by comparing either the results obtained for M1A with those for M3A or the results obtained for M1B with those for M3B. To ease the comparison between the different geometries, the sketches of the four configurations are shown in Figure 5.13. As can be

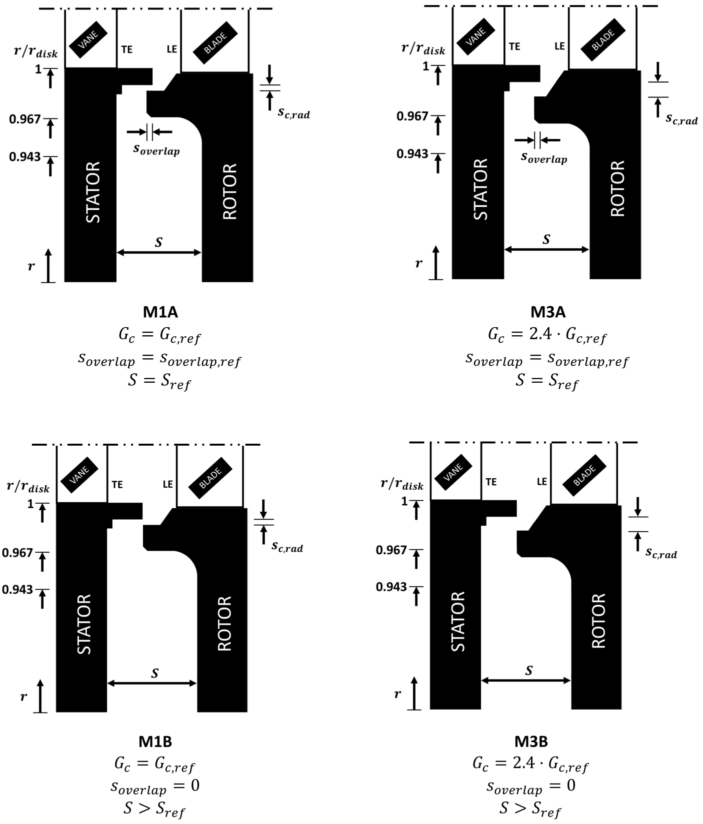

M1A
$G_c = G_{c,ref}$
$s_{overlap} = s_{overlap,ref}$
$S = S_{ref}$

M3A
$G_c = 2.4 \cdot G_{c,ref}$
$s_{overlap} = s_{overlap,ref}$
$S = S_{ref}$

M1B
$G_c = G_{c,ref}$
$s_{overlap} = 0$
$S > S_{ref}$

M3B
$G_c = 2.4 \cdot G_{c,ref}$
$s_{overlap} = 0$
$S > S_{ref}$

Figure 5.13: Comparison between M1A, M3A, M1B and M3B which differ for the value of the radial gap. M1A and M3A have the same axial overlap while M1B and M3B have no overlap.

noticed, M1A and M3A share the same value of axial overlap $s_{overlap}$ and the same distance between the vanes TE and the blades LE (hence the same value of the axial width between stator and rotor S) but they differ in the value of the radial gap $s_{c,rad}$ (hence of the seal clearance ratio G_c), with the M3A configuration having a value 2.4 times higher than M1A. The same situation occurs in the comparison between M1B and M3B, with the only difference being that these two rim seals do not have any axial overlap. Thus, the obtained results will be compared in separate figures for improved clarity.

As can be noticed from the results reported in Figure 5.14a, the trend of $\Phi_{min}/\Phi_{min,ref}$ appears to generally increase with $\Delta C_p^{0.5}$ for both M1A and M3A. However, the flat region is not evident for M3A and it is also interesting to notice that, although M3A has a greater radial gap, it requires lower values of $\Phi_{min}/\Phi_{min,ref}$ to be fully sealed. Similar conclusions can be drawn by looking at the comparison between M1B and M3B reported in Figure 5.14b. However, this observation should not mislead the reader into thinking that a larger radial gap results in a better sealing performance, as the dimensional flow rate required to seal M3A is indeed greater than that needed to seal M1A. In the same way, this phenomenon can be observed between M3B and M1B. Hence, this behaviour is evident by looking at the variation of $C_{w,min}/C_{w,min,ref}$ with $\Delta C_p^{0.5}$, which has been respectively reported in Figure 5.15a for M1A-M3A and in Figure 5.15b for M1B-M3B. In fact, the definition of C_w does not contain the term G_c, making this parameter an indicator of the actual value of the dimensional flow rate required to seal the cavity.
In particular, a radial gap 2.4 times greater results in an average increase in $C_{w,min}$ of approximately 44%, with a minimum of 37% and a maximum of 51% for the case with overlap (M1A vs M3A). These values slightly increase for the case without overlap (M1B vs M3B), resulting in an average increase in $C_{w,min}$ of approximately 60%, with a minimum of 58% and a maximum of 64%. Therefore, this implies that the amount of purge flow required to seal a cavity does not increase linearly with the radial gap and, consequently, with the value of G_c used to derive the value of Φ.

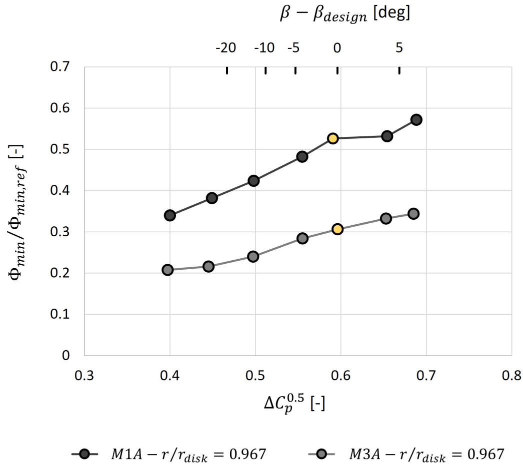

(a) M1A vs M3A - $\Delta C_p^{0.5} - \Phi_{min}/\Phi_{min,ref}$

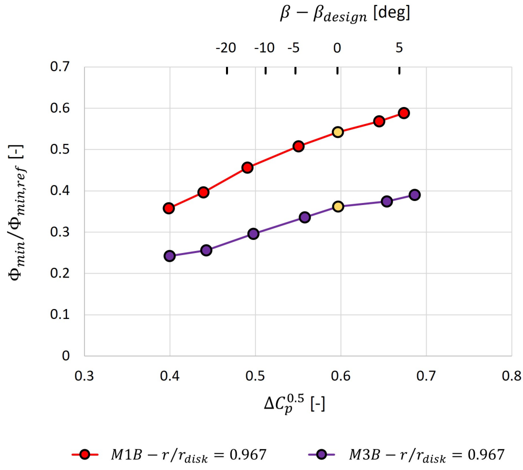

(b) M1B vs M3B - $\Delta C_p^{0.5} - \Phi_{min}/\Phi_{min,ref}$

Figure 5.14: Evaluation of the impact of the radial gap by comparing (a) M1A vs M3A and (b) M1B vs M3B in terms of trends of $\Delta C_p^{0.5} - \Phi_{min}/\Phi_{min,ref}$ *obtained at* $r/r_{disk} = 0.967$ *by fitting the experimental data points with the Orifice Model. © 2024 Baker Hughes Company - All rights reserved*

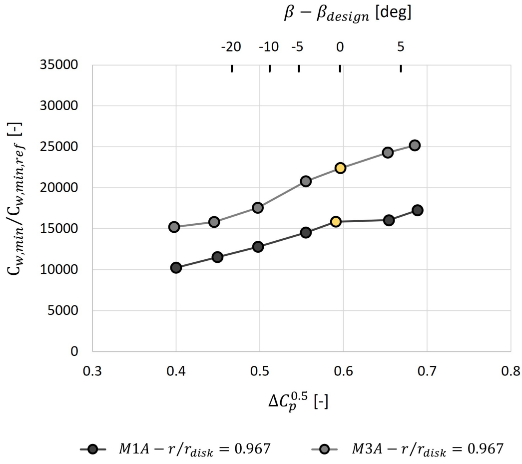

(a) M1A vs M3A - $\Delta C_p^{0.5} - C_{w,min}/C_{w,min,ref}$

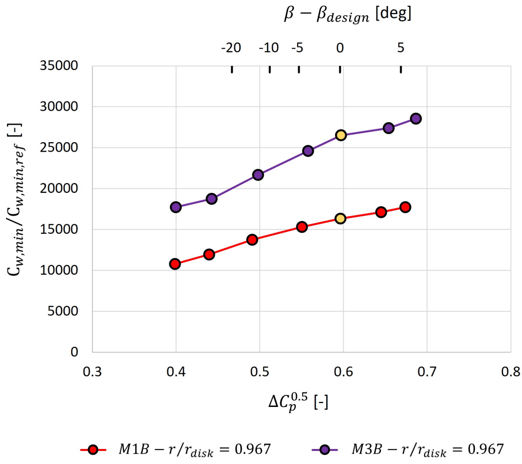

(b) M1B vs M3B - $\Delta C_p^{0.5} - C_{w,min}/C_{w,min,ref}$

Figure 5.15: Evaluation of the impact of the radial gap by comparing (a) M1A vs M3A and (b) M1B vs M3B in terms of trends of $\Delta C_p^{0.5} - C_{w,min}/C_{w,min,ref}$ obtained at $r/r_{disk} = 0.967$ by fitting the experimental data points with the Orifice Model. © 2024 Baker Hughes Company - All rights reserved

To conclude this part, it is possible to speculate that this phenomenon might be also influenced by the fact that the greater quantity of egress flow associated to the M3 configuration may increase the damping effect attributed to the buffer region located above the rotor tooth.

The trends of $\Gamma_c/\Gamma_{c,ref}$ reported in Figure 5.16a and Figure 5.16b appear to be qualitatively similar for the two couples of configurations. However, the trend obtained for M3B seems to be shifted to lower values of Γ_c compared to that of M1B but with comparable amplitudes. This observation is partially confirmed also by the comparison between M1A and M3A, except for a point around the design condition. This discrepancy could be due to the presence of the flat region, which particularly characterized the data obtained for M1A. However, it could also be partially attributed to potential uncertainties in the OM fitting operation.

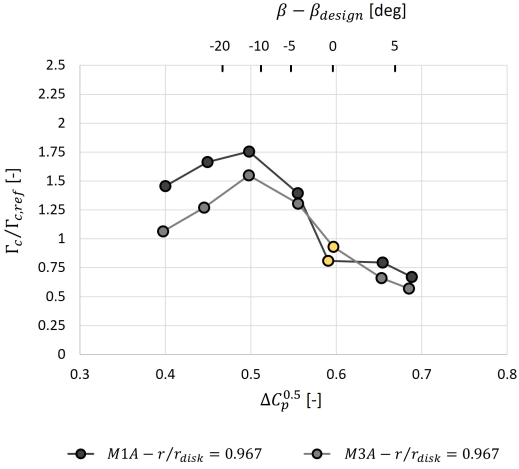

(a) M1A vs M3A - $\Delta C_p^{0.5} - \Gamma_c/\Gamma_{c,ref}$

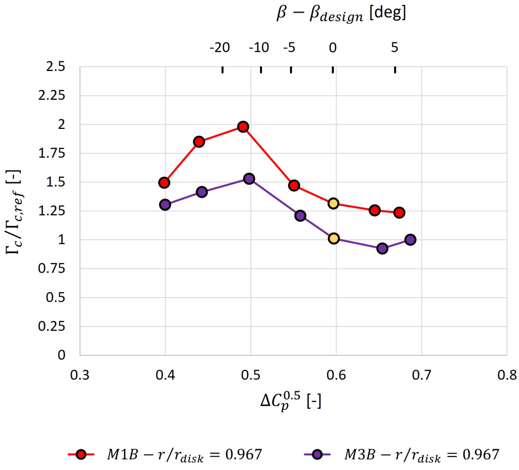

(b) M1B vs M3B - $\Delta C_p^{0.5} - \Gamma_c/\Gamma_{c,ref}$

Figure 5.16: Evaluation of the impact of the radial gap by comparing (a) M1A vs M3A and (b) M1B vs M3B in terms of trends of $\Delta C_p^{0.5} - \Gamma_c/\Gamma_{c,ref}$ *obtained at* $r/r_{disk} = 0.967$ *by fitting the experimental data points with the Orifice Model. © 2024 Baker Hughes Company - All rights reserved*

Chapter 6

Use of PSP to determine the rim sealing effectiveness

Contents

6.1 PSP results overview

The intent of this chapter is to report and discuss the experimental results obtained through the use of the PSP setup described in Figure 4.9, starting from the contours obtained on the stator side of the cavity. All the results reported in this chapter have been obtained by using pure N_2 as purge flow, thus allowing a preliminary comparison with the effectiveness values obtained through standard CO_2 gas concentration measurements in order to validate the application of the PSP technique for the study of hot gas ingestion. Subsequently, the validated PSP setup has been used to obtain 2D maps on the rotor side of the cavity. In particular, attention will be drawn to the presence of non-uniform distributions of effectiveness in the circumferential direction on the tip of the rim seal tooth. Then, the results obtained on both sides of the cavity will be directly compared to highlight the presence of higher effectiveness values on the rotor surface, a phenomenon attributed to the presence of a buffer layer formed by the purge flow pumped towards the outer radius by the rotation of the rotor disk. In the end, the PSP results obtained separately on the stator and rotor surfaces will be correlated with each other by performing sealing effectiveness measurements across the cavity width through the use of the concentration probe shown in Figure 4.10.

The test matrix used to conduct the present study includes three different values of C_f in order to compare the behaviour of the rim seal under design conditions ($C_f = 0.32$) with that under off-design conditions both at lower ($C_f = 0.25$) and higher ($C_f = 0.40$) value of Re_w. Moreover, multiple values of purge flow have been tested in order to analyse the performance of the rim seal under different sealing conditions. Additionally, it is crucial to note that the PSP tests have been conducted only for the baseline M1A rim seal configuration shown in Figure 4.3.

6.2 PSP results on stator side

The first step after completing the PSP setup was to conduct a series of experiments by using pure N_2 as purge flow to determine the PSP effectiveness on the stator surface. Hence, the resulting 2D contours have been reported in Figure 6.1 for three increasing values of Φ/Φ_{ref}. These maps represent the effectiveness derived directly from the images obtained during the experiments, without performing any interpolation by using Cartesian or polar coordinates. Moreover, the obtained contours have been superimposed onto the model of the stator disk in order to highlight the position of the vanes. As can be noticed, the sealing level steadily rises with the injection of more purge air into the cavity. This can be attributed to the increased pressurization of the wheel-space, which leads to a corresponding reduction in the pressure difference between the external annulus flow and the flow within the cavity. Furthermore, for each tested value of Φ/Φ_{ref}, the minimum values of ε_{PSP} can be found in proximity of the cavity entrance. This high effectiveness gradient is likely due to the presence of the mixing region, where the ingress flow mixes with the flow that recirculates within the cavity.

The effectiveness exhibits variations along the radial direction and therefore it does not appear to be perfectly constant, as found for example by Sangan [11]. However, this trend is consistent with the results obtained through the application of the gas sampling technique discussed in Figure 5.3 and with the findings presented in recent literature studies [87, 88, 89]. As previously explained, this phenomenon has been attributed to the presence of an expanded mixing region resulting from the impingement of the rotor boundary layer on the stator surface. Moreover, no 2D phenomena seem to be present for any of the investigated values of purge flow, thus suggesting that the sealing effectiveness is substantially uniform in the circumferential direction. However, this observation could be tied to the use of a low-frequency PSP formulation that required averaging each set of images to obtain a representative snapshot of the flow field inside the wheel-space.

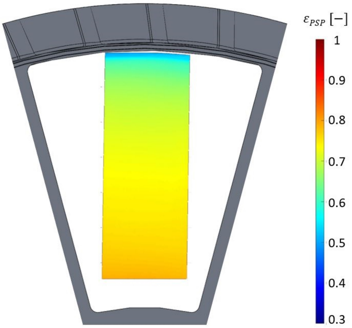

(a) $\Phi/\Phi_{ref} = 0.166$

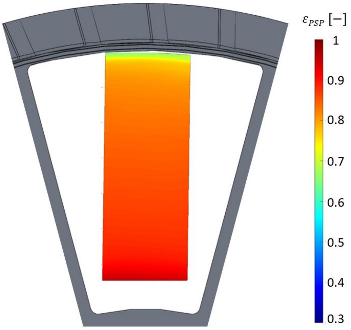

(b) $\Phi/\Phi_{ref} = 0.230$

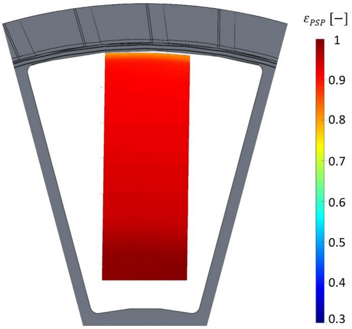

(c) $\Phi/\Phi_{ref} = 0.304$

Figure 6.1: PSP effectiveness contours obtained on the stator side for three different values of purge flow: (a) $\Phi/\Phi_{ref} = 0.166$, (b) $\Phi/\Phi_{ref} = 0.230$ and (c) $\Phi/\Phi_{ref} = 0.304$ [79]. © 2024 Baker Hughes Company - All rights reserved

6.2.1 Validation of the PSP technique

A conversion from Cartesian to polar coordinates was then applied to the 2D maps reported in Figure 6.1 in order to be able to derive the radial profiles of the circumferentially averaged values of sealing effectiveness. Thanks to this conversion, it was possible to easily extract and average row values from the data matrices in order to validate the application of the PSP technique for the study of hot gas ingestion. Indeed, this approach allowed a direct comparison between the radial profiles of effectiveness obtained with PSP and those obtained through standard CO_2 concentration measurements. It is important to point out that this comparison is fundamental, given the use of a non-conventional setup that involves the installation of both the camera and the illumination device on the "back side" of the paint. Moreover, the validity of this comparison was ensured by the fact that the purge flow in the PSP measurements consisted of pure N_2, which has a density almost equal to that of the air used for the concentration measurements, thus allowing the neglect of the impact of the Density Ratio between the external annulus flow and the sealing flow. Indeed, although the air used for the concentration measurements is seeded with a small percentage of CO_2, this value never exceeds the 3-4% of the total purge flow rate injected inside the wheel-space due to the limitations imposed by the datasheet of the employed gas analyser.

A comparison between the results obtained with the two different techniques is reported in Figure 6.2, where the dots and the dashed lines respectively represent the data acquired through gas sampling and PSP. As can be noticed, the comparison in terms of radial profiles of sealing effectiveness is highly satisfactory, as both the trends and the absolute values exhibit strong agreement for every tested value of Φ/Φ_{ref}. However, a more detailed examination of this figure may lead to further interesting insights. Despite the discrepancies between the two data sets are minimal and almost entirely limited within the computed measurement uncertainty reported in Table 4.1, the agreement seems to progressively improve as the value of Φ/Φ_{ref} injected inside the wheel-space increases. Since the

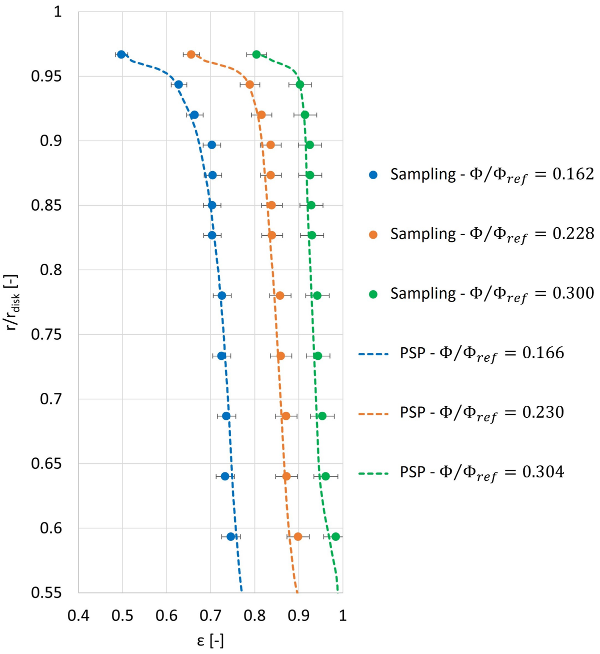

Figure 6.2: Comparison between PSP and gas sampling radial profiles of ε [79]. © 2024 Baker Hughes Company - All rights reserved

flow rate extracted from the cavity and directed towards the gas analyser is typically kept constant for the sake of simplicity, these small differences could be attributed to the intrusiveness of the gas sampling technique. Indeed, despite the generally small impact on the effectiveness values of this measurement technique, which involves extracting air from the stator boundary layer, the measurement clearly becomes more intrusive at lower values of Φ/Φ_{ref}. Nevertheless, the agreement between the two techniques seems to be sufficiently strong to confirm the validity of the PSP approach for the study of hot gas ingestion.

To conclude this part relative to the stator side of the cavity, Figure 6.3 compares the $\Phi - \varepsilon$ curves obtained under design conditions ($C_f = 0.32$)

by using either the PSP or the gas sampling technique. The measurements have been conducted at two distinct radii, $r/r_{disk} = 0.943$ (triangles) and $r/r_{disk} = 0.967$ (circles), and clearly confirm the considerably good agreement between the two employed techniques. This result was expected to be found according to the validation presented in Figure 6.2. However, it was not taken for granted due to the complexities associated with this type of measurement, such as the potential presence of optical distortions due to the interposition of the PMMA of the stator cover, the already mentioned use of a "back side" approach and the possibility to obtain blurred images due to the rotation of the rotor disk. Moreover, the absence of comparable studies in the open literature posed an additional challenge. Nevertheless, according to the validation results presented in this section, the final setup depicted in Figure 4.9 was found to be perfectly suitable for the objectives of this work.

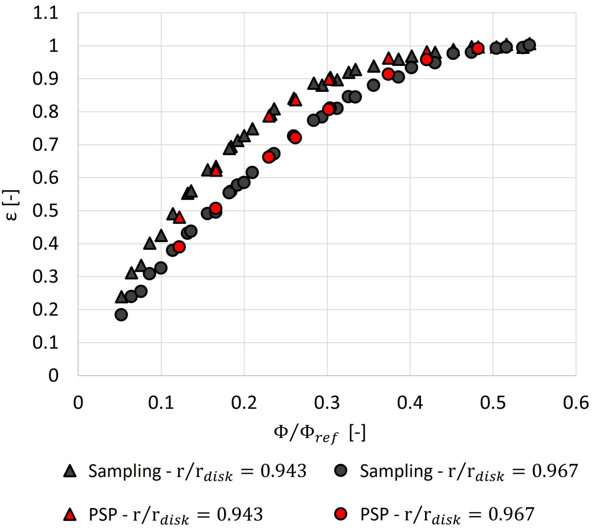

Figure 6.3: Comparison between PSP and gas sampling $\Phi - \varepsilon$ curves [79].
© 2024 Baker Hughes Company - All rights reserved

6.3 PSP results on rotor side

The validated PSP setup was then employed to obtain 2D effectiveness maps on the rotor side of the cavity, maintaining a consistent approach with the measurements conducted on the stator side. Once again, pure N_2 has been used as oxygen-free gas to purge the wheel-space in order to avoid including additional effects due to the influence of the Density Ratio. During the experimental campaign, multiple tests have been conducted at different values of C_f and Φ/Φ_{ref} and the most interesting results are reported in Figure 6.4. Here, two sets of images corresponding to the injection of two different values of sealing flow, $\Phi/\Phi_{ref} = 0.166$ on the left half and $\Phi/\Phi_{ref} = 0.230$ on the right half, have been superimposed onto the model of the rotor disk. Furthermore, three distinct values of C_f have been examined for each value of purge flow. As already mentioned, the case at $C_f = 0.32$ corresponds to the design condition, while the cases at $C_f = 0.25$ and $C_f = 0.40$ represent off-design conditions respectively corresponding to lower and higher values of Re_w and, consequently, of the annulus mass flow rate.

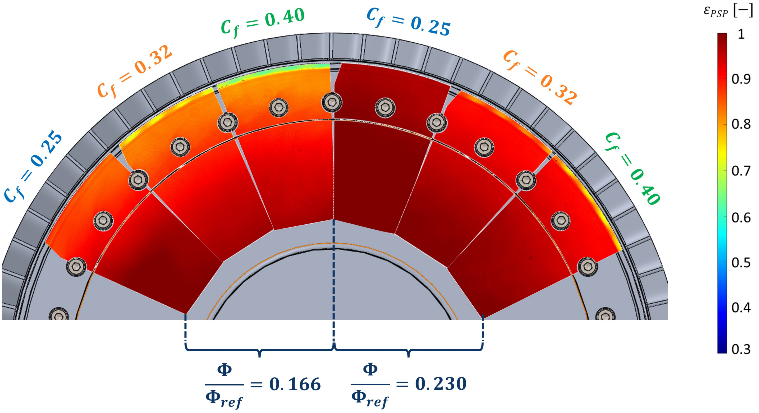

Figure 6.4: PSP effectiveness contours obtained on the rotor side for different values of C_f and Φ/Φ_{ref} [79]. © 2024 Baker Hughes Company - All rights reserved

The analysis of the resulting contours highlights that maintaining a constant Φ/Φ_{ref} while increasing C_f, and consequently ΔC_p due to their linear relationship, results in lower effectiveness values. This can be attributed to the increased potential of the ingress driving force. On the contrary, when C_f is held constant, increasing the quantity of purge flow leads to higher effectiveness values, owing to the increased pressurization of the wheel-space. In analogy with the stator side, no 2D structures appear to be present in the contours obtained on the rotor, thus implying a significant circumferential uniformity of ε_{PSP}. Nevertheless, it is crucial to bear in mind that the data obtained through PSP are time-averaged and the images on the rotor side are all taken by triggering the laser and the camera when the rotor reaches the same tangential position.

Additionally, it is important to point out that the PSP technique allows capturing data even on the tip of the seal tooth, a region that otherwise would be challenging, if not impossible, to investigate using the standard gas sampling approach due to the complexity of positioning probes or concentration taps on such a small surface (order of millimetres). This feature allows the identification of the presence of non-uniform distributions of effectiveness in the circumferential direction at $C_f = 0.32$ and $C_f = 0.40$. This phenomenon, evident upon careful examination of Figure 6.4, has not yet been documented in the open literature through 2D measurements. Therefore, it necessitates a more comprehensive investigation that will be reported in details in the next section.

The acquired 2D effectiveness maps were then post-processed by using the same procedure applied to the stator to extract the circumferentially averaged radial profiles of effectiveness. Subsequently, the radial profiles extracted from the stator and the rotor could be compared to simultaneously illustrate the different behaviours of the two sides of the cavity. This comparison is presented in Figure 6.5 for the same three increasing values of Φ/Φ_{ref} which were used to validate the PSP technique. The analysis of these profiles demonstrate that, for a given radius and value of Φ/Φ_{ref}, the rotor side consistently exhibits an higher effectiveness value compared to the stator side. These trends are in accordance with

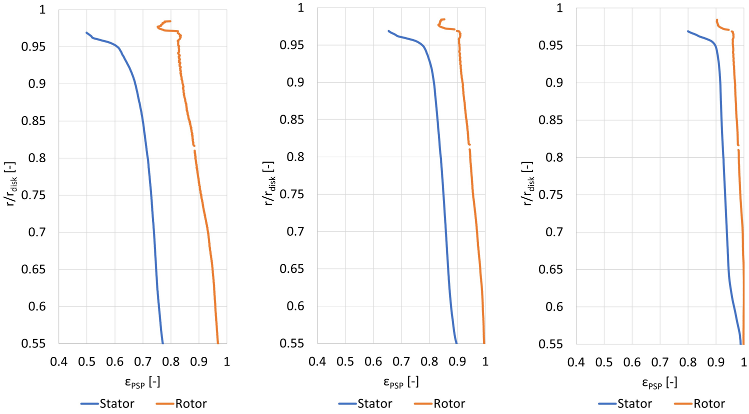

(a) $\Phi/\Phi_{ref} = 0.166$ (b) $\Phi/\Phi_{ref} = 0.230$ (c) $\Phi/\Phi_{ref} = 0.304$

Figure 6.5: Comparison between radial profiles of ε_{PSP} obtained on both the stator and the rotor sides for three different values of purge flow: (a) $\Phi/\Phi_{ref} = 0.166$, (b) $\Phi/\Phi_{ref} = 0.230$ and (c) $\Phi/\Phi_{ref} = 0.304$ [79]. © 2024 Baker Hughes Company - All rights reserved

a limited number of literature studies that have managed to compare effectiveness measurements between the two sides of the cavity, as for example [12, 13, 62, 90]. In these studies, the higher effectiveness on the rotor surface was attributed to the presence of a buffer layer formed by the purge flow pumped towards the outer radius by the rotation of the rotor disk. Furthermore, the acquired radial profiles indicate that, for a given increase in Φ/Φ_{ref}, the improvement in effectiveness on the stator side is greater than on the rotor side. However, both profiles tend to reach the fully sealed condition for the same value of Φ/Φ_{ref}, in accordance with the expected theoretical fluid dynamic behaviour of stator-rotor wheel-spaces. In fact, due to the mixing between the flows on the two sides of the cavity, the rotor will never achieve complete sealing for a lower Φ with respect to the stator. Consequently, this also implies that a significant amount of ingestion can occur while still recording acceptable effectiveness values on the rotor surface.

6.3.1 Non-uniform circumferential distributions of effectiveness on the rim seal tooth

Starting from the observation made in the previous paragraph regarding the presence of non-uniform distributions of effectiveness on the tip of the rim seal tooth, it is therefore very interesting to investigate in detail the region at high radius of the radial profiles extracted from the rotor contours. To better visualize the effectiveness behaviour in this region, an enhanced view of Figure 6.5b is reported in Figure 6.6a, where the sketch of the rotor tooth has been also added in transparency. As can be noticed, the effectiveness behaviour in this region appears to be quite complex but it can be explained by considering one of the raw PSP images obtained during the experimental campaign, such as the one shown in Figure 6.6b. Hence, a decrease in the effectiveness values, consistent with the presence of the previously mentioned low-effectiveness bubbles, appears to be evident in correspondence of the seal tooth which is situated between the green and the blue lines. The shape of these bubbles, whose location has been highlighted in red, resembles an ellipsoid and since the radial profiles have been derived by circumferentially averaging the contour values, the minimum of ε_{PSP} appears to be positioned in correspondence of the major axis of the bubbles, indicated by the yellow dashed line. Moreover, it is also important to notice the presence of a very small peak of effectiveness within the region bounded by the blue and the purple lines. As this behaviour does not appear to be physical, it has been attributed to an uneven illumination resulting from the presence of a fillet in the cavity geometry. However, this effect only leads to minor measurement inaccuracies which are limited to a small region extending radially for less than one millimetre.

The presence of these low-effectiveness regions has been then further investigated by extracting the circumferential profiles of effectiveness from the 2D contours and plotting them against the circumferential coordinate θ. The resulting profiles are shown in Figure 6.7a, which compares the results obtained for three distinct values of Φ/Φ_{ref} while maintaining constant the flow coefficient ($C_f = 0.32$). As can be noticed,

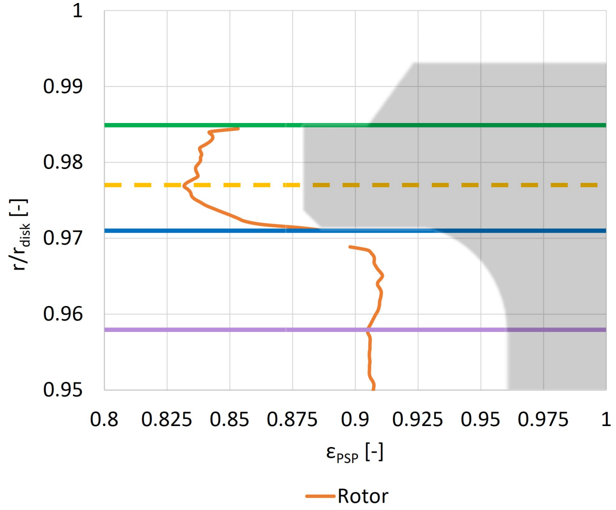

(a) $\Phi/\Phi_{ref} = 0.230$

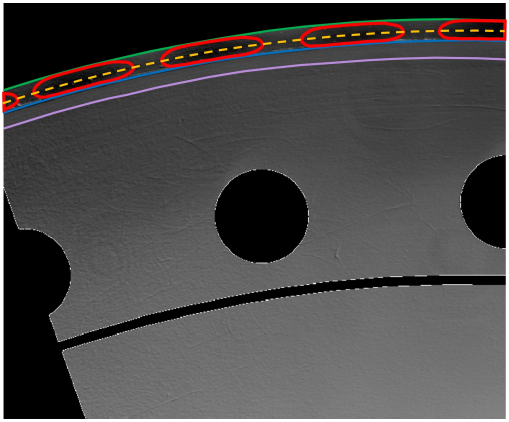

(b) Raw PSP image

Figure 6.6: (a) Detail of the rotor radial profile at high radius obtained for $\Phi/\Phi_{ref} = 0.230$ *and (b) Example of raw image extracted from PSP measurements [79].*

four periodic oscillations are evident for each case and their amplitude appears to decrease as Φ/Φ_{ref} increases (indicating pressurization of the cavity). Additionally, the relative position of the peaks seems to be slightly affected by the value of Φ/Φ_{ref}, showing a gradual shift as the cavity pressure increases. On the contrary, a different approach has been employed for the generation of Figure 6.7b, which compares the results obtained for three distinct values of C_f while maintaining constant the purge flow ($\Phi/\Phi_{ref} = 0.304$). As previously mentioned, the four periodic oscillations are only present at $C_f = 0.32$ and $C_f = 0.40$. It is evident that an increase in C_f, and consequently in ΔC_p, leads to oscillations with a greater amplitude, while the position of the peaks remains essentially unchanged. The behaviour of ε_{PSP} at $C_f = 0.25$ is instead considerably different, exhibiting a constant linear trend without any oscillation.

The results shown in Figure 6.7 indicate an almost perfect clocking between the effectiveness oscillations and the LE of the blades. According to this observation, it could be speculated that the presence of such regions with reduced sealing effectiveness may be induced by the external static pressure distribution generated by the rotor blades. As a matter of fact, this distribution appears to locally impact the egress and ingress mechanisms, thus having a direct impact on the sealing effectiveness on the rotor side and consequently also on the stator side. The close proximity between the entrance to the cavity and the LE of the blades, resembling realistic engine configurations, might be a contributing factor to the appearance of these low effectiveness regions. Moreover, this phenomenon seems to be promoted under operating conditions characterized by higher values of mass flow rate in the annulus ($C_f = 0.32$ and $C_f = 0.40$). In the end, the purge flow appears to have an influence on both the intensity and the tangential position of the peaks, thus highlighting that there is a mutual interaction between the external conditions on the mainstream side (mass flow rate and static pressure distribution) and the purging conditions.

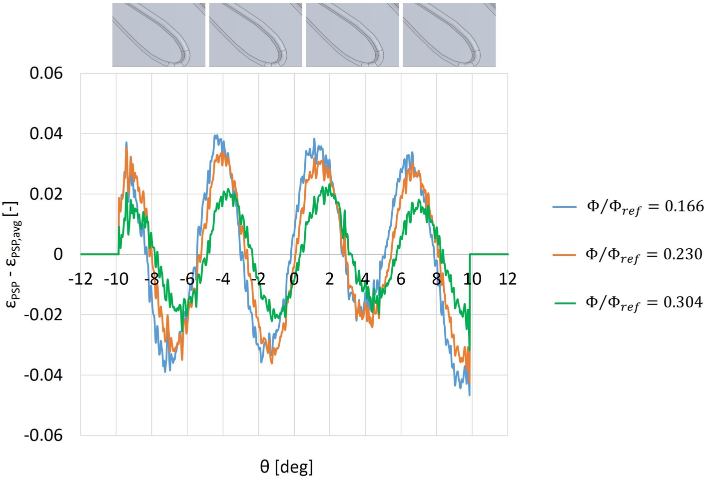

(a) $C_f = 0.32$ with variable Φ/Φ_{ref}

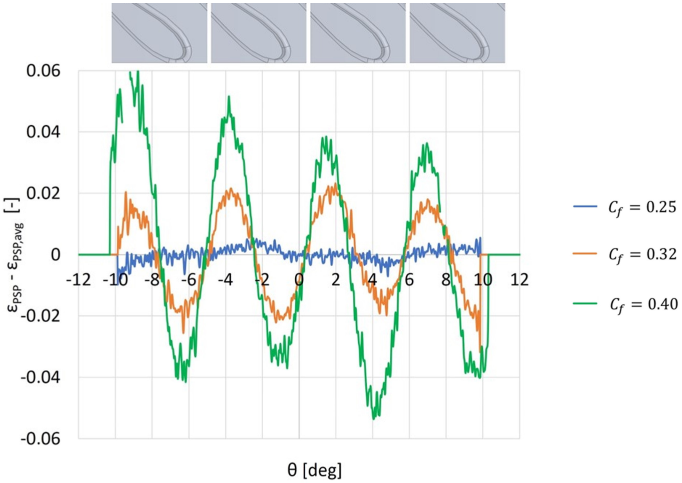

(b) $\Phi/\Phi_{ref} = 0.304$ with variable C_f

Figure 6.7: Circumferential profiles of effectiveness extracted on the front face of the seal tooth: (a) $C_f = 0.32$ with variable Φ/Φ_{ref} and (b) $\Phi/\Phi_{ref} = 0.304$ with variable C_f [79]. © 2024 Baker Hughes Company - All rights reserved

6.4 Analysis of PSP data on stator and rotor side

The experimental data points collected from both the stator and the rotor side can then be compared in terms of $\Phi - \varepsilon$ curves. Hence, Figure 6.8 illustrates the resulting curves obtained at a radial position of $r/r_{disk} = 0.943$ for the usual three values of flow coefficient. Here, the filled symbols correspond to measurements performed on the stator side while the empty symbols correspond to measurements performed on the rotor side. The data on the stator side have been fitted by using the Orifice Model equations derived by Owen [9, 14] and rearranged by Sangan et al. [8] into the explicit EI effectiveness Eq. 2.28. On the other hand, the data on the rotor side have been fitted by using the Buffer Ratio model developed by Mear et al. [13] which consists of Eq. 2.36 where the term BR is defined by Eq. 2.37.

As shown in Figure 6.8, the experimental data points are in good agreement with the corresponding fitting model for each value of C_f. Furthermore, the experiments confirm the presence of a buffer layer on the rotor surface which consistently results in higher effectiveness values compared to the stator side across the entire range of Φ/Φ_{ref} and for all the tested values of flow coefficient. Then, it is also interesting to notice that, under each tested condition, both rotor and stator curves reach the fully sealed condition for identical values of Φ_{min}, thus confirming one of the main hypotheses underlying the development of the Buffer Ratio model.

6.4.1 Seal effectiveness across the cavity width

The values of sealing effectiveness acquired across the cavity width by using the concentration probe can finally be employed to correlate the PSP results obtained separately on the stator and rotor surfaces. Therefore, the axial distributions of effectiveness obtained under design conditions ($C_f = 0.32$) for the usual three values of Φ/Φ_{ref} have been reported in Figure 6.9 along with the averaged values measured by PSP directly on the two cavity surfaces.

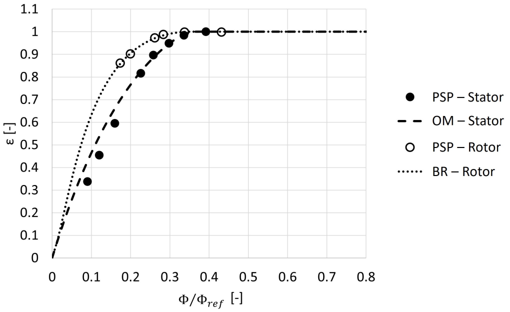

(a) $C_f = 0.25$

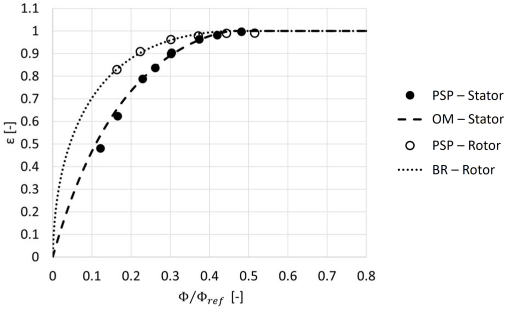

(b) $C_f = 0.32$

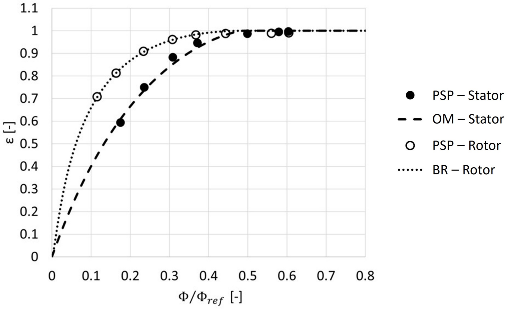

(c) $C_f = 0.40$

Figure 6.8: Comparison in terms of $\Phi - \varepsilon$ curves between stator (OM fitting) and rotor (BR fitting) obtained at $r/r_{disk} = 0.943$ for different values of C_f: (a) $C_f = 0.25$, (b) $C_f = 0.32$ and (c) $C_f = 0.40$ [79]. © 2024 Baker Hughes Company - All rights reserved

Despite the potential intrusiveness of the probe, the plot reveals interesting patterns that characterize the behaviour of the flow at a radial position in the core region ($r/r_{disk} = 0.80$), far from the outer region which is instead located in correspondence of the rim seal. On the stator side, the sealing effectiveness appears to be relatively constant, at least for the initial quarter of the cavity width. Moving away from the stator, the effectiveness then gradually rises, reaching its maximum on the rotor surface. Although this behaviour aligns to some extent with the thermal Buffer Ratio model, the extension of the region near the stator surface characterized by a constant concentration appears to be confined to the initial part of the cavity. This suggests the presence of a thick rotor boundary layer at the examined radial position. Besides the interesting result concerning the distributions of effectiveness in the axial direction, the PSP values obtained on both the stator and rotor surfaces appear to reasonably match the data points acquired by using the concentration probe. Hence, this consistency further enhances the robustness and reliability of the proposed measurement approach.

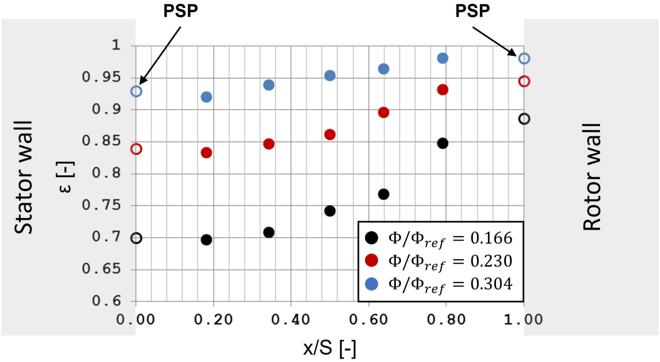

Figure 6.9: Seal effectiveness profiles across the cavity width obtained at $C_f = 0.32$, $r/r_{disk} = 0.80$ and for three different values of Φ/Φ_{ref} by using the concentration probe. The data on the stator and rotor walls are instead obtained by using PSP [79]. © 2024 Baker Hughes Company - All rights reserved

6.5 Concluding remarks on the use of PSP for hot gas ingestion

Now, the reader might question the necessity of employing this optical PSP approach in studies related to hot gas ingestion, given the reliability of the more standard gas sampling technique. According to the results presented in this chapter, several aspects can be taken into consideration to give an answer to this question.

First, it is essential to keep in mind that after validating the optical PSP setup, acquiring a detailed map of the effectiveness within the wheel-space is significantly faster (in the order of ten seconds) than conducting multiple sampling measurements at different radii. In fact, the latter operation necessitates a multichannel system equipped with valves and pipes which may require considerable time to convey the air extracted from the wheel-space to the gas analyser due to the extremely small flow rates involved. Additionally, the extraction of air from the cavity may, in some cases, be regarded as intrusive, especially at low values of Φ/Φ_{ref}. In contrast, optical techniques such as PSP are considered to be non-intrusive, regardless of the tested value of Φ/Φ_{ref}.

Furthermore, the availability of 2D effectiveness maps instead of discrete points obtained from sampling measurements would allow an improved and more efficient validation of the numerical codes. This is a crucial aspect that needs to be taken into consideration in order to gain confidence in simulation results. In addition, accidental measurement errors could be more easily identified by examining the surrounding values in contours with high spatial resolution.

Finally, the PSP technique provides the opportunity to conduct more advanced investigations that would otherwise be challenging or impossible such as studies regarding the rotor side of the cavity and the impact of Density Ratio. As demonstrated by the results reported in this chapter, employing an optical approach on the rotor side eliminates the need for complex slip-rings or telemetry while keeping the advantages previously described for the stator side. Moreover, the PSP technique allows the use of different gases for the external annulus and the purge flow in order to achieve different densities, thus allowing the investigation of the effect of the Density Ratio. Hence, this approach allows replicating the operating conditions of actual engines, where the hot main flow has a lower density than the colder cooling flow. In particular, the investigation on the impact of Density Ratio will be presented in the next chapter.

Chapter 7

Impact of Density Ratio on the rim sealing effectiveness

Contents

7.1 Density Ratio results overview

The intent of this chapter is to report and discuss the impact of the Density Ratio on the sealing performance of rim seals by analysing the experimental results obtained through the use of the PSP setup described in Figure 4.9. For this purpose, all the results presented in this chapter have been obtained by using either pure N_2 ($DR = 1$) or pure CO_2 ($DR = 1.52$) as purge flow. The PSP technique, validated for the study of hot gas ingestion in the previous chapter, has been employed to acquire 2D effectiveness maps on both the stator and the rotor side of the cavity. Hence, the obtained results will demonstrate that when a high-density fluid is used as purge flow, a higher mass flow rate is required to seal the cavity. Moreover, a detailed analysis of these results will confirm the presence of higher effectiveness values on the rotor side due to the presence of the buffer layer, regardless of the density of the gas injected into the wheel-space. In the end, the information extracted from the PSP effectiveness maps will be used to calibrate the fitting parameters of the Orifice Model on the stator side and the Buffer Ratio model on the rotor side under different flow conditions where the Externally-Induced regime is the dominant mechanism that drives the hot gas ingestion. This analysis will emphasize the influence of the DR on the low-order models employed in the data analysis.

In analogy with the previous chapter, the test matrix includes three different values of C_f in order to compare the behaviour of the rim seal under design conditions ($C_f = 0.32$) with that under off-design conditions ($C_f = 0.25$ and $C_f = 0.40$). Moreover, multiple values of purge flow have been tested in order to analyse the performance of the rim seal under different sealing conditions. Again, the PSP tests have been conducted only for the baseline M1A rim seal configuration shown in Figure 4.3.

7.2 Derivation of the Orifice Model equations accounting for Density Ratio

In order to thoroughly analyse the impact of Density Ratio on the sealing performance of rim seals, the Orifice Model developed by Owen [9, 14] and described in Section 2.7 has been modified to account for the effect of DR. In comparison to the original version, which was derived under the assumption of equal density between purge and annulus flows ($DR = 1$), this paragraph details the derivation of an updated version of the characteristic equations of this model which incorporate the effect of DR. According to the knowledge of the author of this work on the subject of hot gas ingestion, an expression explicitly including the effect of DR is currently absent in the open literature. To better understand the subsequent analytical steps, it is essential to bear in mind that this study refers to measurements completely conducted under Externally-Induced conditions, thus completely neglecting the ingestion effects caused by the presence of rotational effects within the wheel-space.

The formulation of an updated version of the OM begins by taking into account the density of the flows within the idealized ingress and egress stream-tubes. Hence, the ingress flow is characterized by pure annulus flow whereas the density of the egress flow results from the mixture of purge and ingress flows:

$$\frac{\rho_i}{\rho_0} = \frac{1}{DR} \qquad \longleftrightarrow \qquad \frac{\rho_e}{\rho_0} = \frac{1}{DR} \cdot (1 - M) + M \tag{7.1}$$

Here, M is a variable representing a mixing parameter whose value is not known a priori. However, in light of the general description of the ingress/egress mechanism through rim seals and under the typical assumption that the egress flow exits the wheel-space in correspondence of the rotor side, it appears reasonable to approximate M to the value of sealing effectiveness measured on the rotor surface (ε_R). As discussed in Chapter 6, for a given radius the effectiveness on the rotor surface appears to be consistently higher than the corresponding value on the stator surface. This phenomenon has been attributed to the formation of a buffer layer resulting from the sealing flow being pumped towards the rim seal by the rotating surface. However, due to mixing effects, both the stator and the rotor side inevitably reach the fully sealed condition for the same value of Φ_{min}. As a result, the ratio between densities, ρ_e/ρ_0, is equal to 1 when $M \approx \varepsilon_R = 1$ while it is equal to $1/DR = \rho_i/\rho_0$ when $M \approx \varepsilon_R = 0$.

To make the upcoming expressions concerning the flow through the rim seal more straightforward, it is useful to redefine the sealing parameter Φ by explicitly incorporating the Density Ratio:

$$\Phi = \frac{\rho_0 \cdot U}{\rho_i \cdot \Omega \cdot r_{disk}} = DR \cdot \frac{U}{\Omega \cdot r_{disk}} \tag{7.2}$$

According to this expression, the inertial parameter Φ can thus be interpreted as a ratio between specific mass flows. From a practical perspective, when the rig operates at a given condition in terms of annulus mass flow rate and rotational speed, a specific value of Φ corresponds to a unique value of purge mass flow, regardless of its specific density. Hence, the density can be also explicitly integrated into the following definitions of the mass flows through the orifice stream-tubes:

$$\dot{m}_e = \rho_e \cdot \int V_{r,e} dA_e \tag{7.3}$$

$$\dot{m}_i = \rho_i \cdot \int V_{r,i} dA_i \tag{7.4}$$

Subsequently, starting from the definition of ε_S on the stator side:

$$\varepsilon_s = 1 - \frac{\Phi_i}{\Phi_e} \tag{7.5}$$

it is possible to analytically integrate Eqs. 7.3-7.4 by using the revised definition of Φ shown in Eq. 7.2 and under the assumption that the shape of the pressure distribution on the annulus side ($p_1(\theta)$) can be successfully approximated through the use of a saw-tooth model, as done also by Owen [10] to derive the original equations of the Orifice Model. Therefore, the following updated version of the “EI orifice equation”, which explicitly incorporates the effect of the DR, can be obtained:

$$\frac{\Phi_0}{\Phi_{min}} = \frac{\varepsilon_s \cdot \sqrt{\rho_e/\rho_0}}{\left[1 + \left(\frac{\Gamma_c}{\sqrt{DR} \cdot \sqrt{\rho_e/\rho_0}}\right)^{-\frac{2}{3}} \cdot (1-\varepsilon_s)^{\frac{2}{3}}\right]^{\frac{3}{2}}} \tag{7.6}$$

Finally, the expression defining the minimum sealing parameter to prevent ingress can also be revised to explicitly include the DR:

$$\Phi_{min} = \frac{2}{3} \cdot C_{d,e} \cdot \sqrt{DR} \cdot \sqrt{\Delta C_p} \tag{7.7}$$

Here, the non-dimensional pressure difference ΔC_p is computed by using the density of the annulus flow. This definition allows the calculation of a dimensionless pressure drop that is independent of the density of the purge flow. Hence, its value depends only on the operating conditions of the test rig (annulus mass flow rate and rotational speed). The updated form of the orifice equation (Eq. 7.6), derived through the application of the revised definition of Φ (Eq. 7.2), closely resembles the original expression derived by Owen [10] and rearranged by Sangan [8] (Eq. 2.28), with the exception of the terms involving the density of the purge flow and its interaction with the mainstream flow. Consequently, the expressions are equivalent when $DR = 1$.

Moreover, it is important to consider that, according to Owen et al. [10], the correct value of ΔC_p to be employed in Eq. 7.7 should always be evaluated within the annulus regions defined by the consistency criterion. Hence, it is useful to recall the definition of the normalized axisymmetric pressure g reported in Eq. 2.30 and the subsequent expression of g^* reported in Eq. 2.31. As previously explained, the positions within the annulus where g equals g^* indicate the locations where the ΔC_p is consistent with the value of Γ_c determined by applying the OM. However, since the expression of g^* was derived in the case of complete absence of purge flow, it is evident that the determination of the station 1, where the evaluation of the pressure difference satisfies the consistency criterion, is not directly influenced by the DR but it depends only on the value of Γ_c.

Finally, it is useful to analyse in detail the terms that account for the effect of Density Ratio appearing in the new expression of the Orifice Model reported in Eq. 7.6. Indeed, the term DR is explicitly present, as well as the term ρ_e/ρ_0, which assumes a virtually unknown value. As previously discussed and in a preliminary approximation, the mixing parameter M described in Eq. 7.1 can be considered equivalent to the sealing effectiveness on the rotor side. Thus, the role of M in Eq. 7.6 can be determined by observing the curves reported in Figure 7.1. Here, the stator effectiveness curve calculated by using a typical value of Γ_c, $DR = 1.52$ and by estimating ρ_e/ρ_0 through the assumption that $M = \varepsilon_R(\Phi)$ has been reported in green. The effectiveness curve estimated by using the same values of DR and Γ_c but setting $\rho_e/\rho_0 = 1$ (i.e. $M = 1$) has been instead reported in red. In addition, it is important to notice that the curve in black represents the effectiveness on the rotor side which has been derived directly from the PSP measurements performed by using a value of $DR = 1.52$. Hence, the examination of Figure 7.1 reveals

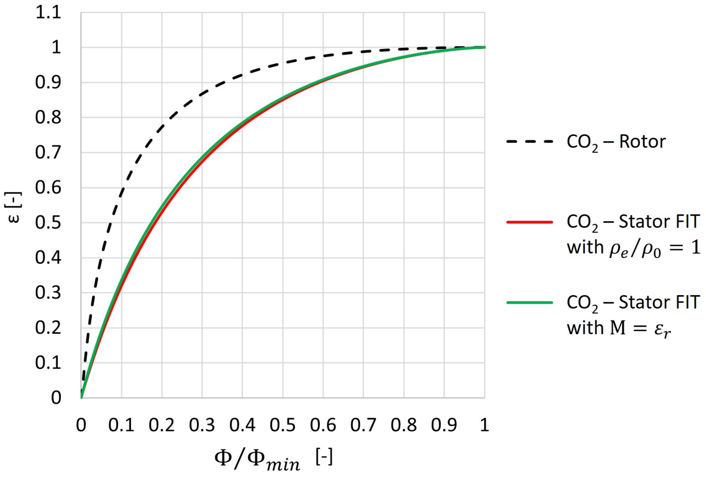

Figure 7.1: Impact of the term ρ_e/ρ_0 on the modified version of the Orifice Model [91].

that the approximation of $\rho_e/\rho_0 = 1$ is completely reasonable, with only a negligible impact on the stator effectiveness curve. Therefore, this approximation will be employed in the data analysis presented in this section, as it maintains the fundamental characteristic of the Orifice Model by uncoupling the cause (external distribution of pressure) from the effect (ingress influencing the effectiveness level).

7.3 Density Ratio results on stator side

Initially, the PSP setup has been employed to conduct multiple tests on the stator side by varying the type of gas and by adjusting the purge mass flow rate to achieve different sealing conditions. The resulting 2D effectiveness maps, obtained for three progressively increasing values of Φ/Φ_{ref}, are presented in Figure 7.2. The left side (Figures 7.2a-7.2c-7.2e) corresponds to the use of N_2 while the right side (Figures 7.2b-7.2d-7.2f) corresponds to the use of CO_2. The N_2 images are the same already seen in Figure 6.1 but they have been also reported here in order to allow a direct comparison with the images related to the use of CO_2. The acquired contours, which represent the values of rim sealing effectiveness directly obtained during the experimental campaign, have been superimposed onto the model of the stator disk in order to highlight the position of the vanes. A general observation applicable to both gases regards the gradual improvement in sealing effectiveness achieved by increasing the pressurization of the cavity through the injection of a higher quantity of purge flow.

Subsequently, a more interesting analysis involves the comparison of the results obtained for the two gases at a specific value of Φ/Φ_{ref}. To achieve this comparison, it is crucial to remember that, as mentioned in the previous section, comparing the same value of Φ/Φ_{ref} for different gases implies injecting the same dimensional quantity of purge flow into the wheel-space without accounting for the distinct specific densities of N_2 and CO_2 (Eq. 7.2). With this assumption in mind, a comparison between the contours reported in Figure 7.2 reveals a similar behaviour

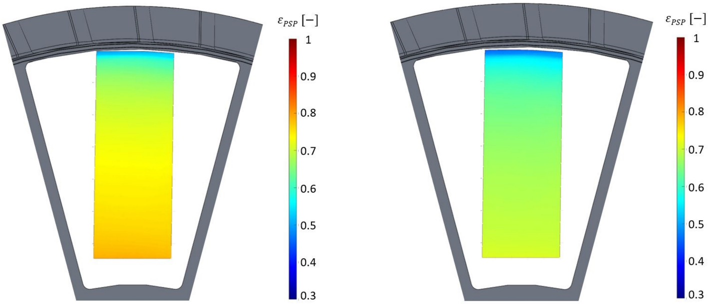

(a) $N_2 - \Phi/\Phi_{ref} = 0.166$ *(b)* $CO_2 - \Phi/\Phi_{ref} = 0.166$

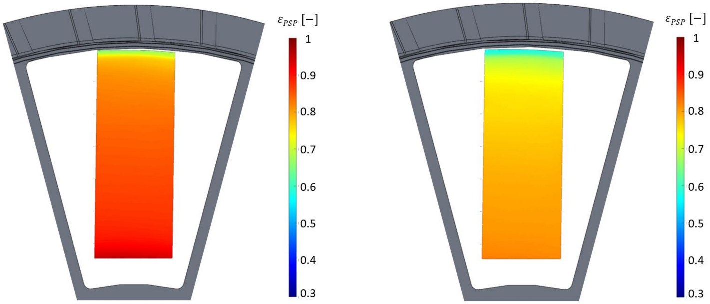

(c) $N_2 - \Phi/\Phi_{ref} = 0.230$ *(d)* $CO_2 - \Phi/\Phi_{ref} = 0.230$

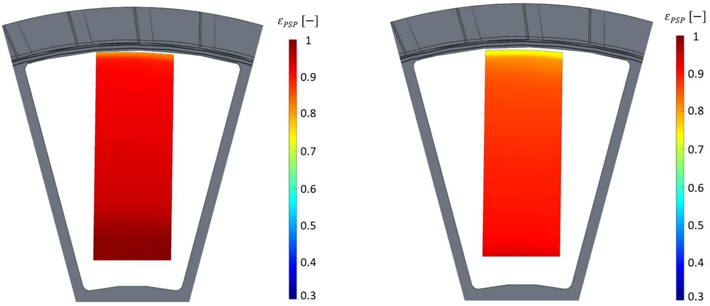

(e) $N_2 - \Phi/\Phi_{ref} = 0.304$ *(f)* $CO_2 - \Phi/\Phi_{ref} = 0.304$

Figure 7.2: PSP effectiveness contours obtained on the stator side by using N_2 *or* CO_2 *and for three different values of purge flow: (a)* $N_2 - \Phi/\Phi_{ref} = 0.166$, *(b)* $CO_2 - \Phi/\Phi_{ref} = 0.166$, *(c)* $N_2 - \Phi/\Phi_{ref} = 0.230$, *(d)* $CO_2 - \Phi/\Phi_{ref} = 0.230$, *(e)* $N_2 - \Phi/\Phi_{ref} = 0.304$ *and (f)* $CO_2 - \Phi/\Phi_{ref} = 0.304$ *[91]. © 2024 Baker Hughes Company - All rights reserved*

for the two gases, with the only distinction being that the use of CO_2 (higher purge flow density) consistently results in lower levels of protection. This phenomenon can be explained by considering the fact that, for comparable values of pressure within the cavity, the purge flow assumes different velocities according to the different densities of the two gases. Additionally, it may be hypothesized that the different velocities could also have an influence on the “spoiling effect” described by Sangan et al. [8]. Moreover, the minimum values of ε_{PSP}, which are associated to the presence of the mixing region near the entrance to the wheel-space, consistently appear to be located at the same radius for every reported value of Φ/Φ_{ref}. The effectiveness in the core region does not seem to be perfectly constant in the radial direction but it appears to be affected by slight variations that seem to be qualitatively similar between the two gases. Hence, the use of sealing flows with different densities does not appear to induce any 2D phenomena inside the cavity in time-averaged terms. This implies the substantial circumferential uniformity of ε_{PSP} in every tested condition. However, as already explained in chapter 6, this observation may be attributed to the use of a low-frequency PSP formulation that required averaging each set of images to obtain a representative snapshot of the flow field inside the wheel-space.

7.4 Density Ratio results on rotor side

The same experiments have been then conducted on the rotor side without making significant adjustments to the setup used for the stator side. Among the numerous acquired 2D effectiveness maps, some of the most interesting results have been reported in Figure 7.3. In particular, the contours obtained at a constant sealing flow rate of $\Phi/\Phi_{ref} = 0.166$ for both N_2 and CO_2 and corresponding to the three tested values of C_f (0.25, 0.32, 0.40) have been superimposed onto the model of the rotor disk. The N_2 images are the same already seen in the left side of Figure 6.4 but they have been also reported here in order to allow a direct comparison with the images related to the use of CO_2. The analysis of these contours

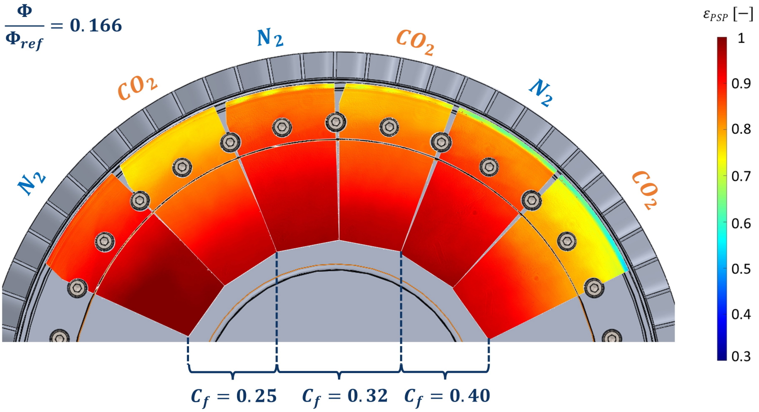

Figure 7.3: PSP effectiveness contours obtained on the rotor side by using N_2 or CO_2 and for different values of C_f at $\Phi/\Phi_{ref} = 0.166$ [91].
© 2024 Baker Hughes Company - All rights reserved

reveals that, for a specific gas and a given quantity of purge flow injected inside the cavity, increasing the flow coefficient C_f and consequently the non-dimensional pressure difference ΔC_p, which acts as the driving force for ingestion in EI conditions, leads to a significant reduction in the rim sealing effectiveness.

Subsequently, it is more interesting to compare the results obtained for N_2 and CO_2 under a specific operating condition of the test rig, both in terms of sealing flow (same Φ) and mass flow rate in the annulus (same ΔC_p). In analogy with the observations made for the effectiveness contours obtained on the stator surface, employing a sealing flow characterized by higher density, such as CO_2, leads to lower effectiveness values despite the contours showing significant qualitative similarity. Moreover, no 2D structures appear to be present, thus implying a significant circumferential uniformity of ε_{PSP} also on the rotor side, except on the tip of the rim seal tooth. Here, the previously discussed presence of non-uniform distributions of effectiveness in the circumferential direction can be observed for both gases. In accordance with the description of the phenomenon provided in Section 6.3.1, these low effectiveness regions appear to be periodically distributed thus confirming that their position seems to be clocked with the LE of the blades. Moreover, these regions appear to be present only at higher values of C_f ($C_f = 0.32$ and $C_f = 0.40$) thus confirming that their presence seems to be influenced by the value of the annulus mass flow rate. However, their appearance does not appear to depend on the density of the purge flow.

Then, the 2D effectiveness contours acquired on both the stator (Figure 7.2) and the rotor (Figure 7.3) were post-processed by using the same procedure described in Chapter 6 to extract the circumferentially averaged radial profiles of effectiveness. The obtained profiles have been reported in Figure 7.4, allowing the simultaneous evaluation of the behaviour of both sides of the cavity for both N_2 and CO_2 at three different values of Φ/Φ_{ref}. By examining the obtained radial trends, it is evident that, for a

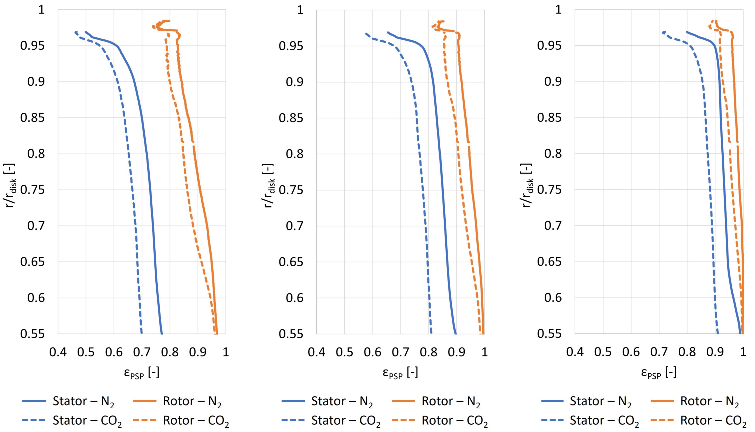

(a) $\Phi/\Phi_{ref} = 0.166$ (b) $\Phi/\Phi_{ref} = 0.230$ (c) $\Phi/\Phi_{ref} = 0.304$

Figure 7.4: Comparison between radial profiles of ε_{PSP} *obtained on both the stator and the rotor sides by using* N_2 *or* CO_2 *and for three different values of purge flow: (a)* $\Phi/\Phi_{ref} = 0.166$*, (b)* $\Phi/\Phi_{ref} = 0.230$ *and (c)* $\Phi/\Phi_{ref} = 0.304$ *[91]. © 2024 Baker Hughes Company - All rights reserved*

given radius and a constant amount of sealing flow, the rotor consistently exhibits greater values of effectiveness compared to the stator, regardless of the density of the gas injected into the wheel-space. As already thoroughly discussed, the increased effectiveness on the rotor side is the result of the presence of a protective buffer layer that forms on the rotating surface due to the disk-pumping effect, a phenomenon that does not appear to be influenced by the DR. Moreover, comparing the results obtained for N_2 and CO_2 on each surface confirms that, although the trends are qualitatively very similar, the use of a sealing flow characterized by higher density always results in lower values of effectiveness for the same quantity of purge flow. Nevertheless, this observation does not hold true for the rotor tooth, where very similar effectiveness values have been obtained. Hence, the effectiveness on the rotor tooth appears to be unaffected by the DR. To gain a more comprehensive understanding of this phenomenon, future tests will be required to thoroughly examine the behaviour of the flow in this limited region of the rim seal.

7.5 Analysis of Density Ratio data on stator and rotor side

Taking into account the observation made at the end of the previous section, the subsequent analysis will focus on the influence of the DR within the wheel-space while neglecting the behaviour of the flow in correspondence of the rotor tooth. For this purpose, the data points obtained experimentally from both the stator and the rotor side can be compared in terms of $\Phi - \varepsilon$ curves to accurately quantify the influence of the DR on the sealing performance of the rim seal. The resulting curves obtained at $r/r_{disk} = 0.943$ for the usual three values of C_f are shown in Figure 7.5 where the black curves are relative to the use of N_2 while the red curves are relative to the use of CO_2. Moreover, the filled symbols correspond to measurements performed on the stator side while the empty symbols correspond to measurements performed on the rotor side. The data on the stator side have been fitted according to the modified version

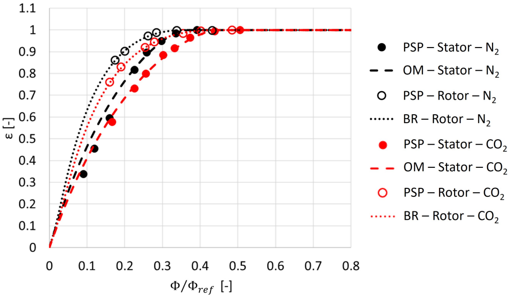

(a) $C_f = 0.25$

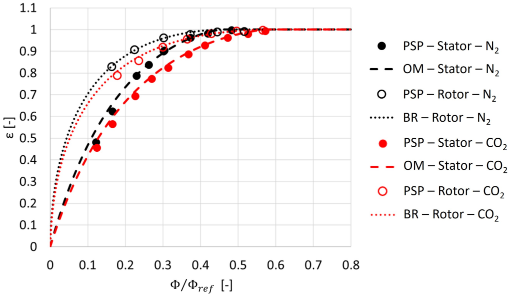

(b) $C_f = 0.32$

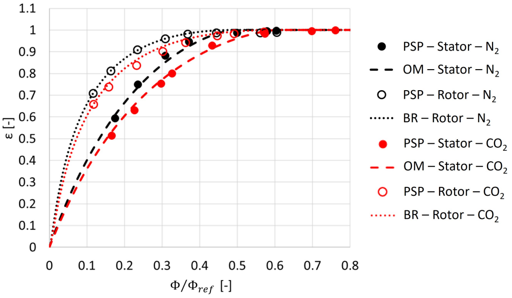

(c) $C_f = 0.40$

Figure 7.5: Comparison in terms of $\Phi - \varepsilon$ *curves between stator (OM fitting) and rotor (BR fitting) obtained at* $r/r_{disk} = 0.943$ *for* N_2 *(black) and* CO_2 *(red) for different values of* C_f*: (a)* $C_f = 0.25$*, (b)* $C_f = 0.32$ *and (c)* $C_f = 0.40$ *[91]. © 2024 Baker Hughes Company - All rights reserved*

of the Orifice Model reported in Eq. 7.6 while the data on the rotor side have been fitted by using the Buffer Ratio model developed by Mear et al. [13] which consists of Eq. 2.36 where the term BR is defined by Eq. 2.37. It is important to note that, since this equation requires the values of Φ_S and ε_S as input to obtain the corresponding $\Phi_R - \varepsilon_R$ curve, there is no need to explicitly include the term DR here, as it is already implicitly taken into account.

As can be noticed, the assumption that the rotor, although generally more protected, may never be fully sealed until there is a mixing region and consequently entrainment of the flow from the stator side, seems to be strongly supported by the results obtained for both gases. Furthermore, the curves resulting from the application of the Orifice Model and the Buffer Ratio Model appear to be in excellent agreement with the experimental data obtained for both N_2 and CO_2 across each tested value of C_f. However, although these curves exhibit the typical shape of conventional effectiveness curves, it is important to note that recent studies, such as the one by Graikos et al. [65], have demonstrated that the use of turned rotor blades may lead to $\Phi - \varepsilon$ curves characterized by the presence of an inflexion. Consequently, these curves might not be adequately fitted by using either the standard Orifice Model equations derived by Owen [9, 14] and rearranged by Sangan et al. [8] or the modified version of the Orifice Model reported in Eq. 7.6 that has been derived during the course of this work.

7.5.1 Effect of Density Ratio on the fitting parameters of the Orifice Model

The resulting fitting parameters obtained from the application of the OM equation on the stator side, which were used to obtain the trends shown in Figure 7.5, are summarized in Table 7.1. In particular, the values of Φ_{min} and Γ_c obtained in the N_2 case ($DR = 1$) are compared with the corresponding values obtained under identical annulus flow conditions but in the CO_2 case ($DR = 1.52$). The following analysis will allow gaining further insights into the effect of DR on the OM fitting parameters.

Table 7.1: Comparison of the optimal fitting parameters (Φ_{min} and Γ_c) obtained by applying the OM on the stator side at $r/r_{disk} = 0.943$ for N_2 and CO_2 and for different values of C_f [91]. © 2024 Baker Hughes Company - All rights reserved

OM fitting	$C_f = 0.25$		$C_f = 0.32$		$C_f = 0.40$	
	N_2	CO_2	N_2	CO_2	N_2	CO_2
$\sqrt{DR}$	1	1.233	1	1.233	1	1.233
$\frac{\Phi_{min,CO_2}}{\Phi_{min,N_2}}$	1.236		1.265		1.243	
$\frac{\Gamma_{c,CO_2}}{\Gamma_{c,N_2}}$	1.007		1.005		1.004	

First, it is interesting to investigate the value assumed by the ratio between the ingress and egress discharge coefficients. As can be noticed, the ratio between Γ_{c,CO_2} and Γ_{c,N_2} appears to be very close to one for all the tested values of C_f. This indicates that the orifice curves obtained for the two gases have essentially the same shape in terms of Φ/Φ_{min} versus ε_S, despite the different densities of the gases used to seal the cavity. Hence, this observation has a direct consequence on the consistency criterion defined by Owen et al. [10] and, in particular, on the expression of g^* reported in Eq. 2.31. As previously highlighted, g^* is defined in the case of total absence of purge flow, thus meaning that its value is determined only by the value assumed by Γ_c while being unaffected by the value of DR. However, having demonstrated that the values of Γ_c obtained for the two gases with different densities are essentially equal, it is evident that the position in the annulus where the pressure difference should be evaluated is completely independent of the density of the purge flow used to seal the cavity. As a result, for a given value of C_f, the value assumed by ΔC_p in Eq. 7.7 appears to be the same regardless of the value of the DR.

On the contrary, the resulting values of Φ_{min} obtained from the application of the Orifice Model are different for the two gases. In particular, when a high-density fluid is used as purge flow, a higher mass flow rate is required to seal the cavity. However, according to the results reported in Table 7.1, it is evident that the ratio between Φ_{min,CO_2} and

Φ_{min,N_2} remains approximately constant for all the tested values of C_f. Moreover, what is even more interesting is that this ratio appears to be very similar to the value of the square root of DR (for the current case $\sqrt{DR} = 1.233$). Therefore, according to Eq. 7.7, it can be concluded that for a specific value of C_f, and thus ΔC_p considering the earlier observation that the consistency criterion is not influenced by the DR, the value of $C_{d,e}$ that characterizes a specific rim seal appears to be quite independent of the density of the gas injected into the wheel-space. Moreover, returning to the definition of Γ_c as the ratio between $C_{d,i}$ and $C_{d,e}$, it can be stated that, since $\Gamma_{c,CO_2} \approx \Gamma_{c,N_2}$ and $C_{d,e,CO_2} \approx C_{d,e,N_2}$, then $C_{d,i,CO_2} \approx C_{d,i,N_2}$ as well. This suggests that, in the EI regime, the values of both ingress and egress discharge coefficients characterizing a specific rim seal appear to be completely independent of the density of the purge flow injected into the wheel-space.

7.5.2 Effect of Density Ratio on the fitting parameters of the Buffer Ratio model

The resulting fitting parameters obtained from the application of the BR model on the rotor side, which were used to obtain the trends shown in Figure 7.5, are summarized in Table 7.2. In particular, the BR fitting has been performed on the data obtained for the N_2 case ($DR = 1$) and then the resulting values of A and n have been also used to perform the fitting on the data obtained under identical annulus flow conditions but for the CO_2 case ($DR = 1.52$). This approach is due to the fact that, as

Table 7.2: Comparison of the optimal fitting parameters (A and n) obtained by applying the BR on the rotor side at $r/r_{disk} = 0.943$ for the N_2 case and for different values of C_f. The same values have been then used to fit also the data for the CO_2 case [91]. © 2024 Baker Hughes Company - All rights reserved

BR fitting for N_2	$C_f = 0.25$	$C_f = 0.32$	$C_f = 0.40$
A	0.616	0.568	0.414
n	0.676	0.281	0.520

mentioned earlier, in the BR model there is no need to explicitly include the term DR, as it is already implicitly taken into account through the use of the values of Φ_S and ε_S respectively obtained for the N_2 and CO_2 cases. As can be seen from Figure 7.5, the trends obtained on the rotor side appear to be in excellent agreement with the experimental data for both gases and for all the tested values of C_f. This suggests that, in the EI regime, even the fitting parameters of the BR model appear to be completely independent of the density of the purge flow injected into the wheel-space.

Conclusions

The aim of this PhD thesis has been to design, commission and test a new Rotating Cavity Rig to experimentally investigate the problem of hot gas ingestion inside a stator-rotor cavity of a gas turbine. Such facility, which is the result of a collaboration between the University of Florence and Baker Hughes, has been installed in the test cell for rotating benches located in the low-pressure wind tunnel area of the THT Lab. It is a single-stage test rig where the test section is constituted by a stator disk containing 44 integrated vanes and a rotor disk containing 66 integrated blades. Both the disks can accommodate replaceable cover plates that, despite some inevitable simplifications, have been specifically designed to replicate different engine rim seals as close as possible. The interchangeability and modularity of the covers allow replacing them with different geometries in order to investigate multiple arrangements with the intent of evaluating the impact of different geometrical parameters on the sealing performance. For this purpose, standard pressure and CO_2 gas sampling measurements can be performed on the stator surface. However, the main innovation of the current test rig resides in the possibility to exploit optical accesses on the stator disk in order to obtain 2D effectiveness maps on both the stator and the rotor sides of the cavity.

The present test rig has been designed to be operated under non-reactive conditions, an approach consistent with the majority of the hot gas ingestion experimental facilities present in literature. The aerodynamic design of the flow path was conducted through numerical simulations performed with the TRAF computational code while the circumferential uniformity of the main annulus flow in the rim seal region was ensured by performing CFD simulations of the feeding system. Subsequently, static structural simulations were performed to verify that the mechanical stresses would remain well below the yield tensile strength of the selected materials and that the values of radial deformation near the rim seal region would be negligible. Additionally, modal and harmonic simulations further confirmed the suitability of the current configuration to ensure a safe operation of the test rig.

Before starting the actual experimental campaign, a series of commissioning tests were conducted to ensure the correct operation of the experimental facility. First, the vibrations in both axial and radial directions were monitored to ensure that they would always remain widely below the threshold value that identifies the safe operation of the test rig. Subsequently, the behaviour of the test rig was verified to be independent of the rotational velocity, in accordance with the studies found in literature. Consequently, this led to the definition of an operational map of the facility which allowed the identification of 2000 RPM as the optimal speed to conduct the experiments. Then, two sets of pressure taps placed after the TE of the vanes were used to verify the circumferential uniformity of the flow in correspondence of the rim seal region. Finally, a test was conducted to demonstrate that the quantity of fluid extracted from the cavity and directed towards the gas analyser would not influence the results, thus ensuring the consistency of the effectiveness measurements.

The sealing performance of seven different configurations of radial rim seals was experimentally determined by performing CO_2 gas sampling measurements on the stator surface. This approach allowed the determination of the impact of different values of axial overlap, different TE-LE distances and different values of radial gap on the effectiveness values. First, the M1A baseline configuration was characterized at design conditions and the shape of the obtained $\Phi - \varepsilon$ curves was observed to agree well with the trends found in literature. However, a variation of the effectiveness values in the radial direction was linked to the presence of an expanded mixing region. By repeating the experiments at multiple off-design conditions, it was possible to highlight that increasing the flow coefficient (and thus the non-dimensional pressure difference) generally results in a reduced level of protection. Nevertheless, a certain level of overlap among the curves was observed in correspondence of the design conditions. This effect was attributed to rotational and unsteady effects but it was suggested that the potential effect of the LE of the blades might also contribute to this phenomenon. Then, the results obtained for the baseline configuration were compared with those obtained for the other six rim seal configurations. The analysis of the impact of different values of axial overlap revealed that a three times greater axial overlap provides an average reduction in the sealing flow rate of approximately 5% (variations in the range $4 - 12\%$). The evaluation of the impact of the TE-LE distance revealed that increasing the vane-blade distance (hence decreasing the influence of the potential effect of the rotor) provides an average reduction in the sealing flow rate of approximately 6% (variations in the range $0 - 10\%$). Finally, the investigation on the impact of different values of radial gap demonstrated that a 2.4 times greater radial gap provides an average increase in the dimensional sealing flow rate of approximately 44% (variations in the range $37 - 51\%$). Therefore, this led to observe that the purge flow required to fully seal a cavity does not increase linearly with the radial gap.

Although gas sampling measurements represent a standard and robust approach to determine the effectiveness inside a stator-rotor cavity, the use of this technique inevitably results in single point measurements where any 2D effect is neglected. Therefore, an alternative approach based on the exploitation of Pressure Sensitive Paint to measure the partial pressure of oxygen and consequently the sealing effectiveness has been presented. Prior to this research, there were no documented cases in literature where PSP had been applied to investigate the phenomenon of hot gas ingestion. First, the 2D maps obtained on the stator side were used to extract multiple radial distributions of effectiveness which were then used to validate the PSP setup through a comparison with the radial profiles obtained by performing standard gas sampling measurements.

Subsequently, the validated PSP setup was used to obtain 2D effectiveness maps on the rotor side where higher effectiveness values were observed. In accordance with the few studies available in literature that have managed to perform effectiveness measurements on the rotor side, this phenomenon was attributed to the presence of a buffer layer formed by the purge flow pumped towards the outer radius by the rotation of the rotor disk. Moreover, a detailed examination of the results obtained on the rotor surface revealed the existence of periodically distributed low-effectiveness regions on the tip of the seal tooth which appeared to be almost perfectly clocked with the LE of the blades. Hence, the presence of such regions with reduced effectiveness was linked to the external static pressure distribution generated by the rotor. In the end, the PSP results obtained separately on the stator and rotor surfaces were correlated with each other by performing sealing effectiveness measurements across the cavity width through the use of a concentration probe. On the stator side, the sealing effectiveness appeared to remain relatively constant within the initial quarter of the cavity width. Then, it gradually increased until a peak was found on the rotor surface. The PSP values obtained on both the stator and rotor surfaces appeared to reasonably match the data acquired with the concentration probe, thus further enhancing the reliability of the PSP approach.

Furthermore, the PSP allowed performing the analysis of the effect of different values of Density Ratio on the sealing performance of the rim seal, an aspect usually neglected in the majority of the experimental facilities present in literature. Hence, two distinct values of Density Ratio were achieved by using either pure N_2 ($DR = 1$) or CO_2 ($DR = 1.52$) as purge flow. The resulting 2D effectiveness maps obtained on both sides of the cavity showed a similar qualitative behaviour for the two gases when the same dimensional quantity of purge flow was injected into the wheel-space. However, it was observed that the use of CO_2 (higher purge flow density) consistently led to reduced levels of protection. This phenomenon was attributed to the fact that, for comparable values of pressure within the cavity, the purge flow assumes different velocities according to the different densities of the two gases. In conclusion, the data gathered from both the stator and the rotor sides were examined in terms of $\Phi - \varepsilon$ curves to determine the influence of the Density Ratio on the sealing performance of the rim seal. Therefore, the experimental data points were respectively fitted by using either a modified version of the Orifice Model that explicitly includes the effect of the Density Ratio or the Buffer Ratio model. The resulting curves appeared to be in excellent agreement with the experimental data obtained for both N_2 and CO_2 across each tested value of C_f. In addition, a detailed investigation of the resulting values of Φ_{min} and Γ_c showed that the ratio between Φ_{min,CO_2} and Φ_{min,N_2} is well approximated by the square root of the DR while the ratio between Γ_{c,CO_2} and Γ_{c,N_2} appears to be very close to one for each tested flow condition. This suggests that, in the EI regime, the values of both ingress and egress discharge coefficients characterizing a specific rim seal appear to be completely independent of the density of the purge flow injected into the wheel-space. Similarly, the analysis of the data obtained on the rotor side indicated that the fitting parameters of the Buffer Ratio model are barely influenced by the density of the purge flow.

List of Figures

List of Tables

Bibliography

[1] Cumpsty, N. and Heyes, A. *Jet propulsion.* Cambridge University Press, 2015.

[2] Alhuyi Nazari, M., Fahim Alavi, M., Salem, M., and Assad, M. E. H. “Utilization of hydrogen in gas turbines: a comprehensive review”. *Int J Low-Carbon Tech*, 17:513–519, February 2022. ISSN 1748-1317. doi: 10.1093/ijlct/ctac025. URL `https://doi.org/10.1093/ijlct/ctac025`.

[3] Chang, C.-C., Do, M. V., Hsu, W.-L., Liu, B.-L., Chang, C.-Y., Chen, Y.-H., Yuan, M.-H., Lin, C.-F., Yu, C.-P., Chen, Y.-H., Shie, J.-L., Wu, W.-Y., Lee, C.-H., and Tuyen, T. V. “A case study on the electricity generation using a micro gas turbine fuelled by biogas from a sewage treatment plant”. *Energies*, 12(12), 2019. ISSN 1996-1073. doi: 10.3390/en12122424.

[4] Breeze, P. “Parabolic trough and fresnel reflector solar power plants”. *Solar Power Generation*, pages 25–34, 2016.

[5] Rovira, A., Abbas, R., Munoz, M., and Sebastian, A. “Analysis of an integrated solar combined cycle with recuperative gas turbine and double recuperative and double expansion propane cycle”. *Entropy*, 22(4), 2020. ISSN 1099-4300. doi: 10.3390/e22040476.

[6] Unnikrishnan, U. and Yang, V. “A review of cooling technologies for high temperature rotating components in gas turbine”. *Propulsion*

and Power Research, 11(3):293–310, 2022. ISSN 2212-540X. doi: 10.1016/j.jppr.2022.07.001. URL `https://www.sciencedirect.com/science/article/pii/S2212540X2200044X`.

[7] Rolls-Royce. *The Jet Engine*. John Wiley & Sons, 5th edition, 2015.

[8] Sangan, C. M., Pountney, O. J., Zhou, K., Wilson, M., Owen, J. M., and Lock, G. D. “Experimental measurements of ingestion through turbine rim seals–part i: Externally induced ingress”. *J. Turbomach*, 135(2), November 2012. ISSN 0889-504X. doi: 10.1115/1.4006609. URL `https://doi.org/10.1115/1.4006609`.

[9] Owen, J. M. “Prediction of ingestion through turbine rim seals–part ii: Externally induced and combined ingress”. *J. Turbomach*, 133 (3), November 2010. ISSN 0889-504X. doi: 10.1115/1.4001178. URL `https://doi.org/10.1115/1.4001178`.

[10] Owen, J. M., Zhou, K., Pountney, O. J., Wilson, M., and Lock, G. D. “Prediction of ingress through turbine rim seals–part i: Externally induced ingress”. *J. Turbomach*, 134(3), July 2011. ISSN 0889-504X. doi: 10.1115/1.4003070. URL `https://doi.org/10.1115/1.4003070`.

[11] Sangan, C. M. *Measurement of ingress through gas turbine rim seals*. PhD thesis, University of Bath Bath, United Kingdom, 2011.

[12] Cho, G.H., Sangan, C. M., Owen, J. M., and Lock, G. D. “Effect of ingress on turbine disks”. *J. Eng. Gas Turbines Power*, 138(4), October 2015. ISSN 0742-4795. doi: 10.1115/1.4031436. URL `https://doi.org/10.1115/1.4031436`.

[13] Isobel Mear, L., Owen, J. M., and Lock, G. D. “Theoretical model to determine effect of ingress on turbine disks”. *Journal of Engineering for Gas Turbines and Power*, 138(3), 2016. ISSN 0742-4795.

[14] Owen, J. M. “Prediction of ingestion through turbine rim seals–part i: Rotationally induced ingress”. *J. Turbomach*, 133(3), November

2010. ISSN 0889-504X. doi: 10.1115/1.4001177. URL `https://doi.org/10.1115/1.4001177`.

[15] Sangan, C. M., Pountney, O. J., Zhou, K., Owen, J. M., Wilson, M., and Lock, G. D. "Experimental measurements of ingestion through turbine rim seals–part ii: Rotationally induced ingress". *J. Turbomach*, 135(2), November 2012. ISSN 0889-504X. doi: 10.1115/1.4006586. URL `https://doi.org/10.1115/1.4006586`.

[16] Scobie, J. A., Sangan, C. M., Teuber, R., Pountney, O. J., Owen, J. M., Wilson, M., and Lock, G. D. "Experimental measurements of ingestion through turbine rim seals–part iv: Off-design conditions". *ASME Paper No. GT2013-94147*, (V03AT15A002), June 2013. doi: 10.1115/GT2013-94147. URL `https://doi.org/10.1115/GT2013-94147`.

[17] Bru Revert, A., Beard, P. F., Chew, J. W., and Bottenheim, S. "Performance of a turbine rim seal subject to rotationally-driven and pressure-driven ingestion". *J. Eng. Gas Turbines Power*, 143 (8), May 2021. ISSN 0742-4795. doi: 10.1115/1.4049858. URL `https://doi.org/10.1115/1.4049858`.

[18] Owen, J. M., Pountney, O. J., and Lock, G. D. "Prediction of ingress through turbine rim seals–part ii: Combined ingress". *J. Turbomach*, 134(3), July 2011. ISSN 0889-504X. doi: 10.1115/1.4003071. URL `https://doi.org/10.1115/1.4003071`.

[19] Sangan, C. M., Pountney, O. J., Scobie, J. A., Wilson, M., Owen, J. M., and Lock, G. D. "Experimental measurements of ingestion through turbine rim seals–part iii: Single and double seals". *J. Turbomach*, 135(5), June 2013. ISSN 0889-504X. doi: 10.1115/1.4007504. URL `https://doi.org/10.1115/1.4007504`.

[20] Bohn, D. E., Decker, A., Ohlendorf, N., and Jakoby, R. "Influence of an axial and radial rim seal geometry on hot gas ingestion into the upstream cavity of a 1.5-stage turbine". *ASME Paper No. GT2006-*

90453, 2006. doi: 10.1115/GT2006-90453. URL `https://doi.org/10.1115/GT2006-90453`.

[21] Childs, P. R. N. *Rotating flow.* Elsevier, 2010.

[22] Batchelor, G. K. "Note on a class of solutions of the navier-stokes equations representing steady rotationally-symmetric flow". *Q J Mechanics Appl Math*, 4(1):29–41, January 1951. ISSN 0033-5614. doi: 10.1093/qjmam/4.1.29. URL `https://doi.org/10.1093/qjmam/4.1.29`.

[23] Stewartson, K. "On the flow between two rotating coaxial disks". *Mathematical Proceedings of the Cambridge Philosophical Society*, 49(2):333–341, 1953. ISSN 0305-0041. doi: 10.1017/S0305004100028437. URL `https://www.cambridge.org/core/article/on-the-flow-between-two-rotating-coaxial-disks/21356A0DCFEF694A2BD2F4DE16B0316C`.

[24] Picha, K. G. and Eckert, E. R. G. "Study of the air flow between coaxial disks rotating with arbitrary velocities in an open or enclosed space". *proceedings of 3rd US Nat. Cong. Appl. Mech*, 1958.

[25] Chen, J.-X., Gan, X., and Owen, J. M. "Heat transfer in an air-cooled rotor-stator system". *J. Turbomach*, 118(3):444–451, July 1996. ISSN 0889-504X. doi: 10.1115/1.2836686. URL `https://doi.org/10.1115/1.2836686`.

[26] Owen, J. M. and Rogers, R. H. *Flow and Heat Transfer in Rotating Disc Systems, Vol.1.* Research Studies Press, Taunton, U. K., 1989.

[27] Daily, J. W. and Nece, R. E. "Chamber dimension effects on induced flow and frictional resistance of enclosed rotating disks". *J. Basic Eng*, 82(1):217–230, March 1960. ISSN 0021-9223. doi: 10.1115/1.3662532. URL `https://doi.org/10.1115/1.3662532`.

[28] Bayley, F. J. and Owen, J. M. "The fluid dynamics of a shrouded disk system with a radial outflow of coolant". *J. Eng. Power*, 92(3):

335–341, July 1970. ISSN 0022-0825. doi: 10.1115/1.3445358. URL `https://doi.org/10.1115/1.3445358`.

[29] Bayley, F. J. and Owen, J. M. “Flow between a rotating and a stationary disc”. *Aeronautical Quarterly*, 20(4):333–354, 1969. ISSN 0001-9259. doi: 10.1017/S000192590000514X. URL `https://www.cambridge.org/core/article/flow-between-a-rotating-and-a-stationary-disc/C60B7EDABDF5BD4B5425BCD610E31B29`.

[30] Phadke, U. P. and Owen, J. M. “An investigation of ingress for an air-cooled shrouded rotating disk system with radial-clearance seals”. *J. Eng. Power*, 105(1):178–182, January 1983. ISSN 0022-0825. doi: 10.1115/1.3227382. URL `https://doi.org/10.1115/1.3227382`.

[31] Graber, D. J., Daniels, W. A., and Johnson, B. V. “Disk pumping test”. *Aero Propulsion Laboratory, Wright-Patterson Air Force Base, OH, Report No. AFWAL-TR-87-2050*, 1987.

[32] Daniels, W. A., Johnson, B. V., Graber, D. J., and Martin, R. J. “Rim seal experiments and analysis for turbine applications”. *J. Turbomach*, 114(2):426–432, April 1992. ISSN 0889-504X. doi: 10.1115/1.2929161. URL `https://doi.org/10.1115/1.2929161`.

[33] Phadke, U. P. and Owen, J. M. “Aerodynamic aspects of the sealing of gas-turbine rotor-stator systems: Part 1: The behavior of simple shrouded rotating-disk systems in a quiescent environment”. *International Journal of Heat and Fluid Flow*, 9(2):98–105, 1988. ISSN 0142-727X. doi: 10.1016/0142-727X(88)90060-4. URL `https://www.sciencedirect.com/science/article/pii/0142727X88900604`.

[34] Chew, J. W. “A theoretical study of ingress for shrouded rotating disk systems with radial outflow”. *J. Turbomach*, 113(1):91–97, January 1991. ISSN 0889-504X. doi: 10.1115/1.2927742. URL `https://doi.org/10.1115/1.2927742`.

[35] Chew, J. W., Dadkhah, S., and Turner, A. B. “Rim sealing of rotor-stator wheelspaces in the absence of external flow”. *J. Turbomach*, 114(2):433–438, April 1992. ISSN 0889-504X. doi: 10.1115/1.2929162. URL `https://doi.org/10.1115/1.2929162`.

[36] Dadkhah, S., Turner, A. B., and Chew, J. W. “Performance of radial clearance rim seals in upstream and downstream rotor-stator wheelspaces”. *J. Turbomach*, 114(2):439–445, April 1992. ISSN 0889-504X. doi: 10.1115/1.2929163. URL `https://doi.org/10.1115/1.2929163`.

[37] Abe, T. “An investigation of turbine disk cooling (experimental investigation and observation of hot gas flow into a wheel space)”. *Proc. 13th CIMAC Congress, Vienna*, pages GT–30, 1979. URL `https://cir.nii.ac.jp/crid/1570291226529896192`.

[38] Phadke, U. P. and Owen, J. M. “Aerodynamic aspects of the sealing of gas-turbine rotor-stator systems: Part 2: The performance of simple seals in a quasi-axisymmetric external flow”. *International Journal of Heat and Fluid Flow*, 9(2):106–112, 1988. ISSN 0142-727X. doi: 10.1016/0142-727X(88)90061-6. URL `https://www.sciencedirect.com/science/article/pii/0142727X88900616`.

[39] Phadke, U. P. and Owen, J. M. “Aerodynamic aspects of the sealing of gas-turbine rotor-stator systems: Part 3: The effect of nonaxisymmetric external flow on seal performance”. *International Journal of Heat and Fluid Flow*, 9(2):113–117, 1988. ISSN 0142-727X. doi: 10.1016/0142-727X(88)90062-8. URL `https://www.sciencedirect.com/science/article/pii/0142727X88900628`.

[40] Hamabe, K. and Ishida, K. “Rim seal experiments and analysis of a rotor-stator system with nonaxisymmetric main flow”. *ASME Paper No. 92-GT-160*, (V001T01A060), June 1992. doi: 10.1115/92-GT-160. URL `https://doi.org/10.1115/92-GT-160`.

[41] Hamabe, K. and Ishida, K. "A simplified model for estimating ingress of gas-turbine rotor-stator systems". *Yokohama International Gas Turbine Congress IGTC-19*, 1991.

[42] Chew, J. W., Green, T., and Turner, A. B. "Rim sealing of rotor-stator wheelspaces in the presence of external flow". *ASME Paper No. 94-GT-126*, 1994. doi: 10.1115/94-GT-126. URL `https://doi.org/10.1115/94-GT-126`.

[43] Green, T. and Turner, A. B. "Ingestion into the upstream wheelspace of an axial turbine stage". *J. Turbomach*, 116(2):327–332, April 1994. ISSN 0889-504X. doi: 10.1115/1.2928368. URL `https://doi.org/10.1115/1.2928368`.

[44] Bohn, D. E., Johann, E., and Kruger, U. "Experimental and numerical investigations of aerodynamic aspects of hot gas ingestion in rotor-stator systems with superimposed cooling mass flow". *ASME Paper No. 95-GT-143*, 1995. doi: 10.1115/95-GT-143. URL `https://doi.org/10.1115/95-GT-143`.

[45] Hills, N. J., Green, T., Turner, A. B., and Chew, J. W. "Aerodynamics of turbine rim-seal ingestion". *ASME Paper No. 97-GT-268*, (V003T09A051), June 1997. doi: 10.1115/97-GT-268. URL `https://doi.org/10.1115/97-GT-268`.

[46] Bohn, D. E., Rudzinski, B., Surken, N., and Gartner, W. "Influence of rim seal geometry on hot gas ingestion into the upstream cavity of an axial turbine stage". *ASME Paper No. 99-GT-248*, 1999. doi: 10.1115/99-GT-248. URL `https://doi.org/10.1115/99-GT-248`.

[47] Bohn, D., Rudzinski, B., Surken, N., and Gartner, W. "Experimental and numerical investigation of the influence of rotor blades on hot gas ingestion into the upstream cavity of an axial turbine stage". *ASME Paper No. 00-GT-284*, 78569:V003T01A088, 2000. ISSN 0791878562.

[48] Khilnani, V. I. and Bhavnani, S. H. "Sealing of gas turbine disk cavities operating in the presence of mainstream external flow".

Experimental Thermal and Fluid Science, 25(3):163–173, 2001. ISSN 0894-1777. doi: 10.1016/S0894-1777(01)00083-8. URL `https://www.sciencedirect.com/science/article/pii/S0894177701000838`.

[49] Hills, N. J., Chew, J. W., and Turner, A. B. "Computational and mathematical modeling of turbine rim seal ingestion". *J. Turbomach*, 124(2):306–315, April 2002. ISSN 0889-504X. doi: 10.1115/1.1456461. URL `https://doi.org/10.1115/1.1456461`.

[50] Bohn, D. and Wolff, M. "Improved formulation to determine minimum sealing flow - cw, min - for different sealing configurations". *ASME Paper No. GT2003-38465*, pages 1041–1049, June 2003. doi: 10.1115/GT2003-38465. URL `https://doi.org/10.1115/GT2003-38465`.

[51] Gentilhomme, O., Hills, N. J., Turner, A. B., and Chew, J. W. "Measurement and analysis of ingestion through a turbine rim seal". *J. Turbomach*, 125(3):505–512, August 2003. ISSN 0889-504X. doi: 10.1115/1.1556411. URL `https://doi.org/10.1115/1.1556411`.

[52] Bohn, D. E., Decker, A., Ma, H., and Wolff, M. "Influence of sealing air mass flow on the velocity distribution in and inside the rim seal of the upstream cavity of a 1.5-stage turbine". *ASME Paper No. GT2003-38459*, 2003. doi: 10.1115/GT2003-38459. URL `https://doi.org/10.1115/GT2003-38459`.

[53] Jakoby, R., Zierer, T., Lindblad, K., Larsson, J., deVito, L., Bohn, D.E., Funcke, J., and Decker, A. "Numerical simulation of the unsteady flow field in an axial gas turbine rim seal configuration". *ASME Paper No. GT2004-53829*, pages 431–440, June 2004. doi: 10.1115/GT2004-53829. URL `https://doi.org/10.1115/GT2004-53829`.

[54] Cao, C., Chew, J. W., Millington, P. R., and Hogg, S. I. "Interaction of rim seal and annulus flows in an axial flow turbine". *J. Eng.*

Gas Turbines Power, 126(4):786–793, November 2004. ISSN 0742-4795. doi: 10.1115/1.1772408. URL `https://doi.org/10.1115/1.1772408`.

[55] Johnson, B. V., Jakoby, R., Bohn, D. E., and Cunat, D. “A method for estimating the influence of time-dependent vane and blade pressure fields on turbine rim seal ingestion”. *ASME Paper No. GT2006-90853*, pages 1519–1530, May 2006. doi: 10.1115/GT2006-90853. URL `https://doi.org/10.1115/GT2006-90853`.

[56] Roy, R. P., Zhou, D. W., Ganesan, S., Wang, C.-Z., Paolillo, R. E., and Johnson, B. V. “The flow field and main gas ingestion in a rotor-stator cavity”. *ASME Paper No. GT2007-27671*, 2007. doi: 10.1115/GT2007-27671. URL `https://doi.org/10.1115/GT2007-27671`.

[57] Johnson, B. V., Wang, C.-Z., and Roy, R. P. “A rim seal orifice model with 2 cds and effects of swirl in seals”. *ASME Paper No. GT2008-50650*, pages 1531–1541, June 2008. doi: 10.1115/GT2008-50650. URL `https://doi.org/10.1115/GT2008-50650`.

[58] Zhou, D. W., Roy, R. P., Wang, C.-Z., and Glahn, J. A. “Main gas ingestion in a turbine stage for three rim cavity configurations”. *J. Turbomach*, 133(3), December 2011. ISSN 0889-504X. doi: 10.1115/1.4002423. URL `https://doi.org/10.1115/1.4002423`.

[59] Balasubramanian, J., Junnarkar, N., Zhou, D. W., Roy, R. P., Kim, Y. W., and Moon, H. K. “Experiments on aft-disk cavity ingestion in a model 1.5-stage axial-flow turbine”. *ASME Paper No. GT2011-45895*, 2011. doi: 10.1115/GT2011-45895. URL `https://doi.org/10.1115/GT2011-45895`.

[60] Coren, D. D., Atkins, N. R., Turner, J. R., Eastwood, D. E., Davies, S., Child, P. R. N., Dixon, J. A., and Scanlon, T. J. “An advanced multiconfiguration stator well cooling test facility”. *J. Turbomach*, 135(1), October 2013. ISSN 0889-504X. doi: 10.1115/1.4006317. URL `https://doi.org/10.1115/1.4006317`.

[61] Eastwood, D., Coren, D. D., Long, C. A., Atkins, N. R., Childs, P. R. N., Scanlon, T. J., and Guijarro-Valencia, A. "Experimental investigation of turbine stator well rim seal, re-ingestion and interstage seal flows using gas concentration techniques and displacement measurements". *J. Eng. Gas Turbines Power*, 134 (8), June 2012. ISSN 0742-4795. doi: 10.1115/1.4005967. URL `https://doi.org/10.1115/1.4005967`.

[62] Pountney, O. J., Sangan, C. M., Lock, G. D., and Owen, J. M. "Effect of ingestion on temperature of turbine disks". *J. Turbomach*, 135 (5), June 2013. ISSN 0889-504X. doi: 10.1115/1.4007503. URL `https://doi.org/10.1115/1.4007503`.

[63] Scobie, J. A. *An Experimental Study of Gas Turbine Rim Seals*. PhD thesis, University of Bath Bath, United Kingdom, 2014.

[64] Patinios, M., Scobie, J. A., Sangan, C. M., Owen, J. M., and Lock, G. D. "Measurements and modeling of ingress in a new 1.5-stage turbine research facility". *J. Eng. Gas Turbines Power*, 139 (1), August 2016. ISSN 0742-4795. doi: 10.1115/1.4034240. URL `https://doi.org/10.1115/1.4034240`.

[65] Graikos, D., Carnevale, M., Sangan, C. M., Lock, G. D., and Scobie, J. A. "Influence of flow coefficient on ingress through turbine rim seals". *J. Eng. Gas Turbines Power*, 143(11), September 2021. ISSN 0742-4795. doi: 10.1115/1.4051912. URL `https://doi.org/10.1115/1.4051912`.

[66] Scobie, J. A., Sangan, C. M., Owen, J. M., and Lock, G. D. "Review of ingress in gas turbines". *J. Eng. Gas Turbines Power*, 138(12), July 2016. ISSN 0742-4795. doi: 10.1115/1.4033938. URL `https://doi.org/10.1115/1.4033938`.

[67] Boutet-Blais, G., Lefrancois, J., Dumas, G., Julien, S., Harvey, J.-F., Marini, R., and Caron, J.-F. "Passive tracer validity for cooling effectiveness through flow computation in a turbine rim seal environment".

ASME Paper No. GT2011-45654, 2011. doi: 10.1115/GT2011-45654. URL `https://doi.org/10.1115/GT2011-45654`.

[68] Wisler, D. C. “Loss reduction in axial-flow compressors through low-speed model testing”. *J. Eng. Gas Turbines Power*, 107(2):354–363, April 1985. ISSN 0742-4795. doi: 10.1115/1.3239730. URL `https://doi.org/10.1115/1.3239730`.

[69] Orsini, L., Picchi, A., Bonini, A., Innocenti, L., Di Benedetto, D., Da Soghe, R., and Mazzei, L. “Design procedure of a rotating cavity rig for hot gas ingestion investigation”. *ASME Paper No. GT2022-82676*, 2022. doi: 10.1115/GT2022-82676. URL `https://doi.org/10.1115/GT2022-82676`.

[70] Arnone, A., Liou, M.-S., and Povinelli, L. A. “Navier-stokes solution of transonic cascade flows using nonperiodic c-type grids”. *Journal of Propulsion and Power*, 8(2):410–417, March 1992. doi: 10.2514/3.23493. URL `https://doi.org/10.2514/3.23493`.

[71] Pacciani, R., Rubechini, F., Arnone, A., and Lutum, E. “Calculation of steady and periodic unsteady blade surface heat transfer in separated transitional flow”. *J. Turbomach*, 134(6), September 2012. ISSN 0889-504X. doi: 10.1115/1.4006312. URL `https://doi.org/10.1115/1.4006312`.

[72] Pichler, R., Zhao, Y., Sandberg, R., Michelassi, V., Pacciani, R., Marconcini, M., and Arnone, A. “Large-eddy simulation and rans analysis of the end-wall flow in a linear low-pressure turbine cascade, part i: Flow and secondary vorticity fields under varying inlet condition”. *J. Turbomach*, 141(12), November 2019. ISSN 0889-504X. doi: 10.1115/1.4045080. URL `https://doi.org/10.1115/1.4045080`.

[73] Marconcini, M., Pacciani, R., Arnone, A., Michelassi, V., Pichler, R., Zhao, Y., and Sandberg, R. “Large-eddy simulation and rans analysis of the end-wall flow in a linear low-pressure-turbine cascade–part ii:

Loss generation". *J. Turbomach*, 141(5), January 2019. ISSN 0889-504X. doi: 10.1115/1.4042208. URL `https://doi.org/10.1115/1.4042208`.

[74] Berdanier, R. A., Monge-Concepcion, I., Knisely, B. F., Barringer, M. D., Thole, K. A., and Grover, E. A. "Scaling sealing effectiveness in a stator-rotor cavity for differing blade spans". *J. Turbomach*, 141(5), January 2019. ISSN 0889-504X. doi: 10.1115/1.4042423. URL `https://doi.org/10.1115/1.4042423`.

[75] Da Soghe, R., Bianchini, C., Mazzei, L., Bonini, A., Innocenti, L., Di Benedetto, D., and Orsini, L. "On the extrapolation of rim sealing performance from test bench to real engine: A numerical survey". *J. Eng. Gas Turbines Power*, 144(4), January 2022. ISSN 0742-4795. doi: 10.1115/1.4052879. URL `https://doi.org/10.1115/1.4052879`.

[76] Orsini, L., Brocchi, S., Picchi, A., Facchini, B., Bonini, A., and Innocenti, L. "Commissioning of a newly designed experimental facility for hot gas ingestion investigation". *ETC Paper No. ETC2023-263*, 2023.

[77] Navarra, K. R. *Development of the pressure-sensitive-paint technique for advanced turbomachinery applications*. PhD thesis, Virginia Polytechnic Institute and State Univeristy, Blacksburg, VA, 1997.

[78] Liu, T., Sullivan, J. P., Asai, K., Klein, C., and Egami, Y. *Pressure and temperature sensitive paints*, volume 1. Springer, 2005.

[79] Orsini, L., Picchi, A., Facchini, B., Bonini, A., and Innocenti, L. "On the use of pressure-sensitive paint to determine the rim sealing effectiveness". *J. Turbomach*, 146(2), October 2023. ISSN 0889-504X. doi: 10.1115/1.4063754. URL `https://doi.org/10.1115/1.4063754`.

[80] Gregory, J. W., Juliano, T. J., Disotell, K. J., Peng, D., Crafton, J., and Komerath, N. M. "Deconvolution-based algorithms for deblurring

psp images of rotating surfaces". *Proceedings of the AIAA Aerospace Sciences Meeting*, pages 2013–0484, 2013.

[81] Charbonnier, D., Ott, P., Jonsson, M., Cottier, F., and Kobke, Th. "Experimental and numerical study of the thermal performance of a film cooled turbine platform". *ASME Paper No. GT2009-60306*, 2009. doi: 10.1115/GT2009-60306. URL `https://doi.org/10.1115/GT2009-60306`.

[82] Ahn, J., Schobeiri, M. T., Han, J.-C., and Moon, H.-K. "Film cooling effectiveness on the leading edge region of a rotating turbine blade with two rows of film cooling holes using pressure sensitive paint". *J. Heat Transfer*, 128(9):879–888, April 2006. ISSN 0022-1481. doi: 10.1115/1.2241945. URL `https://doi.org/10.1115/1.2241945`.

[83] Caciolli, G., Facchini, B., Picchi, A., and Tarchi, L. "Comparison between psp and tlc steady state techniques for adiabatic effectiveness measurement on a multiperforated plate". *Experimental Thermal and Fluid Science*, 48:122–133, 2013. ISSN 0894-1777. doi: 10.1016/j.expthermflusci.2013.02.015. URL `https://www.sciencedirect.com/science/article/pii/S0894177713000526`.

[84] Babazzi, G., Bacci, T., Picchi, A., Fondelli, T., Lenzi, T., Facchini, B., and Cubeda, S. "Development and application of a concentration probe for mixing flows tracking in turbomachinery applications". *J. Turbomach*, 144(3), November 2021. ISSN 0889-504X. doi: 10.1115/1.4052419. URL `https://doi.org/10.1115/1.4052419`.

[85] Babazzi, G., Bacci, T., Picchi, A., Facchini, B., and Cubeda, S. "Film cooling and cold streaks tracking on a fully cooled nozzle guide vane under representative combustor outflow conditions". *J. Turbomach*, 145(2), October 2022. ISSN 0889-504X. doi: 10.1115/1.4055500. URL `https://doi.org/10.1115/1.4055500`.

[86] Kline, S. J. and McClintock, F. A. "Describing uncertainties in

single sample experiments". *Mech. Engineering*, 75:3–8, 1953. URL `https://cir.nii.ac.jp/crid/1571698599500606336`.

[87] Robak, C. W., Faghri, A., and Thole, K. A. "Analysis of gas turbine rim cavity ingestion with axial purge flow injection". *ASME Paper No. GT2019-91807*, (V05BT15A011), June 2019. doi: 10.1115/GT2019-91807. URL `https://doi.org/10.1115/GT2019-91807`.

[88] Horwood, J. T. M., Hualca, F. P., Wilson, M., Scobie, J. A., Sangan, C. M., Lock, G. D., Dahlqvist, J., and Fridh, J. "Flow instabilities in gas turbine chute seals". *J. Eng. Gas Turbines Power*, 142 (2), January 2020. ISSN 0742-4795. doi: 10.1115/1.4045148. URL `https://doi.org/10.1115/1.4045148`.

[89] Roy, A. S., Fridh, J., Scobie, J. A., Sangan, C. M., and Lock, G. D. "Flow instability effects related to purge through a gas turbine chute seal". *Journal of the Global Power and Propulsion Society*, 5:111–125, 2021.

[90] Da Soghe, R., Bianchini, C., Sangan, C. M., Scobie, J. A., and Lock, G. D. "Numerical characterization of hot-gas ingestion through turbine rim seals". *Journal of Engineering for Gas Turbines and Power*, 139(3), 2017. ISSN 0742-4795.

[91] Orsini, L., Picchi, A., Facchini, B., Bonini, A., and Innocenti, L. "Impact of the purge flow density ratio on the rim sealing effectiveness in hot gas ingestion measurements". *J. Turbomach*, 146(2), October 2023. ISSN 0889-504X. doi: 10.1115/1.4063755. URL `https://doi.org/10.1115/1.4063755`.